LBL-37170
UC-401

Lawrence Berkeley Laboratory

UNIVERSITY OF CALIFORNIA

CHEMICAL SCIENCES DIVISION

Dynamics of Inelastic and Reactive Gas-Surface Collisions

L.A. Smoliar
(Ph.D. Thesis)

April 1995

REFERENCE COPY
Does Not
Circulate
Bldg. 50 Library.
LBL-37170
Copy 1

Prepared for the U.S. Department of Energy under Contract Number DE-AC03-76SF00098

DISCLAIMER

This document was prepared as an account of work sponsored by the United States Government. While this document is believed to contain correct information, neither the United States Government nor any agency thereof, nor The Regents of the University of California, nor any of their employees, makes any warranty, express or implied, or assumes any legal responsibility for the accuracy, completeness, or usefulness of any information, apparatus, product, or process disclosed, or represents that its use would not infringe privately owned rights. Reference herein to any specific commercial product, process, or service by its trade name, trademark, manufacturer, or otherwise, does not necessarily constitute or imply its endorsement, recommendation, or favoring by the United States Government or any agency thereof, or The Regents of the University of California. The views and opinions of authors expressed herein do not necessarily state or reflect those of the United States Government or any agency thereof, or The Regents of the University of California.

Lawrence Berkeley Laboratory is an equal opportunity employer.

DISCLAIMER

This document was prepared as an account of work sponsored by the United States Government. While this document is believed to contain correct information, neither the United States Government nor any agency thereof, nor the Regents of the University of California, nor any of their employees, makes any warranty, express or implied, or assumes any legal responsibility for the accuracy, completeness, or usefulness of any information, apparatus, product, or process disclosed, or represents that its use would not infringe privately owned rights. Reference herein to any specific commercial product, process, or service by its trade name, trademark, manufacturer, or otherwise, does not necessarily constitute or imply its endorsement, recommendation, or favoring by the United States Government or any agency thereof, or the Regents of the University of California. The views and opinions of authors expressed herein do not necessarily state or reflect those of the United States Government or any agency thereof or the Regents of the University of California.

LBL-37170

DYNAMICS OF INELASTIC AND REACTIVE GAS-SURFACE COLLISIONS

LAURA ANN SMOLIAR
Ph.D. Thesis

DEPARTMENT OF CHEMISTRY
University of California, Berkeley

and

CHEMICAL SCIENCES DIVISION
Lawrence Berkeley Laboratory
University of California
Berkeley, CA 94720

APRIL 1995

This work was supported by the Director, Office of Energy Research, Office of Basic Energy Sciences, Materials Sciences Division, of the U.S. Department of Energy under Contract No. DE-AC03-76SF00098.

Dynamics of Inelastic and Reactive Gas-Surface Collisions

by

Laura Ann Smoliar

A.B. (Columbia University) 1990

A dissertation submitted in partial satisfaction of the

requirements for the degree of

Doctor of Philosophy

in

Chemistry

in the

GRADUATE DIVISION

of the

UNIVERSITY of CALIFORNIA at BERKELEY

1995

Committee in charge:

Professor Yuan T. Lee, Chair
Professor Gabor. A. Somorjai
Professor D. R. Olander

Abstract

Dynamics of Inelastic and Reactive Gas-Surface Collisions

by

Laura Ann Smoliar

Doctor of Philosophy in Chemistry

University of California at Berkeley

Professor Yuan T. Lee, Chair

The dynamics of inelastic and reactive collisions in atomic beam-surface scattering are presented. The inelastic scattering of hyperthermal rare gaseous atoms from three alkali halide surfaces was studied to understand mechanical energy transfer in unreactive systems. The dynamics of the chemical reaction in the scattering of H(D) atoms from the surfaces of LiF(001) and the basal plane of graphite were also studied.

First, the energy transfer from hyperthermal He atoms and Ne atoms to the (001) faces of LiF and NaCl single crystals was determined by measuring time-of-flight spectra for the incident and scattered atomic beams. In addition, the angular dependence of scattering was explored with respect to two angles: θ_i, the angle between the beam and the surface; and ϕ_i, the angle of the beam with respect to the [100] surface direction. To extend this study, the hyperthermal scattering of the series of rare gas atoms: Ne, Ar, Kr, and Xe from a rough CsI surface is

discussed. The experimental results are compared to the predictions of a classical impulsive collision model, where energy transfer is dependent on the masses of the collision partners and not on the collision energy.

Second, the dynamics of the formation of products in the reactions of H(D) + LiF(001) and D + graphite are discussed. The last step in the reaction and subsequent desorption of the newly formed product are probed by measuring the time-of-flight spectra of the HF, DF, CD_4, C_2D_2, and C_2D_4 product molecules as they leave the surface. There is evidence for exit channels in the potential energy surfaces of all the products observed, and in addition two types of surface reaction mechanisms are seen: Eley-Rideal and Langmuir-Hinshelwood.

For my family.

Table of Contents

Abstract 1

Dedication iii

List of Figures vii

List of Tables x

Acknowledgements xi

Chapter 1 Introduction 1

References 6

Chapter 2 Scattering of Hyperthermal Rare Gas Beams from Two Alkali Halide Surfaces 8

Introduction 8

Experimental 12

Results 14

Scattering from LiF(001) 15

Scattering from NaCl(001) 18

Discussion 19

Conclusion 24

References and Notes 26

Figure Captions 29

Figures 34

Chapter 3 Energy Transfer in the Scattering of Hyperthermal Rare Gas Beams from a CsI Surface 49

Introduction 49

Experimental 51

Results 53

Discussion 56

Conclusions 60

References and Notes 61

Figure Captions 63

Figures 65

Chapter 4 Atomic Beam-Surface Scattering Study of HF(DF) Produced in the Reaction: H(D) + LiF(001) 72

Introduction 72

Experimental 73

Results 76

Discussion 78

Atomic Reactant Species 78

Origin of the Fast Time-of-Flight Peak 79

Dynamics of HF and DF Products 82

Surface Reaction Mechanism 86

Conclusion 87

References and Notes 89

Figure Captions 92

Figures 94

Chapter 5 Dynamics of the Acetylene-d_2, Ethylene-d_4, and Tetradeuteromethane Products from the Reaction of D-Atoms with a Graphite Surface . . . 103

Introduction 103

Experimental 104

Results 106

Discussion 111

Product Translational Energy 111

Product θ_i Distributions 113

Microscopic Picture 116

Comparison with other Molecular Beam Etching Studies . 118

Conclusion 119

References and Notes 121

Tables 124

Figure Captions 126

Figures 130

List of Figures

Fig. 2-1	Gas-Surface Scattering Apparatus	34
Fig. 2-2	Beam Characterization for 0.6% Ne/H_2 and 1% He/H_2 .	35
Fig. 2-3	Time-of-Flight Data from 3 and 20 kcal/mole He Atoms Scattered from LiF(001)	36
Fig. 2-4	Translational Energy Distributions for the Fits in Fig. 2-3	37
Fig. 2-5	Energy Transfer as a Function of Collision Energy .	38
Fig. 2-6	The ϕ_i Dependence of He Atom Scattering from LiF(001)	39
Fig. 2-7	Ne Atoms Scattered from LiF(001) with E_{coll}=45 kcal/mole	40
Fig. 2-8	The ϕ_i Dependence of Ne Atom Scattering from LiF(001)	41
Fig. 2-9	Time-of-Flight data from 3 and 20 kcal/mole He Atoms Scattered from NaCl(001)	42
Fig. 2-10	Translational Energy Distributions for the Fits in Fig. 2-9	43
Fig. 2-11	Ne Atoms Scattered from NaCl(001) with E_{coll}=45 kcal/mole	44
Fig. 2-12	The ϕ_i Dependence of Ne Atom Scattering	

	from NaCl(001)	45
Fig. 2-13	θ_i Distribution for 13 kcal/mole Ne Atoms Scattered from NaCl(001)	46
Fig. 2-14	Relative Ion Sizes in LiF(001) and NaCl(001) . .	47
Fig. 2-15	Three Types of Scattering, θ_i Dependence . . .	48
Fig. 3-1	Beam Characterization	65
Fig. 3-2	Time-of-Flight Data for Ne, Ar, Kr, and Xe Atoms Scattered from CsI with E_{coll}=20 kcal/mole	66
Fig. 3-3	Time-of-Flight Data for Ar Atoms with Three Incident Energies	67
Fig. 3-4	Time-of-Flight Data for Scattered Kr Atoms with E_{coll}=50 kcal/mole and Xe Atoms with E_{coll}=65 kcal/mole .	68
Fig. 3-5	Translational Energy Distribution for Scattered Kr Atoms from Fig. 3-4	69
Fig. 3-6	Translational Energy Distribution for Scattered Xe Atoms from Fig. 3-4	70
Fig. 3-7	Energy Transfer as a Function of Collision Energy .	71
Fig. 4-1	Nozzle Temperature as a Function of Power . .	94
Fig. 4-2	Collisional Ionization	95
Fig. 4-3	HF Product Time-of-Flight Data	96
Fig. 4-4	DF Product Time-of-Flight Data	97
Fig. 4-5	HF and DF Translational Energy Distribution . .	98

Fig. 4-6	θ_i Distributions for HF and DF	99
Fig. 4-7	Evidence for Exit Channel Barrier	100
Fig. 4-8	Microscopic Picture	101
Fig. 4-9	Polar Plot of θ_i Distribution for HF	102
Fig. 5-1	Time-of-Flight Data for m/e=18, 20 . . .	130
Fig. 5-2	Tetradeuteromethane Translational Energy Distribution	131
Fig. 5-3	Time-of-Flight Data for m/e=20 at Different θ_i . .	132
Fig. 5-4	Time-of-Flight Data for m/e=32 at Different θ_i . .	133
Fig. 5-5	Ethylene-d_4 Translational Energy Distribution . .	134
Fig. 5-6	Time-of-Flight Data for m/e=26 at Different θ_i . .	135
Fig. 5-7	Acetylene-d_2 Translational Energy Distribution . .	136
Fig. 5-8	Time-of-Flight Data for m/e=16 at Different θ_i . .	137
Fig. 5-9	Time-of-Flight Data for m/e=14	138
Fig. 5-10	Time-of-Flight Data for m/e=30	139
Fig. 5-11	Evidence for Exit Channel Barriers	140
Fig. 5-12	Polar Plot of θ_i Distribution for Acetylene-d_2 . .	141
Fig. 5-13	Polar Plot of θ_i Distribution for Ethylene-d_4 . .	142
Fig. 5-14	Polar Plot of θ_i Distribution for Tetradeuteromethane	143

List of Tables

Chapter 5

Table I Assignment of Detected Ions from Reaction . . 124

Table II Fragmentation Patterns 125

Acknowledgements

Professor Yuan T. Lee has truly been an inspiration to work for, and I will never be able to thank him enough for the many unusual opportunities that he gave me in addition to wonderful scientific guidance. The most exciting of these was spending seven months in Taipei at the Institute of Atomic and Molecular Sciences, Academia Sinica, where I wrote this thesis. I also appreciated the copious advice that rolled out of the FAX machine when I was really stuck, especially during the time I was trying to assemble the Gas Surface Machine (GSM). Yuan always supported me through the tough times at Berkeley, and taught me a lot about people in the process.

When I started in the Lee Group, Dr. Deon Anex, David Gosalvez, and Mathew Lewin were my co-workers in D43, and they introduced me to many resources at Berkeley. In D43, I also had the pleasure of working with Nancy Chu, Cindy Berrie, and Dr. Gang-Yu Liu.

Almost everyone in the group has made a contribution to the running of the GSM. Floyd Davis was full of great advice about detectors and beams and had the idea of using Cl_2 and Br_2 photodissociation to calibrate the detector. He also had the great talent of making everything look easy and was always happy to talk about experiments. Jim Myers taught me about interfacing and programming in C++ and was instrumental in getting the data acquisition working. We had many useful discussions about ways to approach data fitting. Tzong-Tsong Miau helped me

with calibrating the rhenium nozzle on the 35" machine, brought me food when I was running the experiment for long periods of time, and would stay up late to help me fix broken equipment. Miau is a master of machines and what I know about building, fixing, and maintaining the GSM I learned from him. Arthur Suits was instrumental in convincing me to NOT use an LSI-11 computer to take data, for which I am forever grateful. It was nice to have him return recently since he is always happy to discuss data (and I finally had some to discuss when he got back).

I enjoyed late night discussions about science with my officemates, Allan Bracker and James Chesko, who could always make me laugh. Dr. Kim Prather was my colleague and roommate during my most difficult time in graduate school. She was extremely supportive during my second year orals. Thanks also to Jingsong Zhang, Doo Wan Boo, Hongtao Hou, and Marcus J. J. Vrakking for their help and equipment loans. Ann Lawhead helped me get through all the bureaucracy of LBL and Berkeley, and is always a source of useful information. Thanks to the machinists who did an excellent job on the GSM parts, Bob Conroy of the LBL machine shop who welded the rhenium nozzles, and the electronics and glass shops.

In preparation for Taiwan, Xueming Yang was helpful to consult about mechanical drawing and tolerances on the rotating source machine. Zhifeng Liu helped me master data transfer over the Internet to Taiwan and he, Miau, Jinchun Xie and K. T. Liu attempted to teach me some Mandarin.

My experience in Taiwan was wonderful because of the many generous

people at the Institute of Atomic and Molecular Sciences (IAMS) that made us feel at home. Professor Shen-maw Lin let me monopolize his best computer to write this thesis, and I enjoyed my daily discussions with him about science, Chinese food, Taiwan, and Berkeley in the 1960's. Dr. Y. R. Lee was a tremendous help with experiments in Taiwan and knew all the best places to eat around the National Taiwan University. Tiffany Yeh helped us with experiments and all kinds of daily tasks that I thought were trivial until I tried to do them in Mandarin. The surface group at IAMS was great to talk to. In particular I would like to thank Dr. T. J. Chuang and Dr. J. C. Lin for the helpful ideas that came out of our discussions. Cheryl Longfellow was my constant companion in and out of the lab, and I want to thank her for asking me to go to Taiwan with her and teaching me interesting things about IRMPD and photodissociation in general. Mrs. Hsui-Chuan Shaw made sure that we always saw Yuan when he came to visit IAMS, and helped us track him down in different parts of the world when necessary.

While in Asia, I had the opportunity to visit research institutes in China and Japan. I would like to thank Professor Fanao Kong for hosting us in Beijing and Professor Toshinori Suzuki for inviting me to the Institute for Molecular Science in Okazaki, where I had many helpful discussions about gas-surface dynamics.

I have enjoyed my collaboration with Dr. Robert Sinkovits, from whom I learned about molecular dynamics simulations. I would like to thank Dr. Mark Cardillo, Dr. John Tully, and Dr. Alex Harris of AT&T Bell Laboratories for support and guidance throughout my last 5 years. I found it particularly helpful to

talk to them when deciding what experiments would be feasible on the GSM, and Dr. Cardillo's visits to Berkeley always gave me a boost of confidence when I needed it most. I would also like to thank AT&T Bell Laboratories for a Ph.D. Scholarship.

I was first introduced to the field of surface chemistry in Professor Brian Bent's lab at Columbia University. Brian taught me everything from tightening conflat bolts and swagelocks to how to plan a good experiment and think about data. Everything I learned from Brian and his two senior graduate students, Cindy Jenks and Chao-Ming Chiang, was immensely useful in graduate school. Professor George Flynn inspired me to change my major from math to chemistry in college and continues to be full of great "free advice". He has also been a great role model, and I have tried to emulate him when teaching at Berkeley. Hannah Sevian was first my physical chemistry TA and then one of my closest friends and has always given me a good perspective on life in graduate school at Berkeley.

During my last years in Berkeley, Nerine Cherepy and Erica Kuo gave me something to look forward to when coming home from the lab. I also enjoyed our lunches with Marcia Ziegeweid, who was always full of information about postdocs and jobs as well as funny stories.

I owe my education to my family. My Mother first introduced me to fun toys in her lab when I was a child, and I want her to know that all those late nights she spent teaching me physics and chemistry have indeed paid off! My Father taught me math and writing and kept me from giving up at times when my morale

was low. My Uncle, Gerald Smoliar, always kept up with my research and was the first person to teach me about computers.

This project was generously supported by the Office of Naval Research through Dr. Richard Miller.

Chapter 1

Introduction

The dynamics of collisions between gaseous molecules and a solid surface are of fundamental importance for understanding gas-surface reactions.[1] The work presented here explores gas-surface interactions at the molecular level, both unreactive and reactive, with a focus on the role of energy transfer between the gas and the surface, energy partitioning in reaction products in the case of reactive collisions, and a mechanistic picture of the events taking place on the surface.

The use of supersonic atomic or molecular beams to study gas-surface dynamics has been well established.[2,3] The supersonic beam introduces gaseous atoms or molecules into the collision zone with a well defined velocity. In the hyperthermal scattering of rare gaseous atoms of Chapters 2 and 3, the incident energy of the atoms is well controlled by using the seeded beam technique and adjusting the temperature of a resistively heated rhenium nozzle.[4] In addition, beams of reactive radical species can be introduced with well-defined incident energies. Reactive H and D atoms are used in the scattering experiments described in Chapters 4 and 5.

We built a machine called the "Gas-Surface Machine" (GSM) to do the experiments presented in this thesis. The machine, which is described in detail in

Chapter 2, allows for direct velocity measurement of particles as they evolve from the surface without undergoing any other collisions. The mass of the particles is also known, and so the translational energy is obtained. In the case of reactions, the translational energy distributions of individual reaction products from a complex system can be measured individually (Chapter 5). The translational energy distribution of the products reflects the dynamics of the last step in the gas-surface interaction. In the case of a inelastic scattering, the energy lost to the surface from different types of collisions is obtained. In the case of reactions, important features of the exit channel of the potential energy surface are revealed, such as whether there is a barrier and how energy is partitioned. The geometry of the GSM is such that the angle between the incident beam and the detector axis is always fixed at 90°. The angles θ_i, between the incident beam and the surface plane, and ϕ_i, the angle with respect to a direction along the lattice of the crystal (in the case where it is well defined, i.e. the [100] direction in LiF(001)), were varied so that $\theta_i + \theta_s = 90°$ and $\phi_s = \phi_i + 180°$. The change in scattered product flux with these angles gives a better understanding of the mechanisms for either energy loss (Chapters 2 and 3) or product formation (Chapters 4 and 5) occurring at the surface.

The ultimate goal we strived to achieve was to learn about the dynamics of individual reaction products from a gas-surface reaction. However, as we were working with a new machine and also wanted to understand the role of energy transfer in gas-surface collisions, we decided to start with a less complex system. Thus, we chose to start with hyperthermal scattering of rare gaseous atoms from

various alkali halide surfaces: LiF(001), NaCl(001), and CsI(rough). The rationale was that an understanding of energy transfer in collisions of unreactive systems would be important for later sorting out chemical and non-chemical effects in more complex reactive systems. In other words, we wanted to be able to later distinguish true chemical effects from purely mechanical ones when looking at the different features in a measured time-of-flight spectrum. As it turned out, the reactive systems studied involved H and D atoms, which are quite light, and so the mechanical effects are minimal. However, it is anticipated that if scattering with heavier atoms such as Cl or other halogens is explored in the future, mechanical energy transfer will be an important aspect of the observed dynamics when the collision energy is in the hyperthermal regime.

Chapter 2 describes the hyperthermal scattering of He atoms and Ne atoms from LiF(001) and NaCl(001). Time-of-flight spectra are measured for the atoms as they leave the crystal surface, and translational energy distributions are obtained that reflect how much energy the atom has left over after the collision event at the surface. The series of rare gas atoms: Ne, Ar, Kr, and Xe was used for hyperthermal scattering off a rough surface of CsI, and these experiments are reported in Chapter 3. In both these experiments, the ideas behind the binary collision models often used to describe classical collisions are tested.[1,5] In particular, the idea that the energy transfer in the collision is solely dependent on the masses of the collision partners and not the incident energy can be well tested by looking at a range of rare gases on different alkali halide surfaces.

The real goal of this project was to study reactive systems, and so the second half of this thesis describes the reaction dynamics of H or D atoms scattered from two different surfaces, LiF(001) and the basal plane of HOPG graphite. The kinetics of many gas-surface reactions have been studied effectively using molecular beams,[6-12] but the dynamics have not been as frequently explored. The dynamics of some reactions important to catalysis, such as the oxidation of CO on platinum and the oxidation of deuterium on platinum have been studied.[13-14] However, the reactions reported in Chapters 4 and 5 are etching reactions, where the substrate itself is one of the reactants. The dynamics of etching reactions have not been studied extensively. F. A. Houle has studied the dynamics of silicon etching by XeF_2, but in that case the reactant is introduced using an effusive beam and modulated beam techniques are used to monitor product evolution.[15] The dynamics of etching products from Cl_2 etching of GaAs(110),[16] Cl_2 etching of Si(111),[17] and Cl_2 etching of GaAs(100)[18] have been reported using similar time-of-flight techniques to what is used in this thesis.

In Chapter 4, the reaction of H(D) + LiF(001) is studied by measuring the time-of-flight of the HF or DF product of the gas-surface reaction. In addition to learning about the exit channel of the potential energy surface for this reaction, which has a barrier, the mechanism of the reaction is determined to be of the Eley-Rideal type. The Eley-Rideal mechanism refers to reactions that occur between a gaseous atom and a surface atom or surface adsorbate. The other common mechanism, more commonly reported for catalysis reactions, is the Langmuir-

Hinshelwood mechanism, which is a reaction between two adsorbed species on the surface to form a product that is then released into the gas phase.[19,20]

In Chapter 5, the reaction of D atoms with a graphite surface, producing CD_4, C_2D_2, and C_2D_4 is reported. C_2H_4 was not seen previously in modulated molecular beam work of the H + graphite reaction when an effusive source of H-atoms was used.[11] Here the D-atoms, produced in a supersonic beam, have an incident kinetic energy of ~7.5 kcal/mole and the flux is two orders of magnitude higher. The translational energy distributions for all three products are obtained, giving information about the potential energy surfaces involved in the three reactions. In addition, evidence for both the Eley-Rideal and Langmuir-Hinshelwood mechanisms is presented. In the case of CD_4 formation, there is evidence that both mechanisms operate simultaneously, while for C_2D_2 and C_2D_4, the Langmuir-Hinshelwood mechanism governs the reaction.

References

1. C. T. Rettner and M. N. R. Ashfold (Ed.), Dynamics of Gas-Surface Interactions (The Royal Society of Chemistry, London, 1991).
2. J. A. Barker and D. J. Auerbach, Surf. Sci. Rep. **4**, 1 (1984).
3. S. T. Ceyer, D. G. Gladstone, M. McGonigal, and M. T. Schulberg, Investigations of Surfaces and Interfaces-PartA (John Wiley and Sons, Inc., New York, 1993), pp. 383-452.
4. Details of the nozzle construction are presented in Chapter 4.
5. F. O. Goodman and H. Y. Wachmann, Dynamics of Gas-Surface Scattering (Academic Press, New York, 1976).
6. C. Su, Z. G. Dai, W. L. Luo, D. H. Sun, M. F. Vernon, and B. E. Bent, Surf. Sci. **312**, 181 (1994).
7. C. Su, H. Q. Hou, G. H. Lee, Z. G. Dai, W. Luo, M. F. Vernon, and B.E. Bent, J. Vac. Sci. Technol. B **11**, 1222 (1993).
8. C. Su, M. Xi, Z. G Dai, M. F. Vernon, and B. E. Bent, Surf. Sci. **282**, 357 (1993).
9. D. R. Olander, W. Siekhaus, R. Jones, and J. A. Schwarz, J. Chem. Phys. **57**, 408 (1972).
10. D. R. Olander, R. H. Jones, J. A. Schwarz, and W. J. Siekhaus, J. Chem. Phys. **57**, 421 (1972).

11. M. Balooch and D. R. Olander, J. Chem. Phys. **63**, 4772 (1975).

12. M. J. Vasile and F. A. Stevie, J. Appl. Phys. **53**, 3799 (1982).

13. C. A. Becker, J. P. Cowin, L. Wharton, and D. J. Auerbach, J. Chem. Phys. **67**, 3394 (1977).

14. S. T. Ceyer, W. L. Guthrie, T.-H. Lin, and G. A. Somorjai, J. Chem. Phys. **78**, 6982 (1983).

15. F. A. Houle, J. Chem. Phys. **87**, 1866 (1987).

16. L. A. DeLouise, J. Chem. Phys. **94**, 1528 (1991).

17. H. Yoshikawa and K. Shobatake, Chem. Phys. Lett. **223**, 341 (1994).

18. P. Bond, P. N. Brier, J. Fletcher, P. A. Gorry, and M. E. Pemble, Chem. Phys. Lett. **208**, 269 (1993).

19. J. I. Steinfeld, J. S. Francisco, and W. L. Hase, Chemical Kinetics and Dynamics (Prentice Hall International, Inc., London, 1989) p.196.

20. M. L. Yu and L. A. DeLouise, Surf. Sci. Rep. **19**, 285 (1994).

Chapter 2

Scattering of Hyperthermal Rare Gas Beams from Two Alkali Halide Surfaces

Introduction

We have investigated the energy transfer in collisions between hyperthermal rare gas atoms and the surfaces of alkali halide crystals using atomic beam surface scattering. In this chapter, the experimental results for the following four systems are addressed: He-LiF(001), Ne-LiF(001), He-NaCl(001), and Ne-NaCl(001). He atoms, with collision energies in the range [$3 < E_i$(kcal/mole) < 20], and Ne atoms, with collision energies in the range [$13 < E_i$(kcal/mole) < 66], were incident on each surface, and the time-of-flight spectra of the scattered atoms were recorded under single-collision conditions. The angles θ_i between the incident beam and the surface plane, and ϕ_i the angle with respect to the [100] surface direction, were varied with the detector fixed at 90° from the beam so that $\theta_i + \theta_s = 90°$ and $\phi_s = \phi_i + 180°$. By measuring the time-of-flight spectra of the recoiling atoms for a given incident beam energy, details about the dynamics and the energy transfer in the atom-surface collision are obtained.

Gas phase investigations of collisions between rare gas atoms and alkali halide molecules showed that the energy transfer could be distinguished for two different near collinear configurations and modelled by the impulse approximation.[1]

An important feature of the impulse approximation for the fractional energy transfer, $\Delta E/E$, is the dependence on the masses of the colliding species and the independence of collision energy:

$$\frac{\Delta E}{E} = \frac{4M_a M_b M_c (M_a + M_b + M_c)}{(M_a + M_b)^2 (M_b + M_c)^2} \leq 1, \tag{1}$$

where M_a is the mass of the free atom, M_b is the mass of the target atom in the diatomic molecule, and M_c is the mass of the second atom in the diatomic molecule. For example, the energy transfer in collisions between Xe and CsBr in the following two collinear configurations was quite different:

$$Xe + BrCs, \tag{2}$$

$$Xe + CsBr. \tag{3}$$

The experimental results showed 95% energy transfer for (2) and 61% energy transfer for (3), and predictions based on the impulse approximation were 95.0% for (2) and 60.7% for (3).[2]

To predict the energy transfer in the case of a free atom (M_a) hitting a surface atom (M_b), we let $M_c \rightarrow \infty$. The equation for energy transfer then becomes:

and is valid when $M_a \leq M_b$.[3,4] We have studied the scattering of He atoms and Ne

$$\frac{\Delta E}{E} = \frac{4M_a M_b}{(M_a + M_b)^2} \leq 1, \tag{4}$$

atoms from LiF(001) and NaCl(001) surfaces to determine if 1) the energy transfer is dominated by the impulsive collisions between the rare gas atoms and individual atoms comprising the alkali halide surface, 2) $\Delta E/E$ is independent of collision energy as predicted by this simple model, and 3) the model predicts the energy transfer from rare gas atoms of different masses to alkali halide salts containing different masses for the anion and cation. It is our hope that a full understanding of energy transfer in the hyperthermal regime of these non-reactive systems will help in future studies of reactive systems where chemical effects and non-chemical effects both play a role in the dynamics of the gas-surface interaction.[5]

While there is a wealth of data on the scattering of light rare gases, most frequently He atoms, from the surfaces of LiF and NaCl,[6] at low collision energies (on the order of several meV), the scattering in the energy range of up to 3eV has not been widely studied. Low collision energies were used to study diffraction, elastic, and inelastic scattering from these surfaces. The goal of these low energy inelastic scattering experiments was to understand the energy transfer to and from single phonon modes, and great pains were taken to minimize multi-phonon

scattering.[7] Our experiments, on the other hand, are in an energy regime where highly inelastic scattering events, involving the creation of a large number of phonons, can be studied. Such hyperthermal scattering has been studied for Xe scattered from the surfaces of GaAs(110), Ag(100), and Ge(100),[4] but there is no systematic study of the alkali halide salts. Saecker and Nathanson[8] have investigated the scattering of Ne, CH_4, NH_3, and D_2O with surfaces of perfluorinatedpolyether, glycerol, and squalane using similar beam-surface scattering experiments. These studies of atomic and molecular collisions with liquid surfaces show impulsive collision behavior and give insight into what functional groups the incoming gas particles see in collisions with the liquid surface.

In the experiments described in this chapter, the mechanisms of energy transfer from the incoming rare gas atom to the alkali halide surface are described. The time-of-flight spectrum of the recoiling atom reflects the amount of energy the particles retain after collision, and since the incident energy of the atomic beam is known, the energy transfer to the surface is easily calculated. The features in the time-of-flight spectrum reveal what types of energy loss occurred at the surface. It will be shown, for example, that Ne atom collisions with each surface show two distinct features whereas He atom scattering shows only one. From the large amounts of energy transferred to LiF(001) and NaCl(001), especially in the case of Ne atom scattering, it can be concluded that these crystals are not behaving as rigid walls. Rather, such highly inelastic collisions suggest that the crystal is

flexible, which is not surprising if many phonon modes are excited in the energy transfer process.

Experimental

The atomic beam surface scattering apparatus, shown schematically in Fig. 1, was used for the experiment. A continuous supersonic beam of rare gas atoms was produced and their time-of-flight after scattering from the surface of an alkali halide single crystal mounted on a three-axis rotatable manipulator was measured. The source-detector angle is fixed at 90°, and the crystal can be rotated to change the incident angle between the beam and the surface, θ_i, as well as the orientation of the [100] direction of the crystal, ϕ_i.

A resistively heated rhenium nozzle with a .007" diameter hole, described elsewhere,[9] is used to generate a supersonic beam of rare gas mixtures. Seeded beams were made with 1% He in H_2 and 0.6% Ne in H_2. The beam velocity and speed ratio were characterized for each mixture as a function of 1) stagnation pressure, and 2) the power used to heat the nozzle, on a crossed molecular beams apparatus by measuring beam time-of-flight using a spinning slotted wheel chopper and with the detector looking directly into the beam.[10] The time-of-flight data were fit to the following equation, which is appropriate for a supersonic beam:

$$N(v) = v^2 \exp(-\beta(v - v_0)^2), \tag{5}$$

where N(v) is a number density distribution of speeds; $\beta = m/2kT_s$, in $(m/s)^{-2}$,

characterizes the width of the distribution (where T_s is the "translational temperature" of the beam); and v_0 is the most probable velocity in the distribution, N(v). The beam energy is calculated from v_0. The speed ratio, $S= v_0(\beta)^{1/2} > 1$, characterizes the quality of the supersonic expansion.[11] The nozzle temperature was determined by measuring beam time-of-flight for pure Ne and also using optical pyrometry. The results of the characterization using beam time-of-flight measurements are shown in Fig. 2. The stagnation pressure was adjusted to create a good expansion as the temperature of the nozzle was increased. Speed ratios of 5-8 and 6-11 were obtained for the 1%He/H_2 and 0.6%Ne/H_2 mixtures, respectively.

The atomic beam source is differentially pumped by a 6,600 l/s diffusion pump backed by a 169 cfm mechanical booster pump (Edwards EH250F/E2M40F) in the source region,[12] which contains a .017" tungsten skimmer, and a 1,500 l/s diffusion pump in the differential region containing a .065" stainless steel skimmer. The main chamber is pumped by two liquid nitrogen baffled 3,000 l/s diffusion pumps. A three-axis rotatable manipulator equipped with a surface heater (Vacuum Generators) is mounted in the main chamber so that the axis of rotation lies perpendicular to and at the intersection of the molecular beam and the axis of the detector. A cross-correlation mechanical chopper wheel lies in between the surface and the detector to chop the atoms recoiling from the surface, allowing for time-of-flight measurements.[13] The flight length from the chopper wheel to the ionizer is 23.9 cm.[14] The UHV detector is a triply differentially pumped quadrupole mass

spectrometer (Extrel), with each region pumped by a 400 l/s magnetically suspended turbomolecular pump (Seiko-Seiki) collectively backed with a Diffstak (Edwards Model 63). A Brink type electron bombardment ionizer with an effective length of 1.5 cm, housed in a liquid nitrogen cooled copper insert, ionizes atoms (ionization efficiency is 10^{-4}) as they fly in from the interaction region. Electrostatic lenses guide newly formed ions entering and exiting the quadrupole filter, and a channeltron electron multiplier (Galileo) multiplies the ion signal. The pulses from the channeltron are sent to a multichannel scaler (Stanford Research SR430), which is interfaced through a GPIB interface (National Instruments) to a 486-25 PC, where time-of-flight data can be co-added and uncorrelated from the pseudo-random sequence of the cross-correlation chopper wheel.[13]

Results

For each surface, the time-of-flight spectra of recoiling He atoms and Ne atoms were taken as a function of incident energy, while holding the angles θ_i and ϕ_i fixed at 45° and 0°, respectively. The energy transfer as a function of collision energy was investigated in this measurement. The time-of-flight spectra were also taken at fixed collision energy and θ_i for varying ϕ_i. Some features of the time-of-flight spectra are more distinguishable at certain values of ϕ_i. Time-of-flight spectra were also measured at a fixed collision energy and ϕ_i over a range of θ_i, to determine whether energy is preferentially lost in the parallel or perpendicular directions to the surface. In all the following experiments, the integrated signal

from the time-of-flight spectra as a function of θ_i has a maximum at θ_i= 45°, indicating that energy is lost equally in the parallel and perpendicular directions to the surface. The results for the θ_i dependence of the time-of-flight spectra are independent of collision energy. Since the systems have the same θ_i dependence, only one example, the case of Ne atoms scattered from NaCl, is illustrated below.

Scattering from LiF(001)

He atom scattering from LiF(001) was measured in the range from 3-20 kcal/mole for θ_i= 45° and ϕ_i= 0°. The crystal temperature was maintained at 656-666 K to prevent adsorption of water or other background gases. Two time-of-flight specta are shown in Fig. 3, one for E_{coll}= 3 kcal/mole (Fig. 3a) and one for E_{coll}= 20 kcal/mole (Fig. 3b). The time-of-flight spectra for He atoms scattered from LiF(001) show only one peak. When the time-of-flight spectra from Fig. 3 are converted into translational energy distributions, Fig. 4, the peak energy and the maximum energy of the scattered beam can be determined by the leading edge in the time-of-flight spectrum. The translational energy distribution is calculated using the method of forward convolution, taking into account instrumental parameters such as the spread in the time-of-flight due to the width of the ionizer.[15]

In the low collision energy He atom time-of-flight spectra, it is clear that the maximum energy extends out beyond the incident beam energy, Fig.3a. In Figs.4a and 4b, two translational energy distributions are shown, corresponding to the two channels used in constructing the fit to the time-of-flight spectrum. The second

channel (Fig.4b) is a Maxwell-Boltzmann distribution for the surface temperature of the crystal, and the first channel (Fig.4a) is adjusted so that the total fit matches the data. Notice that for the second channel, the Maxwell-Boltzmann distribution, the translational energy distribution extends out to energies corresponding to the leading edge of the time-of-flight spectrum. However, to get a good total fit, the first channel must also extend out to energies beyond the collision energy. There are therefor atoms that gain energy from the hot surface. This effect is reproduced in molecular dynamics simulations that were performed to try and better understand the experimental results.[16] The percentage of the energy transferred, $\%E_{trans.}$, based on the collision energy and the peak maximum in the translational energy distribution for recoiling atoms is calculated according to :

$$E_{trans.} = \frac{E_{coll} - E_{P(E)}}{E_{coll}}, \qquad (6)$$

and the results are in displayed as the open circles in Fig. 5.

The variation of the time-of-flight spectrum with ϕ_i was investigated at E_{coll}= 12 kcal/mole for θ_i= 20°, 45°, and 60°. There is not much of a shift in the leading edge of the time-of-flight with changing ϕ_i, however the intensity of the scattering peak decreases as ϕ_i is increased, Fig. 6. The change in the time-of-flight peak maximum with ϕ_i is quite small, especially for θ_i= 45°, in both the experiments and the simulations for He atom scattering. Variations of the spectra with ϕ_i are generally more clearly seen at small and large values of θ_i, i.e. away from θ_i= 45°.

Ne atom scattering from LiF(001) was investigated in the range of beam energies 13-66 kcal/mole. Time-of-flight spectra for the Ne atoms have a fast sharp peak and a slow tail. When these time-of-flight spectra are transformed into translational energy distributions, it is clear that there are two energy loss peaks, one that involves a relatively small energy loss (fast time-of-flight peak) and one that is almost 100% energy loss (slow time-of-flight peak). In Fig. 7a, a Ne atom time-of-flight is shown with a corresponding translational energy distribution for θ_i= 20° (Fig. 7b). At θ_i= 20° slow Ne atoms are clearly seen in the time-of-flight spectrum. The slow peak is not as clear in the time-of-flight spectrum when θ_i is closer to 45°, but is still seen when transforming the time-of-flight data into a translational energy distribution. The slow part of the time-of-flight spectrum cannot simply be fit to a Maxwell-Boltzmann distribution for the surface temperature in this case. The energy loss of Ne atoms was measured as a function of collision energy for fixed θ_i= 45° and ϕ_i= 0° with crystal temperatures in the range of 659-664 K. The results are presented as the open squares and diamonds in Fig. 5.

Time-of-flight data for E_{coll}= 45 kcal/mole were taken at θ_i= 20°, 45°, and 60° for ϕ_i values between 0° and 40°. The experimental findings show that at θ_i= 20° and 45° there is no noticeable ϕ_i dependence, but for θ_i= 60°, the peak position and leading edge of the time-of-flight change with ϕ_i, Fig 8. There is a small peak shift to longer times as ϕ_i increases from 0° to 40°. In addition, the intensity for

the $\phi_i = 0^\circ$ peak is larger than the intensities for the larger values of ϕ_i, which are similar to one another.

Scattering from NaCl(001)

The collisional energy dependence of He atom scattering from NaCl(001) was investigated for beam energies in the range 3-20 kcal/mole. As in the case of scattering from LiF(001), only one time-of-flight peak is seen, corresponding to one peak in the translational energy distribution. Fig. 5 (filled circles) shows the results of the collisional energy dependence study for $\theta_i = 45^\circ$ and $\phi_i = 0^\circ$ with crystal temperatures from 640-654 K. Figs. 9a and 9b show example time-of-flight specta at 3 and 20 kcal/mole collision energies, respectively, and corresponding translational energy distributions are shown in Figs. 10a, 10b, and 10c. Again, the behavior of the He atoms scattered at low collision energies indicates that some energy is gained from the surface, just as in the case of He atoms scattered from LiF(001).

The scattering of Ne atoms from NaCl(001) in the range of 13-66 kcal/mole results in time-of-flight spectra with two contributions as seen for Ne atoms scattered from LiF(001), Fig. 11. The energy loss as E_{coll} is varied, determined by translational energy distributions, is summarized in Fig. 5 (filled squares and diamonds) for fixed $\theta_i = 45^\circ$ and $\phi_i = 0^\circ$ with crystal temperatures of 640-651 K.

The ϕ_i dependence of Ne atom scattering from NaCl(001) was investigated for $\theta_i = 20^\circ$, 45°, and 60° at a collision energy of $E_{coll} = 45$ kcal/mole. The ϕ_i

dependence is shown in Fig. 12 for $\theta_i = 60°$, where the time-of-flight peak is shifted (both the peak maximum and leading edge) to shorter times for $\phi_i = 0°$ as compared to $\phi_i = 40°$. Also, the peak intensity is greatest for $\phi_i = 0°$ and least for $\phi_i = 40°$.

Time-of-flight spectra taken for Ne atoms scattered from NaCl(001) for a range of θ_i and a collision energy of 13 kcal/mole was measured by integrating the area under each time-of-flight spectrum for every value of θ_i while holding $\phi_i = 0°$ and the crystal temperature at 654-656 K. As can be seen from Fig. 13, the maximum intensity is at 45°. This behavior was seen for the other systems as well. Keep in mind that the source-to-detector angle is fixed at 90°, so that the angular distribution is not the total flux as would be the case if the detector measured scattering over the entire solid angle that originates from the interaction region.

Discussion

In the classical impulsive collision model, energy transfer is dependent on the masses of the collision partners involved and not on the collision energy. The energy transfer to a surface based on Eqn. 4 results from a simple billiard ball type picture. In this simple picture the energy transfer between the incoming atom and an ion sitting on the surface of the crystal can be calculated. The predicted energy transfer from this calculation for different atom-ion collisions is shown on the right side of Fig. 5 (93% for He-Li; 57% for He-F; 50% for He-Na; 36% for He-Cl; ~100% for Ne-F; 99% for Ne-Na; and 93% for Ne-Cl; $M_a > M_b$ for Ne-Li). However, if the geometrical constraints on the incoming atom as it approaches the

salt ions are considered, it is clear that the incoming He atom or Ne atom will not easily access an exposed cation in the salt in the case of a perfectly flat surface, Fig. 14. In both LiF(001) and NaCl(001), the anion eclipses the cation. The ionic radii in LiF are r_{Li+}= 0.60 Å and r_{F-}= 1.36 Å; in NaCl they are r_{Na+}= 0.95 Å and r_{Cl-}= 1.81 Å.[17] The incoming particles, He atoms and Ne atoms, have atomic radii of ~1.5 and 1.58 Å, respectively. Thus, an incoming He atom or Ne atom will not see an exposed Li^+ or Na^+ unless the cation is sitting at an exposed terrace site, where it is not eclipsed by any anion neighbors. This explains why two distinct peaks are not seen for He atoms scattered from LiF(001) with one peak corresponding to impulsive He-Li collisions, for example.

He atom scattering from LiF(001) and NaCl(001) shows similar patterns of energy transfer, as seen in Fig. 5. The energy transfer for He atom scattered from LiF(001) falls short of the 57% predicted for an impulsive He-F collision, which could be due to two factors.[18] First of all, the surface is hot, and thus the energy transfer is expected to be reduced by an amount on the order of k_BT_s, where T_s is the surface temperature. Second, the predictions from Eqn. (4) result from a one dimensional model, and extending to three dimensions and averaging over impact parameter will reduce $\Delta E/E$. The energy transfer for He atoms scattered from NaCl(001) goes above the 36% predicted for a He-Cl collision. If Eqn. (4) is used to try to correlate the observed $\Delta E/E$ with multiple collisions, the observed $\Delta E/E$ would correspond to up to two sequential collisions. However, the amount of energy transfer steadily rises with collision energy in the range of 3-20 kcal/mole,

which is inconsistent with the impulsive model.

Ne atom scattering from LiF(001) and NaCl(001) was different from He atom scattering in that two types of energy loss were clearly observed instead of just one. In both cases, the fast time-of-flight peak corresponded to energy loss that is less efficient than what the impulsive model predicts for a simple gas atom-anion head-on collision. This first energy loss channel only increased moderately as the collision energy was increased from 13-66 kcal/mole, levelling off at higher collision energies to 65-70% energy transfer. The slow time-of-flight feature corresponds to more efficient energy loss, and more closely resembles what the impulsive model predicts. This energy loss channel does not change appreciably with collision energy. The atoms that undergo the second type of collision lose almost all memory of their incident velocity. They are sligtly faster than atoms that simply desorb from a surface at the surface temperatures used, but the broad distribution reflects the fact that the energy left in translation has a broad Maxwell-Boltzmann type distribution. The broad peaks in the time-of-flight also result from the fact that some atoms may undergo multiple collisions, and therefor a range of energy transfer is observed. Thus the time-of-flight is quite broad for the slow component. The slow recoiling Ne atoms are expected especially for Ne-F collisions, where the masses of the Ne atom and F atom are nearly equal; collisions between atoms of similar mass are the most efficient at transferring energy (in Eqn.4, as $M_a \rightarrow M_b$, $\Delta E/E \rightarrow 1$). However, a highly efficient energy transfer single collision cannot be distinguished from high energy loss due to

multiple scattering based on the time-of-flight data. This is one of the motivations for doing molecular dynamics simulations.

The faster time-of-flight peak for the Ne atom scattering off each salt results from a less efficient energy transfer collision. Since in the case if Ne atoms, $k_B T_s << E_{coll}$, the elevated surface temperature is not expected to lead to a significant decrease in the energy transfer. However, the effect of averaging over impact parameter, as already mentioned, still applies here. The reduced energy transfer would also occur if several atoms worked in concert, as a coupled set, during the collision, for then the incoming atom sees a greater effective mass as its collision partner. For example, in the Ne atom scattering from LiF(001) at 66 kcal/mole collision energy, the first channel resulted in 70% energy transfer to the surface (Fig. 5). So, if $\Delta E/E$ is set to 0.70 in Eqn. 4, the effective mass (M_{eff}) at the surface that the Ne atom collided with ($M_{eff}= M_b$) can be calculated to be M_{eff}~68. For 64% energy transfer, when E_{coll}= 45 kcal/mole, M_{eff}= 80. Although M_{eff} does not tell us which atoms are acting together, it is useful to see that as the $\Delta E/E$ gets larger, M_{eff} decreases. The width of the fast time-of-flight peak comes from scattering over a range of impact parameters governed by the local surface morphology, which includes steps and defects visible on the atomic level.[19]

The dependence of the time-of-flight spectra on the two angles, θ_i and ϕ_i, was explored for all the systems. For all four systems, He-LiF(001), Ne-LiF(001), He-NaCl(001), and Ne-NaCl(001), the largest integrated time-of-flight signal occurred at θ_i= 45° when the collision energy, ϕ_i, and the crystal temperature were

held constant. The shape of the θ_i dependence does not change in the range of collision energies studied here. For the fixed geometry in this experiment, and given that the θ_i behavior is independent of E_{coll} (i.e. the scattering lobe does not change with E_{coll}) this type of angular distribution indicates whether energy is lost preferentially in the parallel or perpendicualar directions to the surface. In Fig. 15, three types of θ_i dependences are shown: Case 1) energy is lost equally in both the parallel and perpendicular directions; Case 2) energy is preferentially lost along the direction perpendicular to the surface; Case 3) energy is preferentially lost in the direction parallel to the surface. As θ_i is changed from 45°, as shown in the figure, the detectable product vector also changes so that the entire lobe may be scanned within a given plane. Thus, the maximum in the lobe is found in the beam-detector plane. The assumptions here are that the scattering lobe is cylindrically symmetric, which is a reasonable assumption since scattering of this type usually gives a $\mathrm{Cos}^n\theta$ type distribution, and that the lobe does not change with incident angle.

The ϕ_i dependence was explored when it became apparent that the time-of-flight shifted with ϕ_i in the molecular dynamics simulations. The shift with ϕ_i is most easily seen for Ne atom scattering, especially in the case of Ne atoms scattered from NaCl(001), Fig. 12. Here, energy transfer is slightly less efficient when scattering is along the (001) direction of the lattice. This could perhaps be due to increased coupling to the nearest neighboring atoms along the (001) direction, creating a slightly higher M_{eff}. In all the cases shown in Figs. 6, 8, and 12, the scattering signal is greatest when $\phi_i = 0°$. Since the detector-to-source angle

is fixed in one plane at 90°, this indicates that more of the scattered atoms stay in the scattering plane along the (001) direction than along the other directions defined by ϕ_i.

Conclusion

The atomic beam surface scattering experiments described in this chapter show the different mechanisms of energy transfer for hyperthermal He atoms and Ne atoms colliding with LiF(001) and NaCl(001). He atom scattering for both surfaces shows only one distinguishable time-of-flight peak and similar energy transfer behavior as a function of collision energy.[20] For He atoms scattered from LiF(001), the $\Delta E/E$ approaches but falls short of the 57% predicted for an impulsive He-F collision. For He scattered from NaCl(001), the energy transfer goes above the 36% predicted for an impulsive He-Cl collision. In both cases $\Delta E/E$ rises with E_{coll}. Ne atom scattering differed from He atom scattering in that two contributions to the time-of-flight could be distinguished. Each Ne atom time-of-flight had a fast sharp peak and a slow broad peak. Once E_{coll} was about 20 kcal/mole, energy transfer did not change appreciably with collision energy, which is consistent with the impulsive model. The fast time-of-flight peak results from less efficient energy transfer than predicted by the impulsive model for atom-anion collisions, and can be rationalized as scattering from a coupled set of atoms working together as one collision partner. The slow time-of-flight peak, from atoms that lose almost all their energy to the surface, is consistent with an atom-

anion impulsive collision but could also be due to multiple collisions.

The dependence of scattering on the angles θ_i and ϕ_i showed that scattered flux was greatest for $\theta_i = 45^\circ$ and $\phi_i = 0^\circ$. A slight shift in the time-of-flight with varied ϕ_i, was also observed.

References and Notes

1. F. P. Tully, N. H. Cheung, H. Haberland, and Y. T. Lee, J. Chem. Phys. **73**, 4460 (1980).
2. B. H. Mahan, J. Chem. Phys. **52**, 5221 (1970).
3. F. O. Goodman and H. Y. Wachman, Dynamics of Gas-Surface Scattering (Academic Press, NewYork, 1976).
4. A. Amirav, M. J. Cardillo, P. L. Trevor, Carmay Lim, and J. C. Tully, J. Chem. Phys. **87**, 1796 (1987).
5. See Chapter 3.
6. Toennies, J. P, Dynamics of Gas-Surface Interaction (Springer Verlag, New York, 1982).
7. L. Mattera, M. Rocca, C. Salvo, S. Terreni, F. Tommasini, and U. Valbusa, Dynamics of Gas-Surface Interaction (Springer Verlag, New York, 1982).
8. M. E. Saecker and G. M. Nathanson, J. Chem. Phys. **100**, 3999 (1994); J. Chem. Phys. **99**, 7056 (1993).
9. See Chapter 4.
10. R. K. Sparks, Ph. D. Thesis, University of California, Berkeley (1979).
11. R. B. Bernstein, Chemical Dynamics via Molecular Beam and Laser Techniques (Oxford University Press, New York, 1982).
12. Mechanical booster pump donated by Genus Inc.

13. R. David, K. Kern, P. Zeppenfeld, and G. Comsa, Rev. Sci. Instrum. **57**, 2771 (1986).

14. Detector calibration was carried out to tune the electrostatic lenses and measure the flight length by photodissociating Cl_2 and Br_2 using 355 nm light from a Nd:YAG laser. Since the Newton circle for the recoiling fragments is so large compared to the velocity vector for the molecular beam, and the bond dissociation energies are well known, photofragment spectra taken at 90° could be used to measure the flight length by fitting the time-of-flight data to a translational energy distribution in the form of a δ-function for the proper energy release, given by the difference in the photon energy and the bond dissociation energy.

15. A. M. Wodtke, Ph. D. Thesis, University of California, Berkeley, 1986; X. Zhao, Ph. D. Thesis, University of California, Berkeley, 1988; J. D. Myers, Ph. D. Thesis, University of California, Berkeley, 1993.

16. Molecular dynamics simulations were performed by R. S. Sinkovits.

17. L. Pauling, The Nature of the Chemical Bond, 3rd Edition (Cornell University Press, Ithaca, New York, 1980).

18. J. Harris, Dynamics of Gas-Surface Interactions (The Royal Society of Chemistry, London, 1991).

19. Atomic force microscopy has been used to look at the crystal morphology before and after scattering.

20. Note that in the He atom scattering, a small Maxwell-Boltzmann component

may be hidden under the major time-of-flight peak, but it cannot be seen directly in either the time-of-flight or the corresponding translational energy distribution.

Figure Captions

Fig. 2-1 Gas-Surface Scattering Apparatus with channeltron (A), exit lenses (B), liquid nitrogen cooled copper insert (C), quadrupole filter (D), Brink type electron bombardment ionizer followed by entrance lenses (E), high-temperature rhenium nozzle (F), surface mounted on 3-axis rotatable manipulator (not shown) (G), cross-correlation chopper wheel (H), source region pumped by 6000 l/s diffusion pump (I), differential region pumped by 1000 l/s diffusion pump (J), main chamber pumped by two 2000 l/s diffusion pumps equipped with liquid nitrogen baffles (K, L), three regions of differential pumping on the detector pumped by three 400 l/s magnetically suspended turbomolecular pumps (T1, T2, T3).

Fig. 2-2 Beam characterization using the rhenium nozzle for 0.6%Ne/H_2 (solid squares) and 1% He/H_2 (solid circles) as well as nozzle temperature using neat Ne (open squares). See text for details of E_{beam} calculation from time-of-flight data.

Fig. 2-3 (a) Time-of-flight data (circles) for 3 kcal/mole He atoms scattered from LiF(001) taken at θ_i=45°, ϕ_i=0° and a surface temperature of 656 K. The two channels are derived from the translational energy distributions of Figs. 4a&b. Channel 2 (dashed line) is a Maxwell-Boltzmann distribution for the surface temperature, and channel 1 (dotted line) is adjusted to make

the total fit (solid line) follow the data.

(b) Time-of-flight data (circles) for 20 kcal/mole He atoms scattered from LiF(001) taken at the same angles and a surface temperature of 661 K. The fit (solid line) corresponds to the translational energy distribution of Fig. 4c.

Fig. 2-4 (a) Translational energy distribution for channel 1 of Fig. 3a.

(b) Translational energy distribution for channel 2 of Fig. 3a. This is a Maxwell-Boltzmann distribution for 656 K, the surface temperature.

(c) Translational energy distribution for Fig. 3b.

Fig. 2-5 Energy transfer as a function of collision energy for the systems studied: He atoms scattered from LiF(001) θ_i=45°, ϕ_i=0°, crystal temperature=656-666K (open circles); He atoms scattered from NaCl(001) θ_i=45°, ϕ_i=0°, crystal temperature=640-654K (filled circles); Ne atoms scattered from LiF(001) θ_i=45°, ϕ_i=0°, crystal temperature=659-664K fast TOF peak(open squares) and slow TOF peak (open diamonds); Ne atoms scattered from NaCl(001) θ_i=45°, ϕ_i=0°, crystal temperature=640-651K fast TOF peak(filled squares) and slow TOF peak (filled diamonds); predictions for impulsive collisions between incoming He atoms and Ne atoms and individual surface atoms in the LiF(001) and NaCl(001) surfaces (filled triangles).

Fig. 2-6 The ϕ_i dependence of He atom scattering from LiF(001). He atoms scattered at 12 kcal/mole with θ_i= 60°, a surface temperature of 659-661 K, and ϕ_i= 0° (inverted triangles), ϕ_i= 20° (diamonds), ϕ_i= 30° (squares), and ϕ_i= 40° (circles).

Fig. 2-7 (a) Time-of-flight data (circles) for Ne atoms scattered from LiF(001) with E_{coll}= 45 kcal/mole, θ_i= 20°, ϕ_i= 0°, and $T_{surface}$= 666 K. The fit (solid line) is derived from (b).

(b) Corresponding translational energy distribution, showing two distinct peaks.

Fig. 2-8 The ϕ_i dependence of Ne atom scattering from LiF(001). Ne atoms scattered at 45 kcal/mole with θ_i=60°, a surface temperature of 647-652 K, and ϕ_i= 0° (inverted triangles), ϕ_i= 20° (diamonds), ϕ_i= 30° (squares), and ϕ_i= 40° (circles).

Fig. 2-9 (a) Time-of-flight data (circles) for 3 kcal/mole He atoms scattered from NaCl(001) for θ_i=45°, ϕ_i=0°, and $T_{surface}$= 641 K. The two channels are derived from the translational energy distributions of Figs. 10a and 10b. Channel 2 (dashed line) is a Maxwell-Boltzmann distribution for the surface temperature, and channel 1(dotted line) is adjusted to make the total fit (solid line) fit the data.

(b) Time-of-flight data (circles) for 20 kcal/mole He atoms scattered from NaCl(001) at the same angles and a surface temperature of 654K. The fit corresponds to the translational energy distribution of Fig. 10c.

Fig. 2-10 (a) Translational energy distribution for channel 1 of part (a).

(b) Translational energy distribution for channel 2 of part (a).

(c) Translational energy distribution for part (b).

Fig. 2-11 (a) Time-of-flight data (circles) for 45 kcal/mole Ne atoms scattered from NaCl(001) at θ_i=20°, ϕ_i=30°, and $T_{surface}$= 616 K. The fit (solid line) is derived from (b).

(b) Translational energy distibution giving rise to the fit of part (a).

Fig. 2-12 The ϕ_i dependence of Ne atom scattering from NaCl(001). Ne atoms scattered at 45 kcal/mole with θ_i=60°, a surface temperature of 615-626 K, and ϕ_i= 0° (circles), ϕ_i= 20° (triangles), ϕ_i= 30° (diamonds), and ϕ_i= 40° (squares).

Fig. 2-13 Angular distribution for varied θ_i and fixed ϕ_i=0° of 13 kcal/mole Ne atoms scattered from NaCl(001). $T_{surface}$= 654-656 K.

Fig. 2-14 The LiF(001) and NaCl(001) lattices showing the relative sizes of the ions. This shows that the anion eclipses the cation in each lattice, making direct collision with Li atoms or Na atoms unlikely, except in the case of defect sites.

Fig. 2-15 Three types of scattering show how the θ_i dependence probes the scattering lobe in the source-detector plane. Case 1: energy is lost equally in the parallel and perpendicular directions to the surface; Case 2: energy is lost preferentilally in the perpendicular direction; Case 3: energy is lost preferentially in the parallel direction. The results in this paper all follow Case 1.

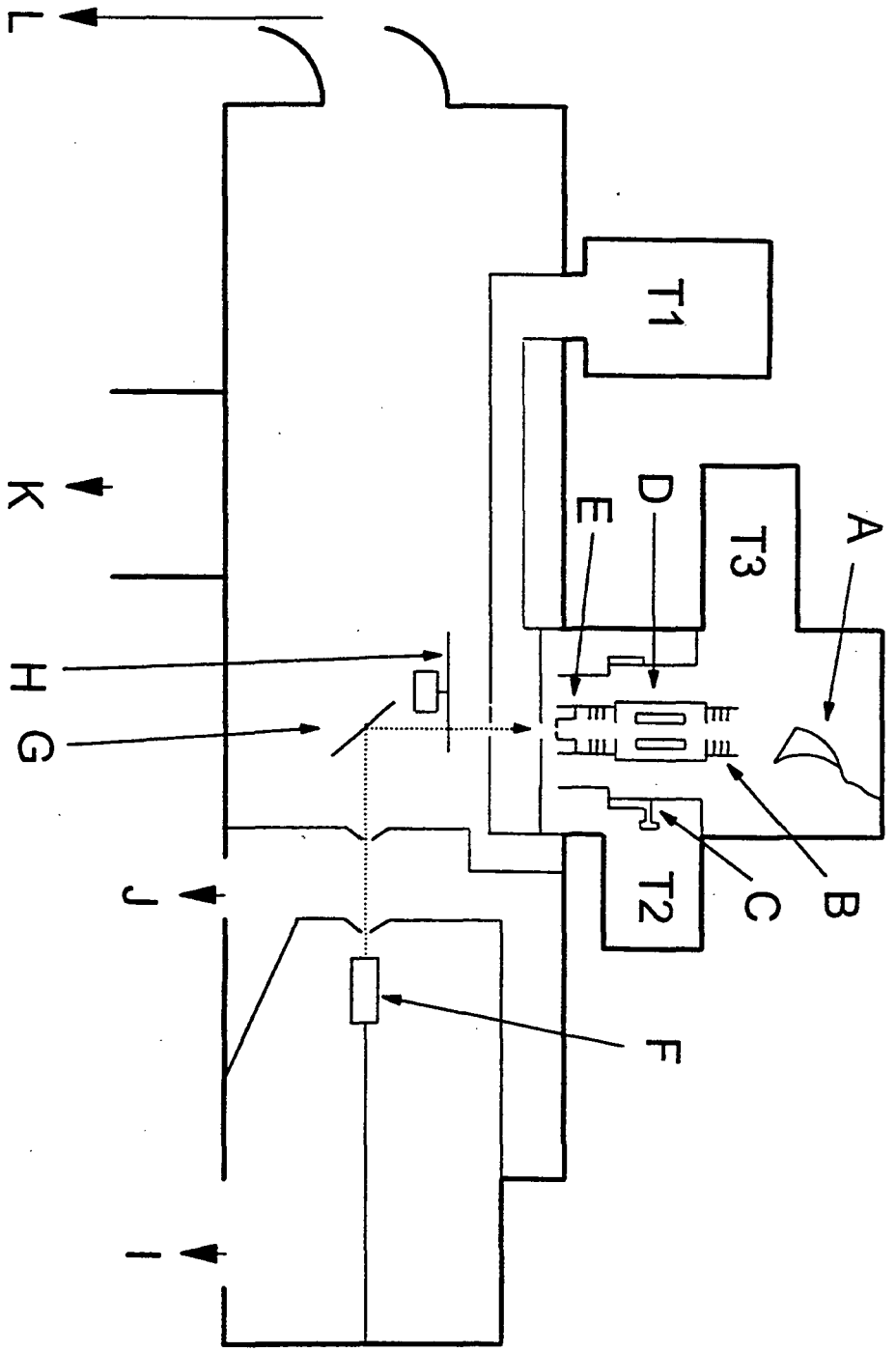

Figure 2-1

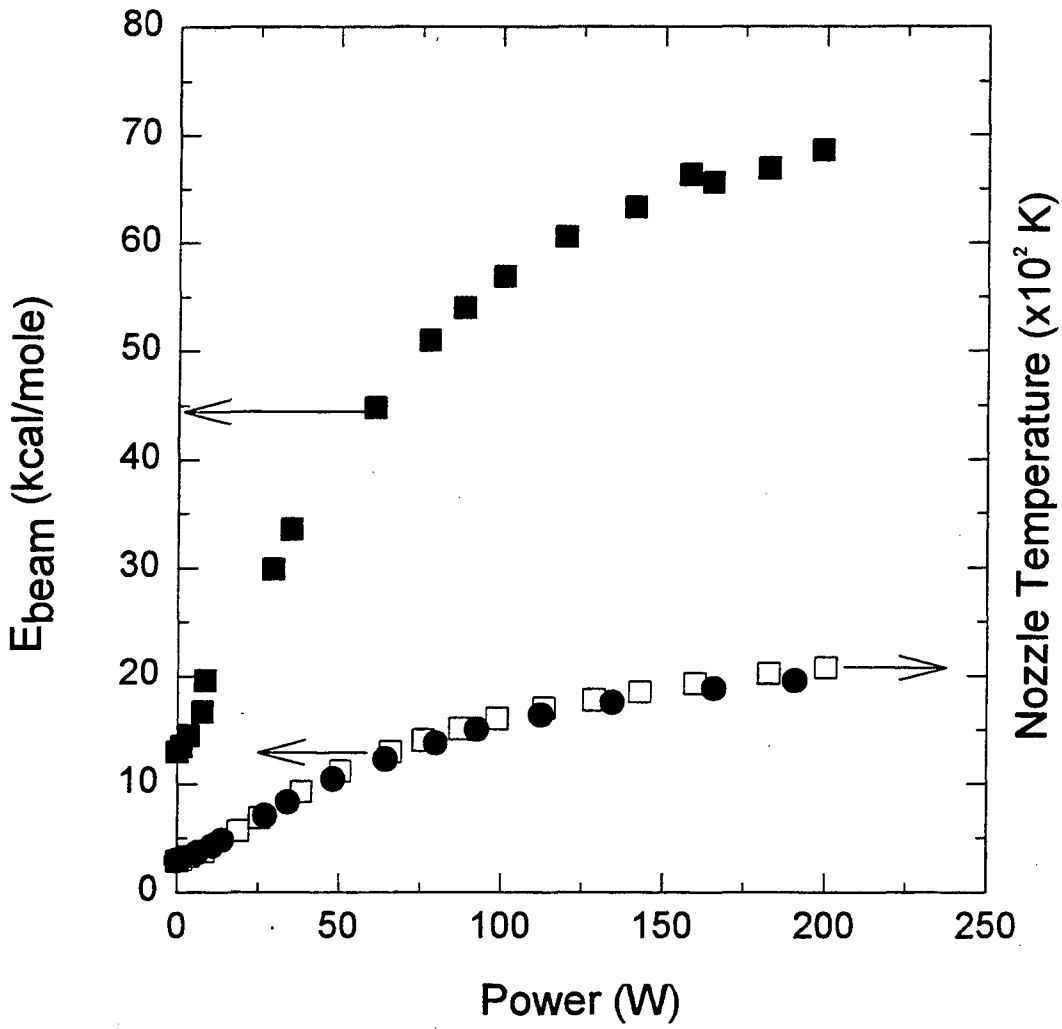
80
70
60
50
40
30
20
10
0
0
50
100
150
200
250
Power (W)
Ebeam (kcal/mole)
Nozzle Temperature (x10² K)

Figure 2-2

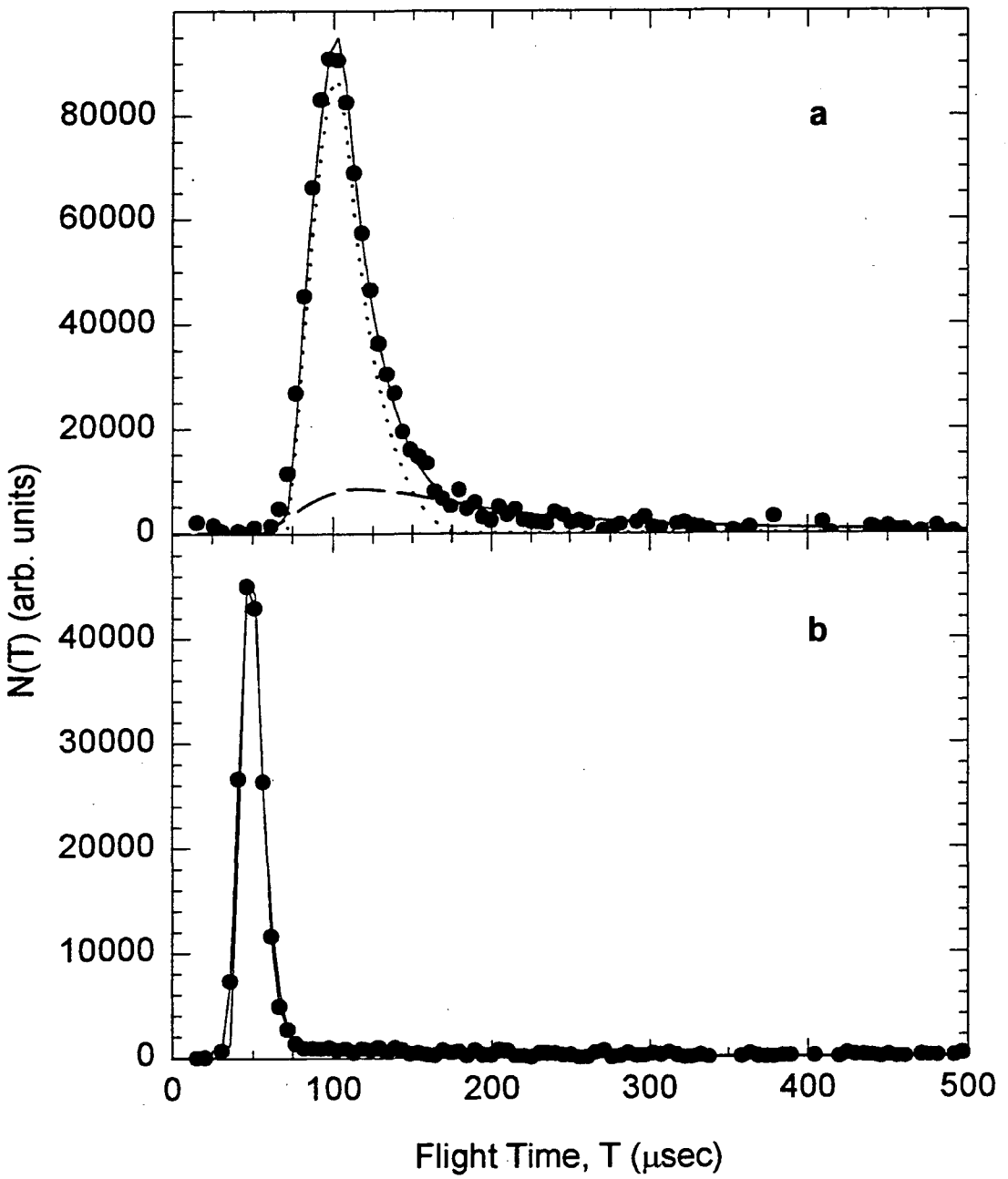
a
b
80000
60000
40000
20000
0
40000
30000
20000
10000
0
N(T) (arb. units)
0
100
200
300
400
500
Flight Time, T (μsec)

Figure 2-3

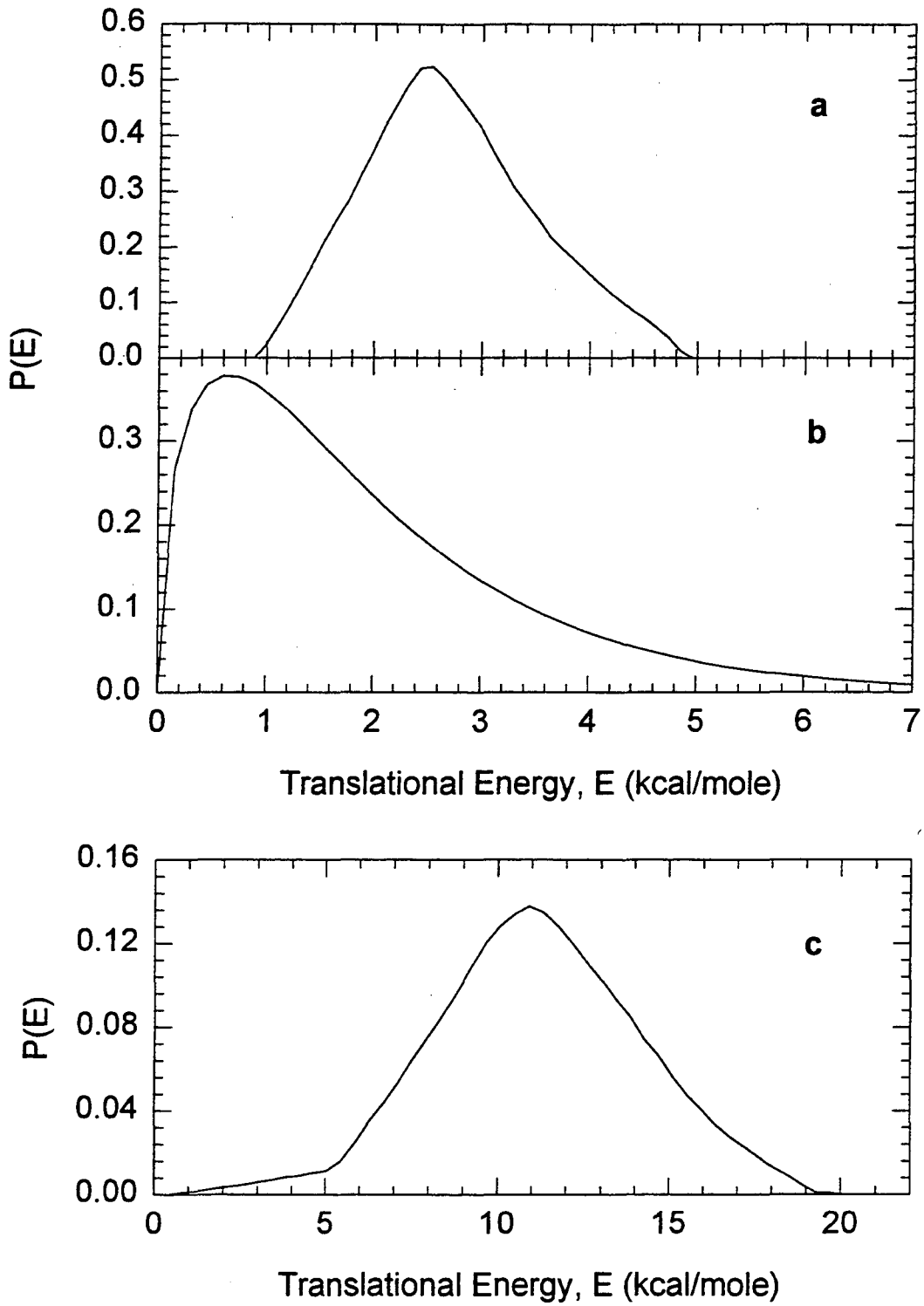
0.6
0.5
0.4
0.3
0.2
0.1
0.0
a
P(E)
0.3
0.2
0.1
0.0
b
0
1
2
3
4
5
6
7
Translational Energy, E (kcal/mole)
0.16
0.12
0.08
0.04
0.00
c
P(E)
0
5
10
15
20
Translational Energy, E (kcal/mole)

Figure 2-4

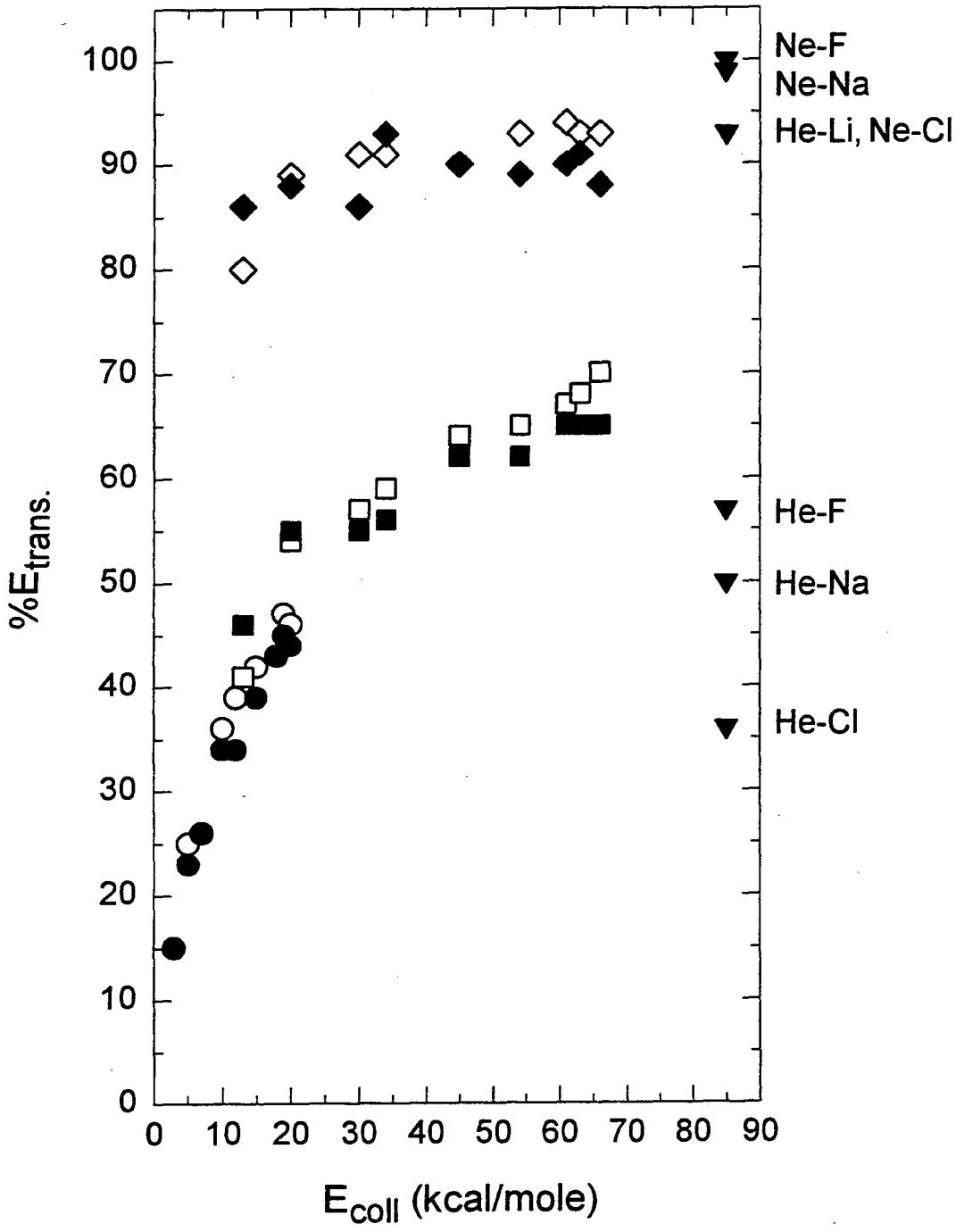
Ne-F
Ne-Na
He-Li, Ne-Cl
He-F
He-Na
He-Cl
%Etrans.
Ecoll (kcal/mole)
0
10
20
30
40
50
60
70
80
90
100

Figure 2-5

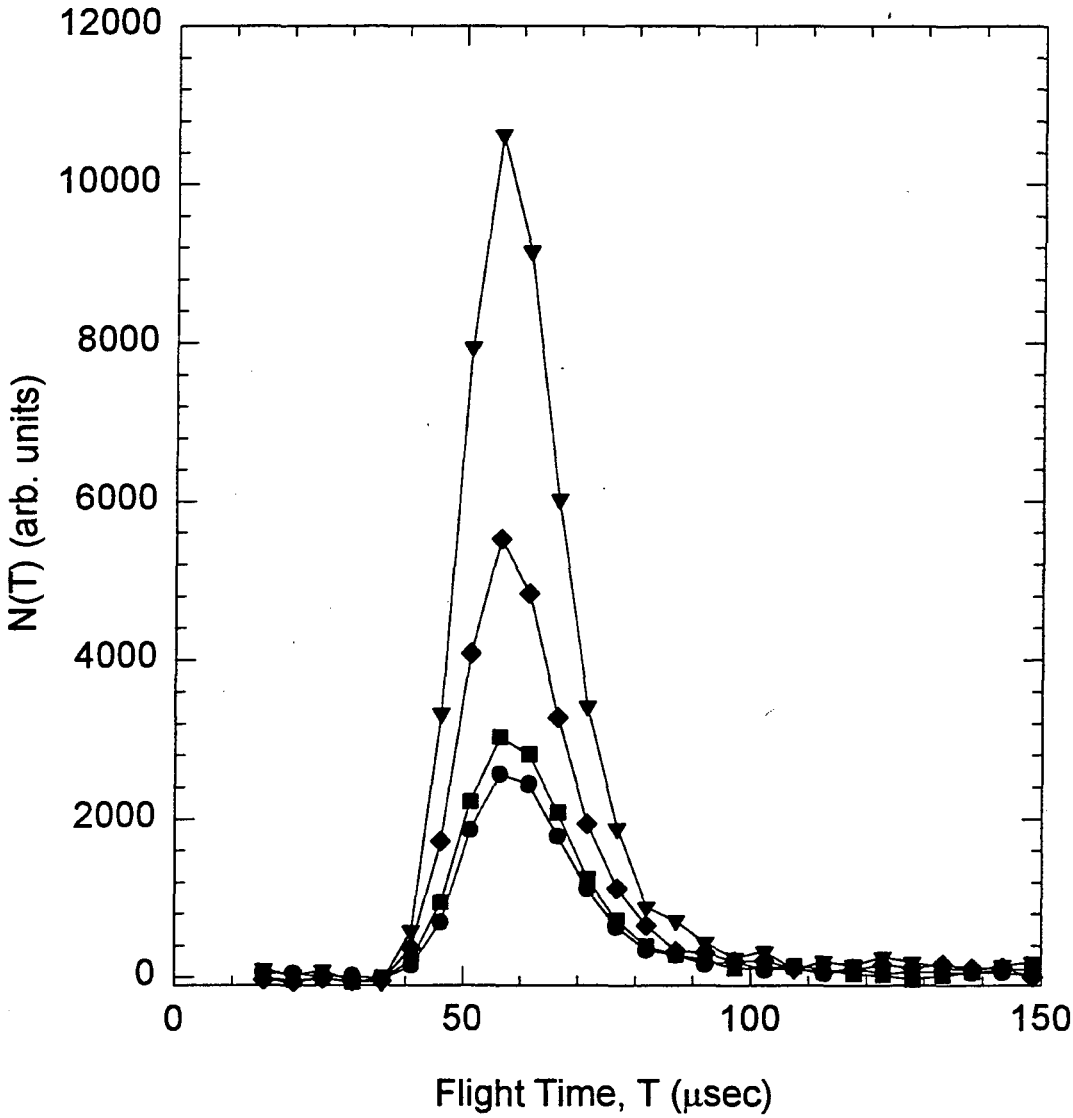
12000
10000
8000
6000
4000
2000
0
N(T) (arb. units)
0
50
100
150
Flight Time, T (μsec)

Figure 2-6

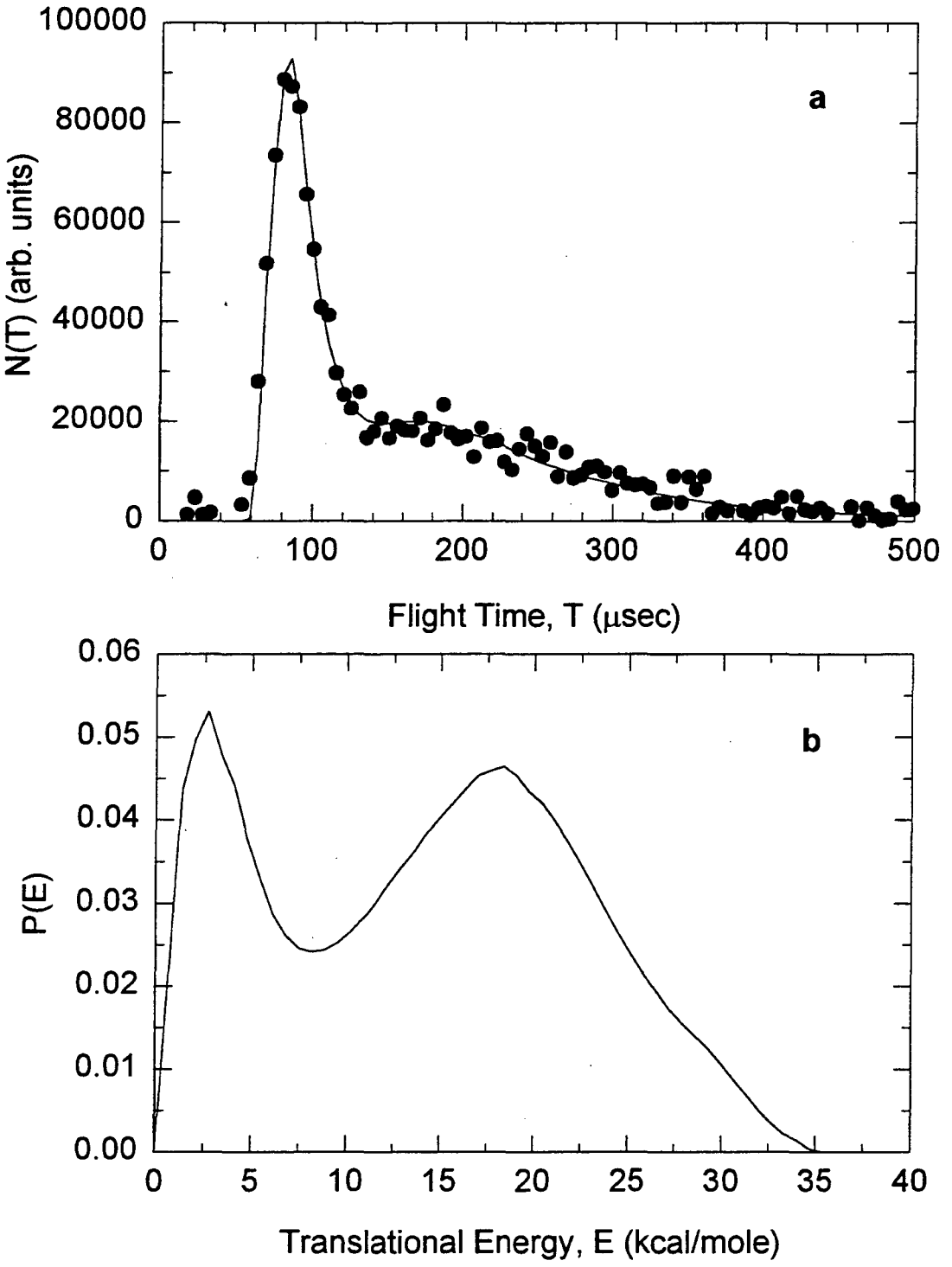
100000
80000
60000
40000
20000
0
N(T) (arb. units)
a
0
100
200
300
400
500
Flight Time, T (μsec)
0.06
0.05
0.04
0.03
0.02
0.01
0.00
P(E)
b
0
5
10
15
20
25
30
35
40
Translational Energy, E (kcal/mole)

Figure 2-7

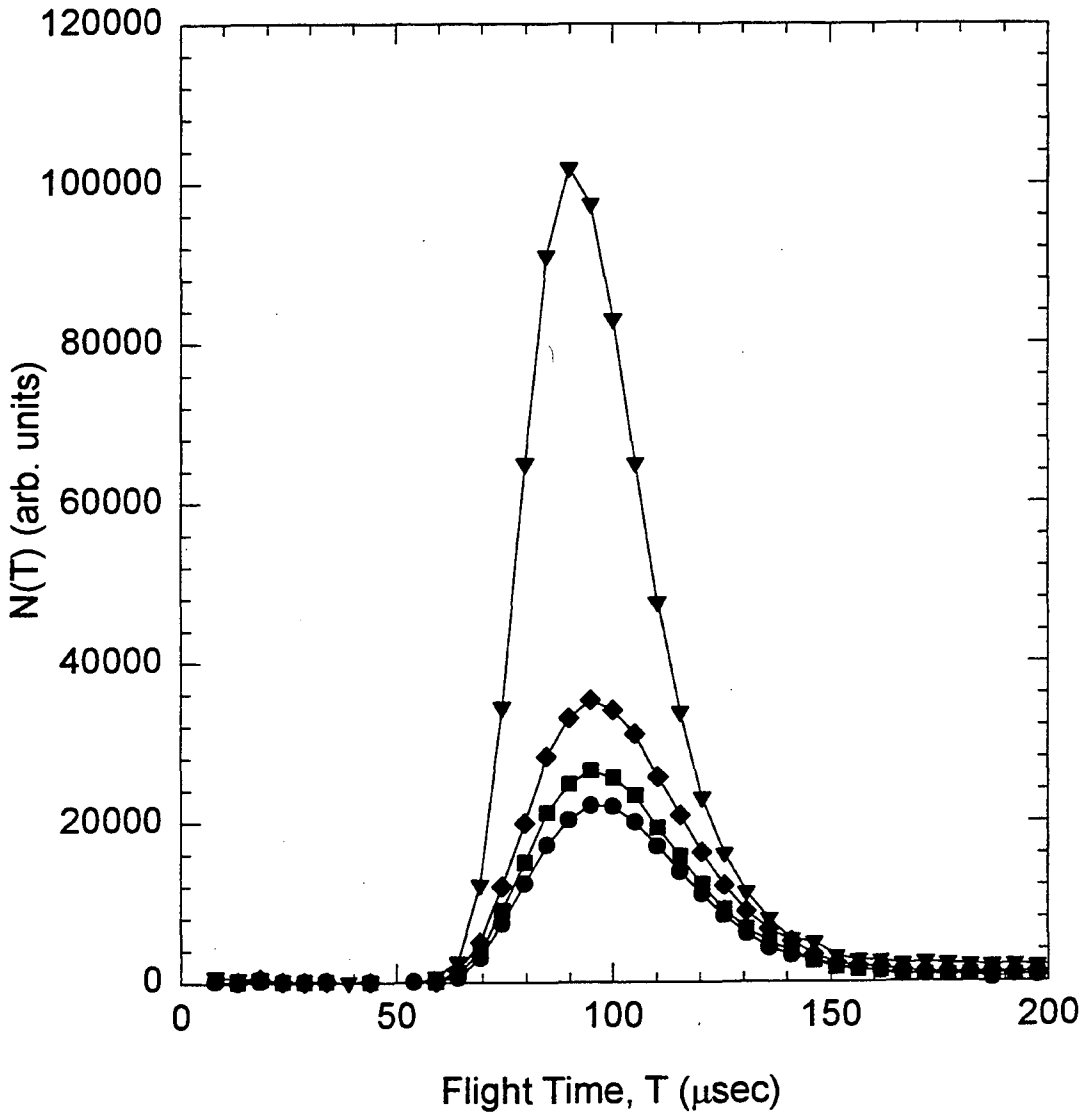
120000
100000
80000
60000
40000
20000
0
N(T) (arb. units)
0
50
100
150
200
Flight Time, T (μsec)

Figure 2-8

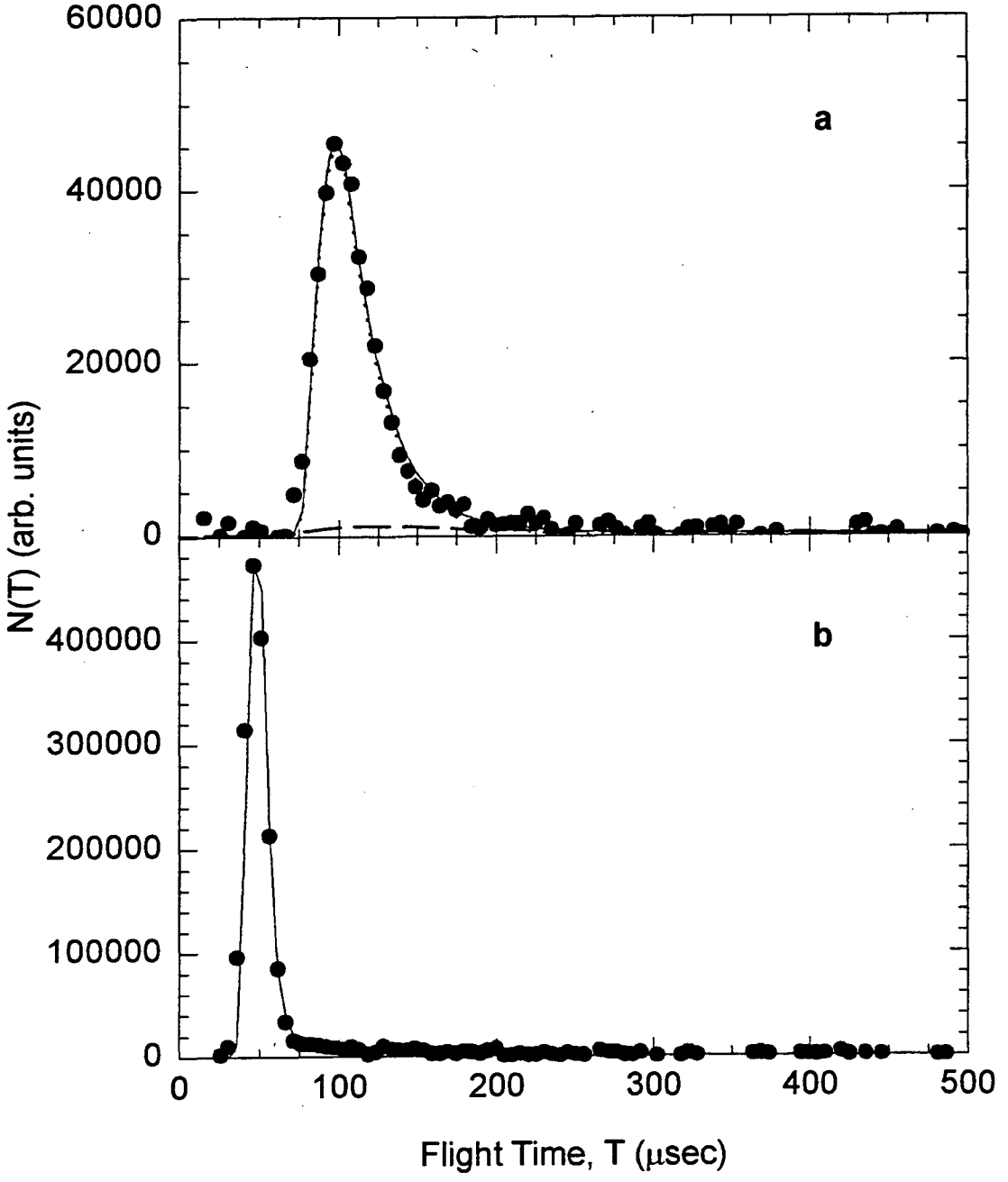
60000
40000
20000
0
a
400000
300000
200000
100000
0
b
N(T) (arb. units)
0
100
200
300
400
500
Flight Time, T (μsec)

Figure 2-9

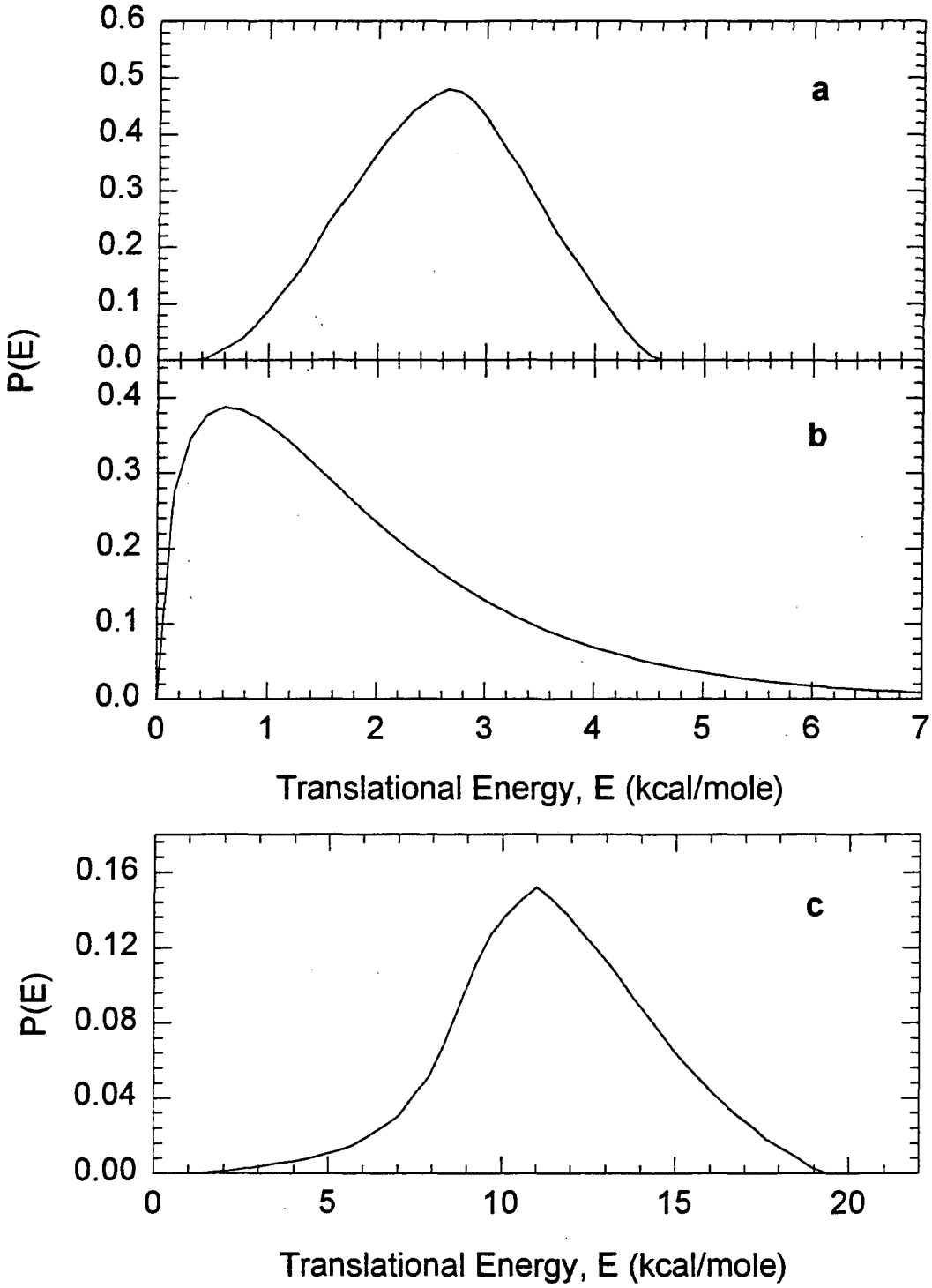
0.6
0.5
0.4
0.3
0.2
0.1
0.0
a
P(E)
0.4
0.3
0.2
0.1
0.0
b
0
1
2
3
4
5
6
7
Translational Energy, E (kcal/mole)
0.16
0.12
0.08
0.04
0.00
c
P(E)
0
5
10
15
20
Translational Energy, E (kcal/mole)

Figure 2-10

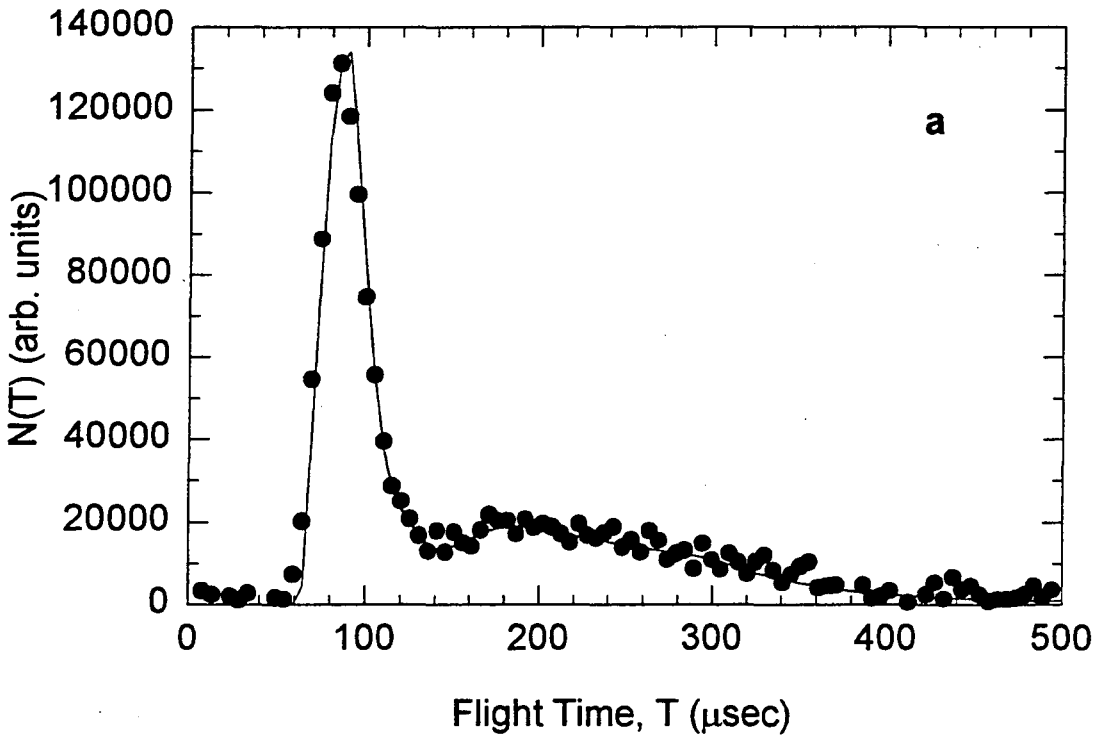
140000
120000
100000
80000
60000
40000
20000
0
N(T) (arb. units)
a
0
100
200
300
400
500
Flight Time, T (μsec)

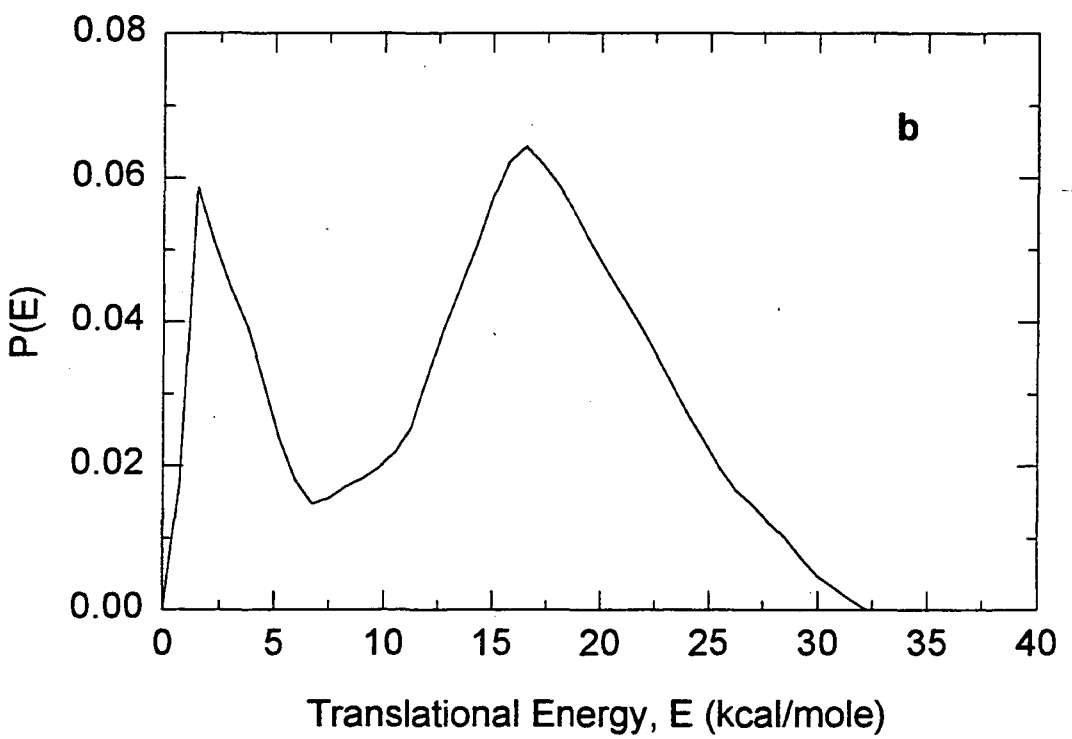
0.08
0.06
0.04
0.02
0.00
P(E)
b
0
5
10
15
20
25
30
35
40
Translational Energy, E (kcal/mole)

Figure 2-11

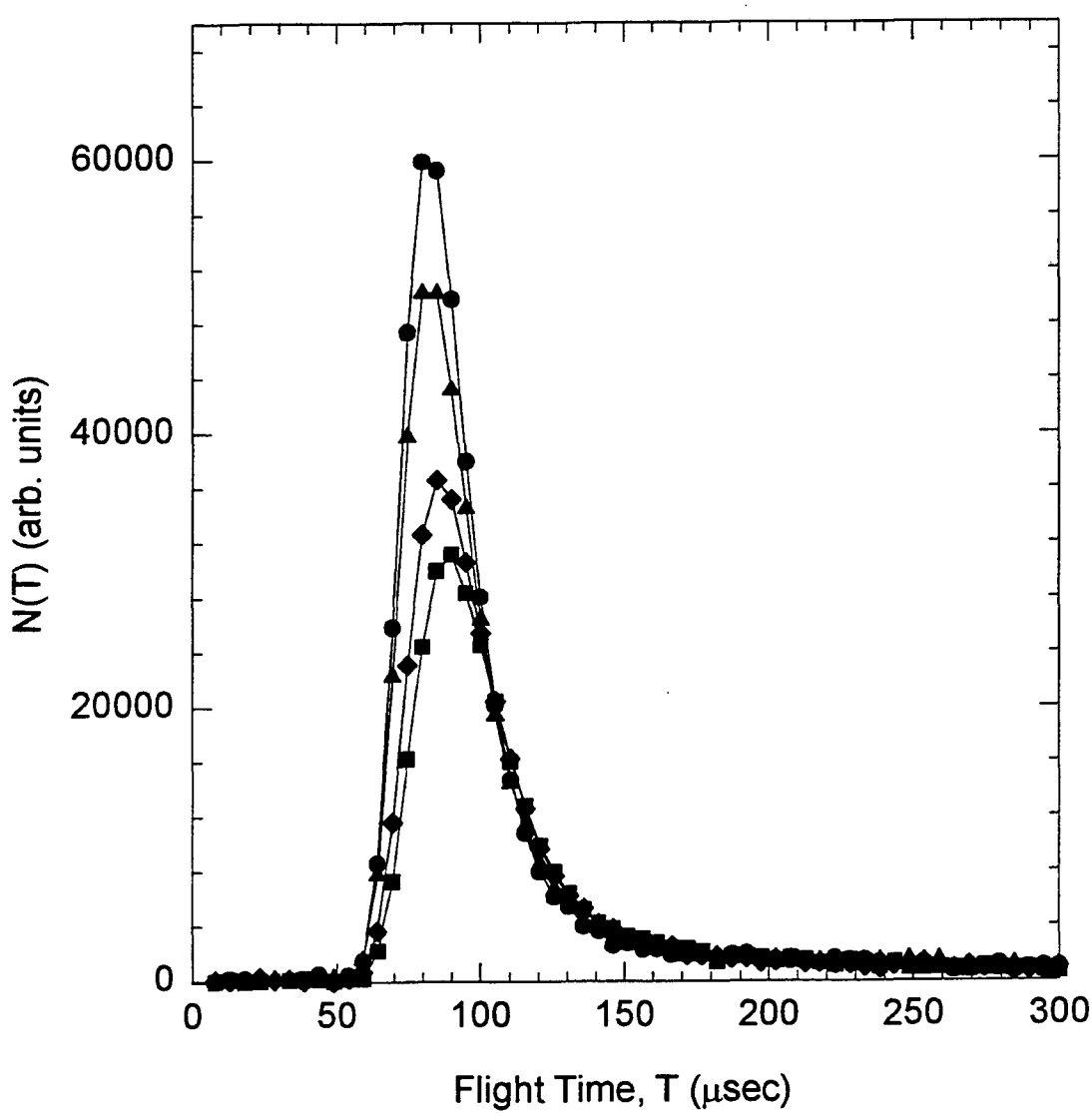
60000
40000
20000
0
N(T) (arb. units)
0
50
100
150
200
250
300
Flight Time, T (μsec)

Figure 2-12

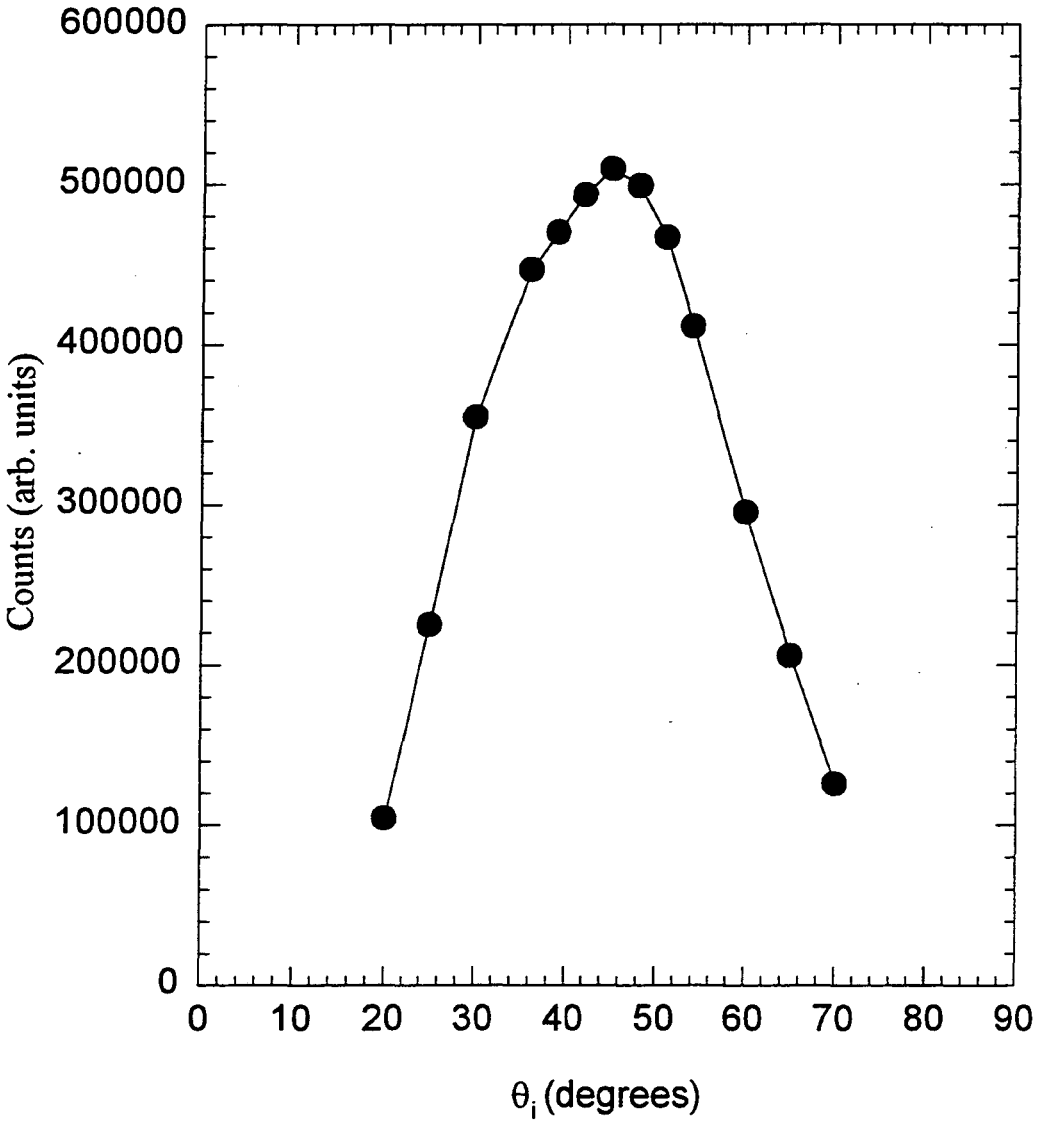
600000
500000
400000
300000
200000
100000
0
Counts (arb. units)
0
10
20
30
40
50
60
70
80
90
θi (degrees)

Figure 2-13

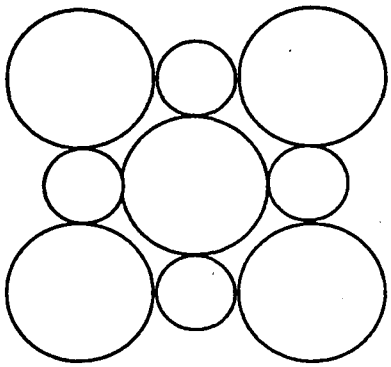

NaCl(001)

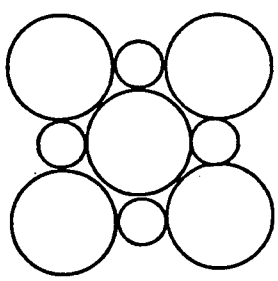

LiF(001)

Figure 2-14

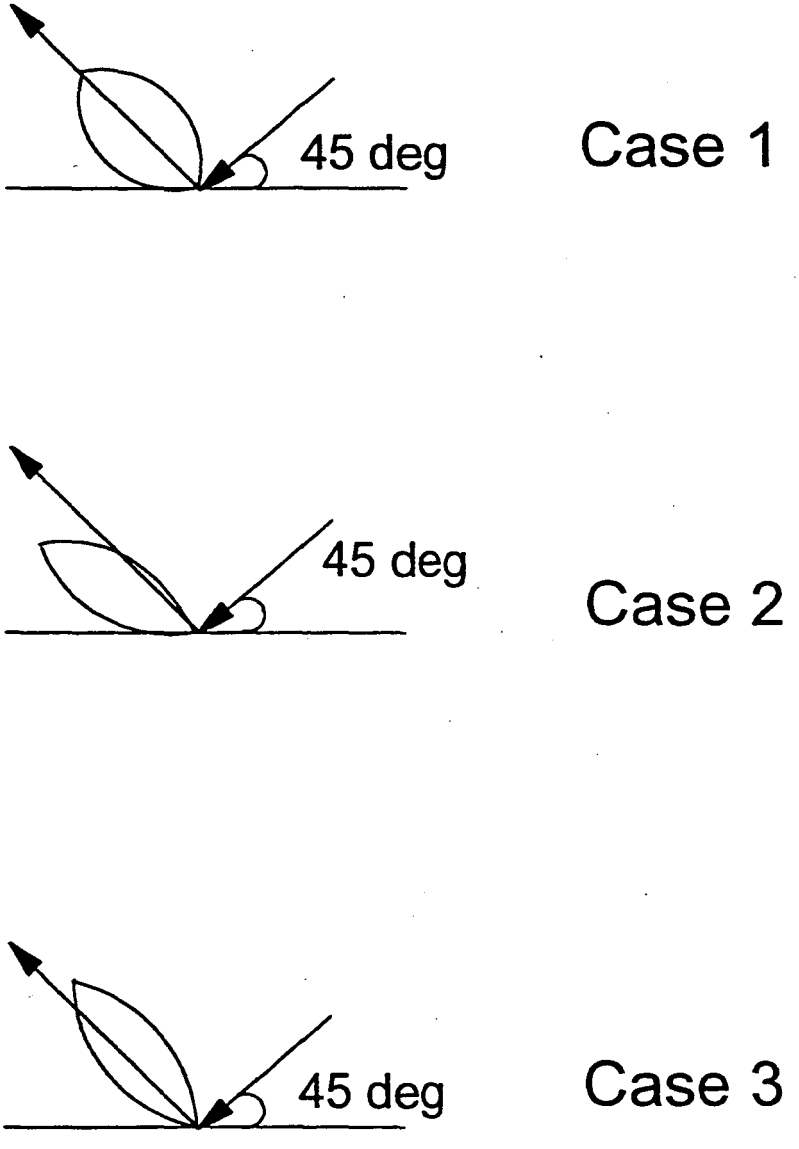

Figure 2-15

Chapter 3

Energy Transfer in the Scattering of Hyperthermal Rare Gas Beams from a CsI Surface

Introduction

Energy transfer in hyperthermal scattering of the rare gaseous atoms: Ne, Ar, Kr, and Xe from a CsI surface has been studied to further understand the mechanisms of energy loss in gas-surface collisions. This is an extension of our work on hyperthermal He atom and Ne atom scattering from LiF(001) and NaCl(001). In the hyperthermal energy regime, the masses of the collision partners are expected to be the most important parameter determining the efficiency of energy transfer. In CsI, the mass of Cs is greater than all the rare gaseous atoms used, and thus the condition that $\mu<1$ is always satisified, where

$$\mu=\frac{M_g}{M_s}, \qquad (1)$$

M_g is the mass of the gaseous atom, and M_s is the mass of the surface atom involved in the collision. The condition of $\mu<1$ is necessary for the expression for energy transfer in the impulse limit to hold:

where E_i is the incident energy.[1] In addition, for the I anion in CsI, the $M_I > M_{Ne}$,

$$\frac{\Delta E}{E_i} = \frac{4\mu}{(1+\mu)^2}, \qquad (2)$$

M_{Ar}, and M_{Kr}. If impulsive collisions are important, then when the mass of the incoming gaseous atom more closely matches the mass of a surface atom in the CsI crystal, the energy transfer in expected to be more efficient. In Eq. (2), this corresponds to the limit of $\mu=1$, where the fractional energy transfer, $\Delta E/E$, is 1. In addition, the value of $\Delta E/E$ should be independent of the incident collision energy.

As was found in the work on He atom and Ne atom scattering from LiF(001) and NaCl(001), simple impulsive collisions do not fully explain the energy transfer observed. Two distinct features appear in the time-of-flight spectra of the scattered atoms in certain ranges of collision energy. This points to more than one mechanism of energy transfer. The trend in energy transfer with mass qualitatively follows the predictions of the impulse approximation, though, and the model is useful in trying to understand the way energy is lost to the surface.

Unlike LiF and NaCl, CsI does not naturally cleave along a lattice plane, and so although a single crystal was used, the surface was rough. A rough surface can lead to more multiple collision energy loss. Also, measuring an angular distribution is less helpful than in the case of LiF(001) and NaCl(001) since the surface plane is not as well defined. The angular distributions are so broad that it is often hard to define an angle of maximum flux. In the LiF(001) and NaCl(001) scattering, this was useful for determining whether energy was lost preferentially in the directions parallel or perpendicular to the surface.

Very little experimental work has tested the impulse approximation or explored energy transfer in the hyperthermal regime in a systematic way for neutral particles hitting a surface. Winters et al. studied the collisions of He, Ar, and Xe atoms colliding with a Pt(111) surface using supersonic beams, though.[2] They also studied the ion-surface collisions between He^+, Ar^+, and Xe^+ colliding with a gold film. They report mean final translational energies of the atoms and ions after they scatter from the surface and the fraction of energy lost to the surface, but there are no time-of-flight spectra shown and so presumably distinctive features showing different mechanisms of energy loss were not observed. The energy loss is discussed in terms of binary collisions. Other previous work on hyperthermal scattering has been discussed already in Chapter 2.

Experimental

We measured the energy transfer with the same atomic beam surface scattering apparatus used for the He atom and Ne atom scattering from LiF(001) and NaCl(001) (see Chapter 2). In this experiment, however, a wider range of rare gases and a CsI crystal was used. Seeded beams of Ne, Ar, Kr, and Xe were expanded to form supersonic beams, and each beam was characterized for 1) stagnation pressure, and 2) the power used to heat the nozzle, on a crossed molecular beams apparatus by measuring beam time-of-flight using a spinning slotted wheel as a chopper with the detector looking directly into the beam. The time-of-flight data were fit to the following equation, which is appropriate for a

supersonic beam:

$$N(v) = v^2 \exp(-\beta(v-v_0)^2), \quad (3)$$

where N(v) is a number density distribution of speeds; $\beta = m/2kT_s$, in $(m/s)^{-2}$, characterizes the width of the distribution (where T_s is the "translational temperature" of the beam); and v_o is the most probable velocity in the distribution, N(v). The beam energy, which is the collision energy, E_{coll}, in the scattering event, is calculated from v_o.[3] The range of E_{coll} depends on the rare gas used: for Ne atoms E_{coll}=13-63 kcal/mole, for Ar atoms E_{coll}=10-58 kcal/mole; for Kr atoms E_{coll}=13-73 kcal/mole, and for Xe atoms E_{coll}=16-95 kcal/mole. The nozzle stagnation pressure was adjusted to create a good expansion as the temperature of the nozzle was increased. The speed ratio, S, where

$$S = v_o \beta^{\frac{1}{2}} > 1, \quad (4)$$

was determined for each mixture at many beam energies. The following speed ratio ranges were obtained: for 0.6%Ne/H_2 S=6-11, for 4%Ar/He S=7-11, for 5%Kr/He S=8-11, and for 5%Xe/He S=9-14. The nozzle temperature was determined by measuring beam time-of-flight for a neat Ne beam and also using optical pyrometry. The beam characterization results are shown in Fig. 1.

The single crystal CsI (Atomergic) was not cleaved because CsI has no natural cleavage plane. A rough surface was used, and the crystal was heated in vacuum for 24 hours at T_{surf}= 750-800 K. This removes impurities such as water

and also anneals the crystal. The surface was maintained at T_{surf}= 630-640 K during the experiment to prevent the adsorption of background gases.[4]

As in Chapter 2, the time-of-flight spectra of the Ne, Ar, Kr, and Xe atoms were measured after scattering from the crystal by placing a chopper wheel between the surface and the detector. The flight length was 23.9cm, and a cross-correlation chopper wheel was used as before. Time-of-flight spectra were measured for each angle, θ_i, between the incident beam and the surface (see Chapter 2).

Results

Time-of-flight spectra were measured for fixed collision energies, E_{coll}, and angles θ_i. Each θ_i distribution was measured with E_{coll} held constant. (The dependence on the angle ϕ_i was not measured since the surface is not a well-defined lattice plane in this case. In the case of LiF(001) and NaCl(001), ϕ_i was the angle of the incoming beam with respect to the [100] surface direction.)

The time-of-flight spectra of the different rare gases incident with the same collision energy clearly show different energy transfer behavior. In Fig. 2, the time-of-flight spectra of Ne, Ar, Kr, and Xe recoiling from the CsI surface are shown for E_{coll}=20 kcal/mole. The time-of-flight spectra reflect the energy that is left over in the gas atom after the collision event. At E_{coll}=20 kcal/mole, the Ne and Ar atom time-of-flight spectra clearly show two components. For the heavier Kr and Xe atoms, the time-of-flight spectra are broad and the "fast" and "slow"

peaks are blurred together. The light Ne atoms have lost much less energy than the heavier Xe atoms, and in addition since Xe is heavier it moves slower; thus, the time-of-flight peak in Fig. 2a is at much earlier times than in Fig. 2d.

For each species, the "fast" and "slow" features in the time-of-flight spectra are blurred together at low E_{coll} and become distinct at higher E_{coll}. The values of E_{coll} where the peaks become distinct are different for each species. This general trend is illustrated in Fig. 3, where time-of-flight spectra for recoiling Ar atoms are shown for three values of E_{coll}: 10, 19, and 48 kcal/mole. Thus, while in Fig. 2 the Kr and Xe atom spectra are broad, at higher collision energies, these atoms also show "fast" and "slow" features.

The time-of-flight spectra of Kr and Xe atoms for E_{coll}=50 and 65 kcal/mole, respectively, are shown in Fig. 4 at θ_i= 20° and 60°. These spectra clearly show "fast" and "slow" components. By taking the spectra at many angles, θ_i, the two components can be separated. The lines in Fig. 4 are simulated time-of-flight spectra based on the translational energy distributions shown in Figs. 5 and 6 for Kr and Xe, respectively. Simulated time-of-flight spectra are generated using the forward convolution method described in Chapter 2.[5] Simulated spectra are generated for each component and then these are added to get a total fit. In the fitting procedure, the "slow" component of the time-of-flight was assumed to have no variation with θ_i, and only the "fast" component was adjusted to get a good total fit at all angles θ_i. However, it turned out that very little variation in the "fast" component was required. It is reasonable to fix the simulation for the "slow"

component at all θ_i since this peak arises from atoms that have lost most of their incident energy. In Fig. 5a, the translational energy distribution used to generate the simulation of the "fast" Kr atom time-of-flight peak is shown. It is quite broad and extends out to about 34 kcal/mole, which is less than E_{coll}=50 kcal/mole. Thus, no elastic scattering is observed. The "slow" Kr atom time-of-flight peak is simulated using the translational energy distribution in Fig. 5b. For comparison, a Maxwell-Boltzmann distribution for the surface temperature is also shown. Thus, while these Kr atoms have lost quite a bit of energy, they have not become completely thermalized to the surface temperature of 646 K. Figs. 6a and 6b similarly show the translational energy distributions for the "fast" and "slow" Xe atoms recoiling after striking the surface with E_{coll}=65 kcal/mole. In the case of Xe, the "slow" atom distribution deviates even more from a Maxwell-Boltzmann distribution than in the case of Kr.

The percentage of the energy transfer, $\%E_{trans.}$, based on the collision energy and the peak maximum in the translational energy distribution for recoiling atoms is calculated according to:

$$\%E_{trans.} = \frac{E_{coll} - E_{P(E)}}{E_{coll}} . \qquad (5)$$

The results for all the systems studied (taken from spectra measured at θ_i=45°) are shown in Fig. 7. In addition, the $\%E_{trans.}$ calculated from Eqn. (2) for different impulsive collisions is indicated at the right side of the graph. In Fig. 7, the $\%E_{trans.}$

for "fast" and "slow" time-of-flight components is distinguished by the solid and open symbols, respectively.

For the "fast" time-of-flight component, the qualitative variation in $\%E_{trans.}$ with the mass of the incoming gas particle follows the expected trend, however the magnitude of $\%E_{trans.}$ is not what is predicted by using Eqn. (2), except for the case of Ne atoms. In addition, the $\%E_{trans.}$ for the "fast" peak appears to be independent of E_{coll}, which is also a feature of the impulse approximation model.

For the "slow" time-of-flight component the energy transfer is roughly constant with varying E_{coll}, and the magnitude of $\%E_{trans.}$ for Kr and Xe atom scattering is about the same as that predicted using Egn. (2). However, for the case of Ne and Ar, the $\%E_{trans.}$ is much greater than that predicted by the impulse approximation in Eqn. (2).

Discussion

The hyperthermal scattering results reflect the dynamics of the gas-surface interaction at the repulsive wall of the potential energy surface. The energy transfer is mechanical in nature since no chemical reactions are taking place. It is important to investigate the purely mechanical energy transfer in order to better understand reactive collisions, whose dynamics reflect both mechanical and chemical effects. The applicability of binary collision models can be well tested with rare gases scattering from CsI because the whole range of rare gases can be used while maintaining the $\mu<1$ condition (see Eqn. 1).[6] In Chapter 2, the

expression for energy transfer in the impulsive limit for a gas-surface collision was derived by starting from the gas phase version and fixing one mass of the diatomic molecule to be ∞. However, Eqn. (2) can also be derived from a model where the incoming particle scatters from a linear chain.[7] The model is one-dimensional and gives the energy transfer for a linear binary collision; the energy transfer, given by Eqn. (2) is also known as the 'Baule' formula.[8] The impulse limit is valid when the collision is fast and the gas atom leaves the collision zone before the lattice can respond. Thus, impulsive collisions are expected above a certain threshold of E_{coll}, where classical mechanics describes the interaction well and the atom can leave faster than the lattice can respond. However, as E_{coll} increases, the gas atom can also more easily penetrate or deform the lattice, suffering multiple collisions during its outbound motion. Trying to distinguish between these two processes is not always straightforward when looking at the energy transfer, $\%E_{trans.}$, resulting from the gas-surface interaction.

There are some factors that reduce the energy transfer given by Eqn. (2).[7] First of all, the energy transfer will be reduced by increased surface temperature by an amount on the order of k_BT_s. Including a "thermal average" for the initial motion of the surface atom at a surface temperature, T_s, results in a modified expression for the energy transfer:

$$\Delta E(T_s) = \frac{4\mu}{(1+\mu)^2}(E_i - k_B T_s) \qquad (6)$$

However, for T_s~650 K in these experiments, $k_B T_s$~1.3 kcal/mole, which is insignificant compared to E_i. Another factor that reduces the energy transfer from the predictions of Eqn. (2) is averaging over impact parameter to account for a three-dimensional picture (the model was strictly one-dimensional). Thus, the reduction in energy transfer for Ar, Kr, and Xe atoms (from the "fast" time-of-flight peak) compared with the predictions from Eqn. (2) is not surprising. These collisions may indeed be impulsive since the energy transfer exhibits the mass trend and independence of E_{coll} predicted by the model.

For the "fast" time-of-flight peak, the energy transfer can also reflect scattering from a higher effective mass, M_{eff}, at the surface.[2, 9] M_{eff} replaces M_s in Eqn. (1). The following M_{eff} values can be calculated for Ar, Kr, and Xe atom scattering, respectively: 235, 275, and 364. These numbers reflect the extent of coupling between surface atoms in the collision, but do not tell exactly how many Cs or I atoms are involved. They can only give a relative picture where Xe scatters from a larger coupled set of atoms than Kr or Ar. The "fast" peak from Ne atom scattering gives a $\%E_{trans.}$ close to that predicted by Eqn. (2).

The "slow" time-of-flight peak results from very efficient energy transfer, but may result from multiple collisions, depending on the particular system (see Fig. 7). For Kr and Xe atom scattering, large values of $\%E_{trans.}$ are expected for impulsive collisions, but for Ar and Ne atom scattering, the $\%E_{trans.}$ is much greater than that predicted by Eqn. (2). The "slow" time-of-flight peak for Kr and Xe

atoms recoiling from the surface was fit with a translational energy distribution "hotter" than a Maxwell-Boltzmann distribution for the surface temperature, T_s (Figs. 5 and 6). For Kr and Xe atoms, with M_g so close to M_s, very efficient energy transfer is expected and so only a few collisions would be needed for complete thermal accomodation. The atoms would then emerge with a Maxwell-Boltzmann distribution. Since this is clearly not the case, single collision energy transfer may indeed be taking place for Kr and Xe atoms. Thus, for Kr and Xe atoms, the "slow" and "fast" time-of-flight peaks may both arise from single collisions, but the nature of the collision partner at the surface may be different. In the case of the "fast" time-of-flight peak, the scattering may be from a coupled set of atoms while in the case of the "slow" time-of-flight peak, a head on collision with a single Cs or I may be taking place. Unlike the cases of LiF or NaCl, in CsI head-on collisions with either the Cs^+ or I^- ions are possible since the cations do not eclipse the anions to the same extent (r_{Cs+}= 1.455 Å and r_{I-}= 1.785 Å).[10]

For Ne and Ar atom scattering, the energy loss observed as the "slow" time-of-flight peak is likely due to multiple collisions. By successive calculations with Eqn. (2), the energy loss from sequential collisions can be calculated. For successive Ne-Cs or Ne-I collisions, the energy loss observed in Fig. 7 can result from 4-6 collisions. For the case of Ar, the energy loss corresponds to about 2-3 collisions. This kind of energy loss may be the result of the gas atom deforming or penetrating the lattice and then sufferring multiple collisions along its exit trajectory.

Conclusions

The hyperthermal scattering of Ne, Ar, Kr, and Xe was investigated to further explore the mass dependence of the gas atom on the efficiency of energy transfer in gas-surface collisions. By measuring the time-of-flight of the recoiling atom as it emerges from the collision zone, the dynamics of the energy loss processes taking place can be examined in detail. For Ne atoms in the range of E_{coll}= 13-63 kcal/mole and Ar atoms in the range of E_{coll}= 10-58 kcal/mole, one mechanism of energy loss due to multiple collisions and another likely resulting from single collisions were observed. For Kr and Xe atoms in the ranges of E_{coll}=13-73 kcal/mole and 16-95 kcal/mole, respectively, two energy loss mechanisms were observed, which may be due to different types of single collision events at the surface.

References and Notes

1. R. W. Zwanzig, J. Chem. Phys. **32**, 1173 (1960).
2. H. F. Winters, H. Coufal, C. T. Rettner, and D. S. Bethune, Phys. Rev. B **41**, 6240 (1990).
3. H. Haberland, U. Buck, and M. Tolle, Rev. Sci. Instrum. **56**, 1714 (1985).
4. The melting point of CsI is 899 K; R. C. Weast, CRC Handbook of Chemistry and Physics (CRC Press, Boca Raton, Florida, 1989).
5. A. M. Wodtke, Ph. D. Thesis, University of California, Berkeley, 1986; X. Zhao, Ph. D. Thesis, University of California, Berkeley, 1988; J. D. Myers, Ph. D. Thesis, University of California, Berkeley, 1993.
6. When $\mu>1$, the gas atom is not stopped by the collision and thus penetrates the lattice, suffering multiple collisions. This violates the definition of impulsive scattering since the lattice responds on the time scale of the collision in this case.
7. J. Harris, Dynamics of Gas-Surface Interactions (The Royal Society of Chemistry, London, 1991).
8. F. O. Goodman and H. Y. Wachman, Dynamics of Gas-Surface Scattering (Academic Press, New York, 1976).
9. G. Carter and J. S. Colligon, Ion Bombardment of Solids (Elsevier, New York, 1968).

10. J. S. Blakemore, Solid State Physics, 2nd Ed. (Cambridge University Press, Cambridge, 1985) p.17.

Figure Captions

Fig. 3-1 Characterization of seeded beams using the high temperature rhenium nozzle. Nozzle temperature calibrated with a neat Ne beam (open squares). E_{beam} determined for 0.6% Ne/H_2 (open diamonds), 4% Ar/He (solid squares), 5% Kr/He (solid triangles), and 5% Xe/He (open circles).

Fig. 3-2 Time-of-flight spectra of (a) Ne, (b) Ar, (c) Kr, and (d) Xe that had E_{coll}=20 kcal/mole initially (all taken at θ_i=45°). The time-of-flight spectra reflect the amount of kinetic energy left over in the gaseous atom after collision with the surface.

Fig. 3-3 Time-of-flight spectra for Ar atoms with different incident energies recoiling from CsI (measured at θ_i=45°). In (a) E_{coll}=10 kcal/mole, in (b) E_{coll}=19 kcal/mole, and in (c) E_{coll}=48 kcal/mole. The two features in the time-of-flight spectra become clearly separated as E_{coll} is increased for all the rare gaseous atoms studied.

Fig. 3-4 Time-of-flight spectra for: Kr atoms with E_{coll}= 50 kcal/mole taken at (a) θ_i=20° and (b) θ_i=60° and Xe atoms with E_{coll}=65 kcal/mole taken at (c) θ_i=20° and (d) θ_i=60°. The fits are generated from the translational energy distributions in Figs. 5 and 6 for Kr and Xe, respectively. The

"fast" time-of-flight peak is simulated using the distribution in Fig. 5a (Kr) or Fig. 6a (Xe) (dotted line), and the "slow" time-of-flight peak is simulated using the distribution in Fig. 5b (Kr) or Fig. 6b (Xe) (dashed line). The total fit (solid line) is the sum of the "fast" and "slow" contributions.

Fig. 3-5 Translational energy distributions used to fit the Kr atom scattering data in Figs. 4a and 4b: (a) for the fit of the "fast" time-of-flight peak and (b) for the fit of the "slow" time of flight peak (dashed line). A Maxwell-Boltzmann distribution for T_{surf}=646 K is also shown (solid line) in (b).

Fig. 3-6 Translational energy distributions used to fit the Xe atom scattering data in Figs. 4c and 4d: (a) for the fit of the "fast" time-of-flight peak and (b) for the fit of the "slow" time of flight peak (dashed line). A Maxwell-Boltzmann distribution for T_{surf}=648 K is also shown (solid line) in (b).

Fig. 3-7 Summary of $\%E_{trans.}$ for all the systems studied over the entire range of E_{coll} used in the experiments. Solid symbols represent the $\%E_{trans.}$ from "fast" time-of-flight peaks and open symbols represent the $\%E_{trans.}$ from "slow" time-of-flight components as follows: Ne (squares), Ar (upright triangles), Kr (diamonds), and Xe (hexagons). The $\%E_{trans.}$ predicted using Eqn. (2) for different impulsive collisions is shown at right (open circles).

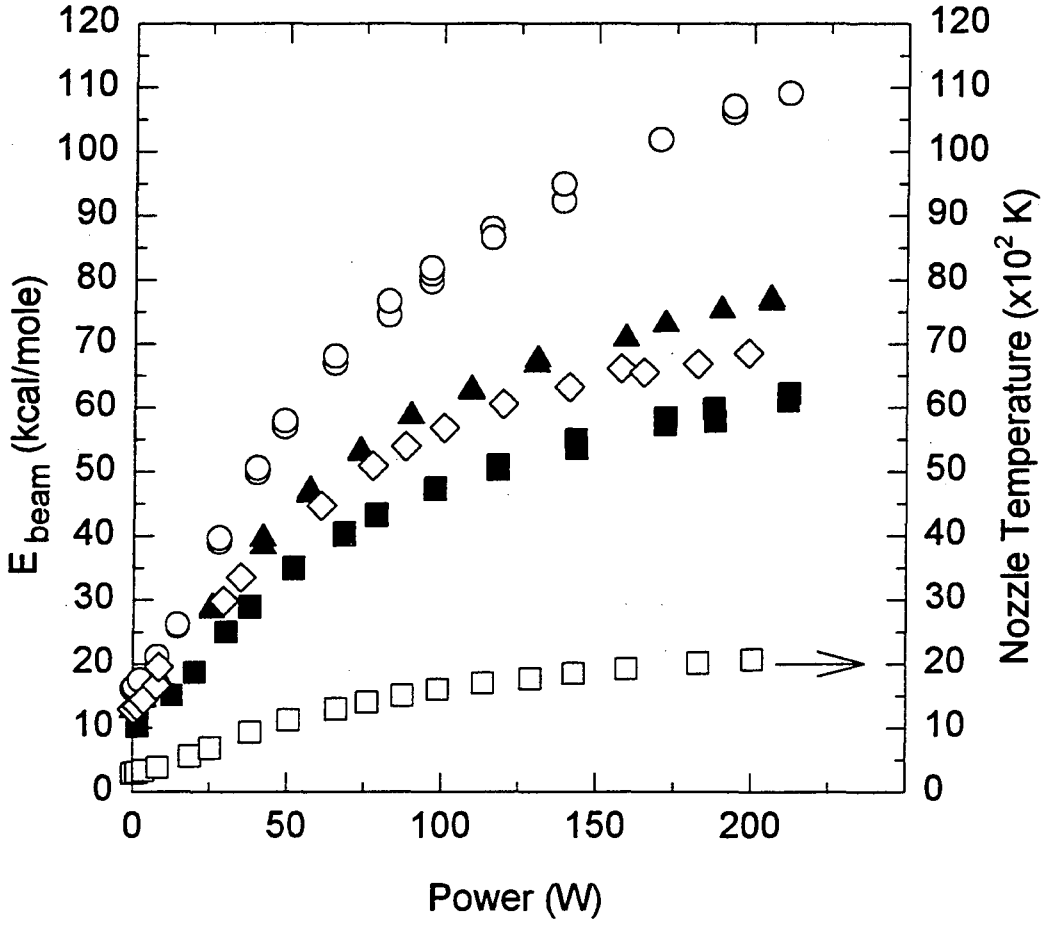
120
110
100
90
80
70
60
50
40
30
20
10
0
0
50
100
150
200
Power (W)
E beam (kcal/mole)
Nozzle Temperature (x10² K)

Figure 3-1

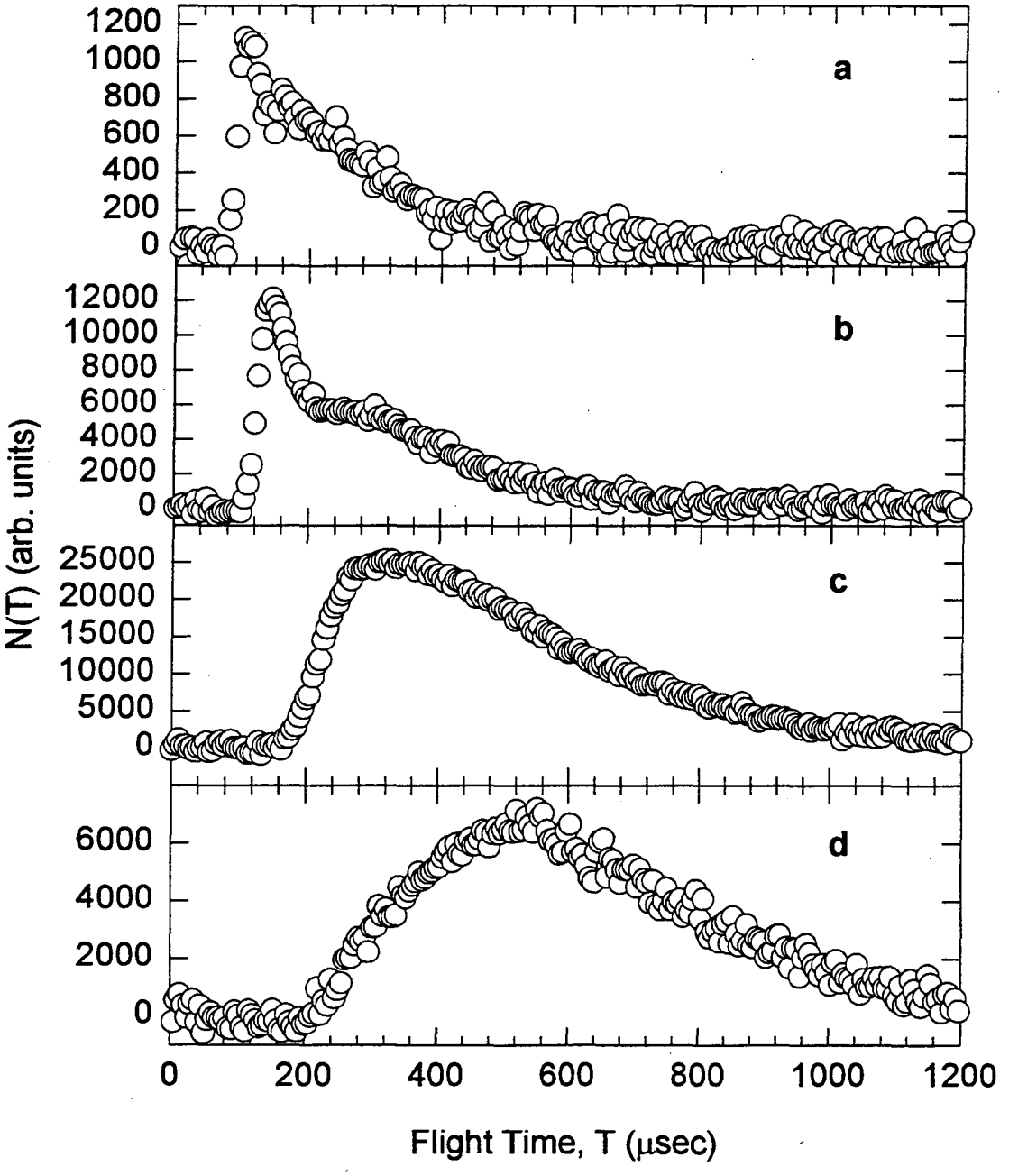
a
b
c
d
N(T) (arb. units)
Flight Time, T (μsec)
0
200
400
600
800
1000
1200
2000
4000
6000
8000
10000
12000
5000
15000
20000
25000

Figure 3-2

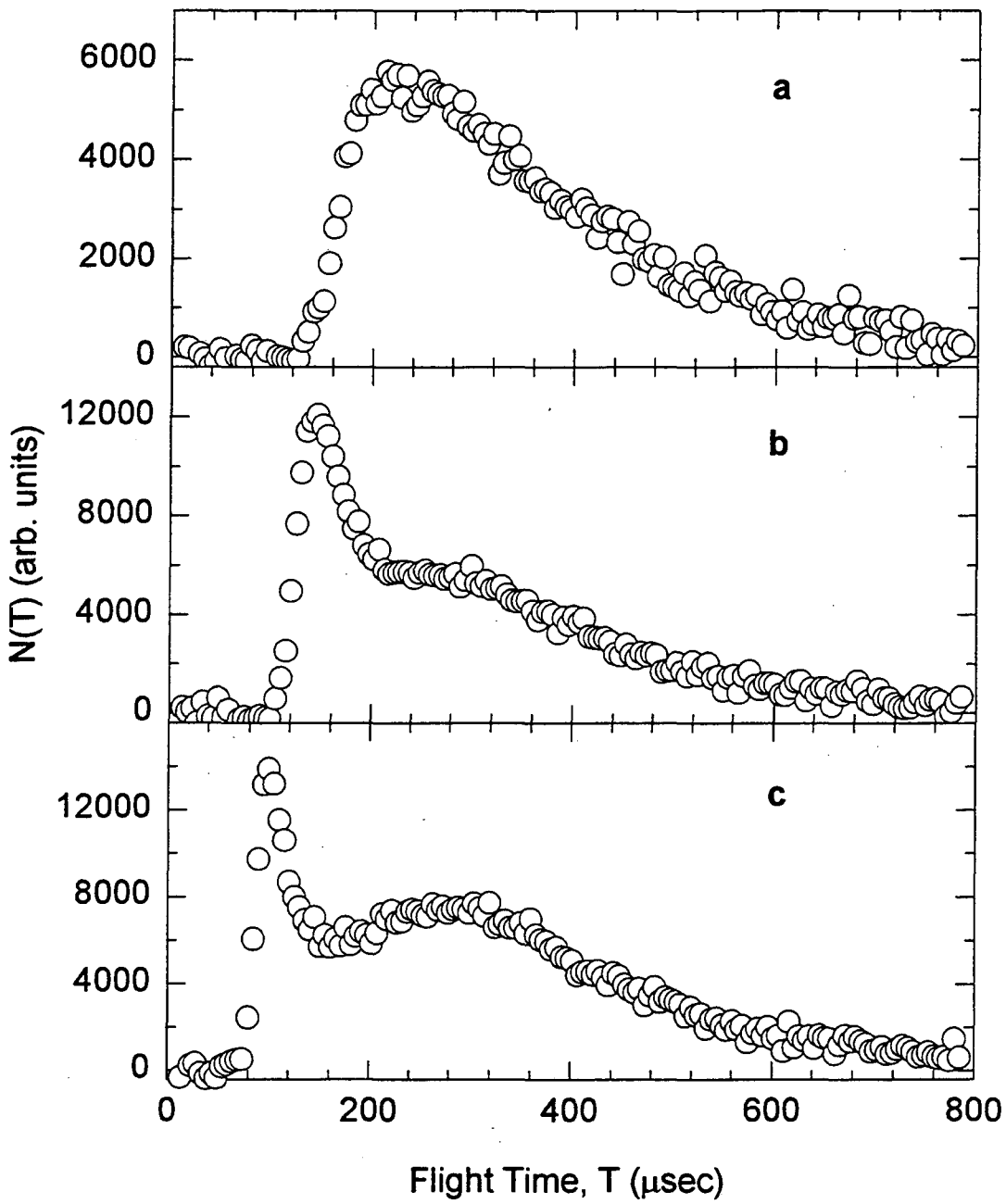
6000
4000
2000
0
a
12000
8000
4000
0
b
12000
8000
4000
0
c
N(T) (arb. units)
0
200
400
600
800
Flight Time, T (μsec)

Figure 3-3

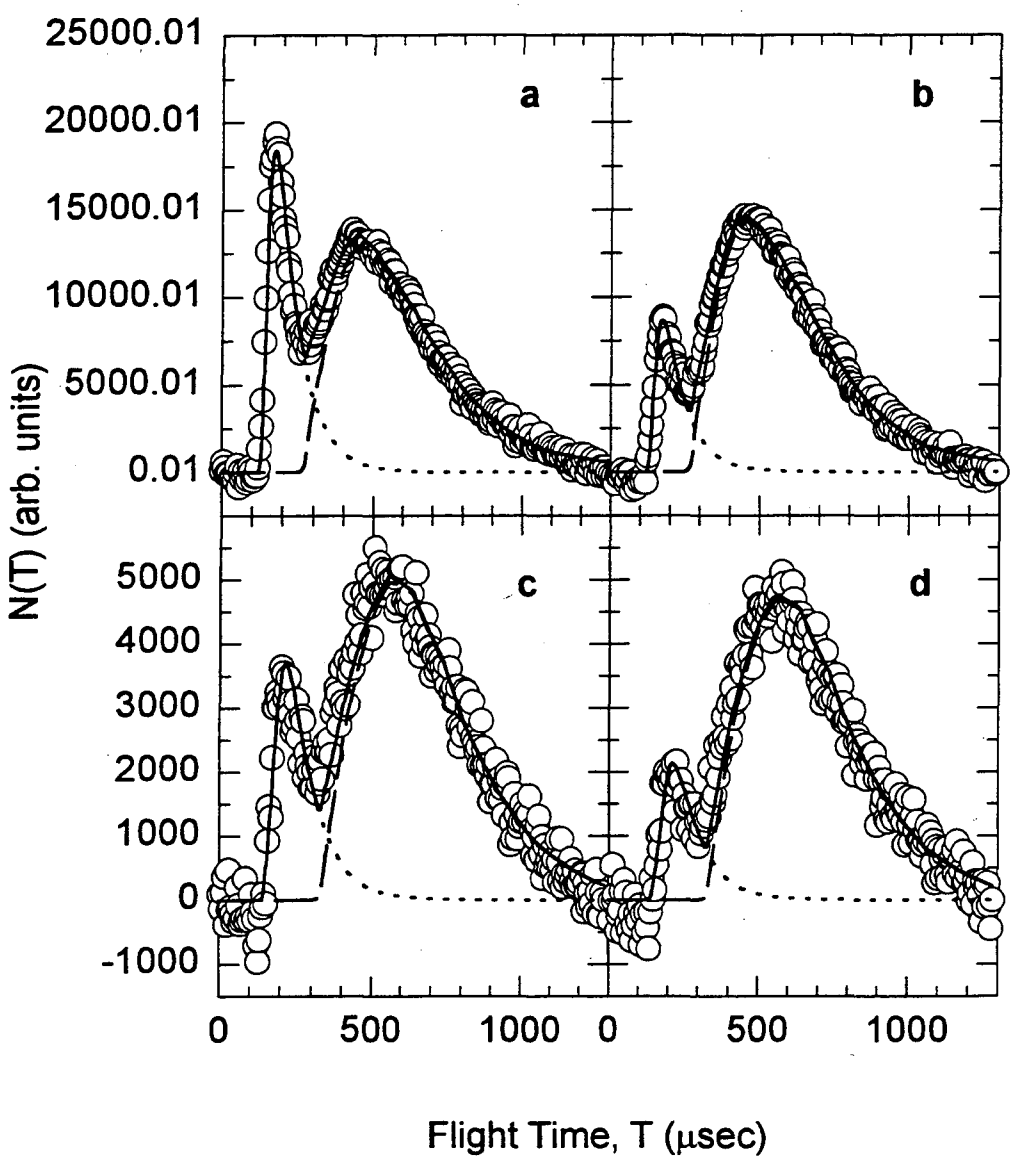
25000.01
20000.01
15000.01
10000.01
5000.01
0.01
5000
4000
3000
2000
1000
0
-1000
N(T) (arb. units)
a
b
c
d
0
500
1000
0
500
1000
Flight Time, T (μsec)

Figure 3-4

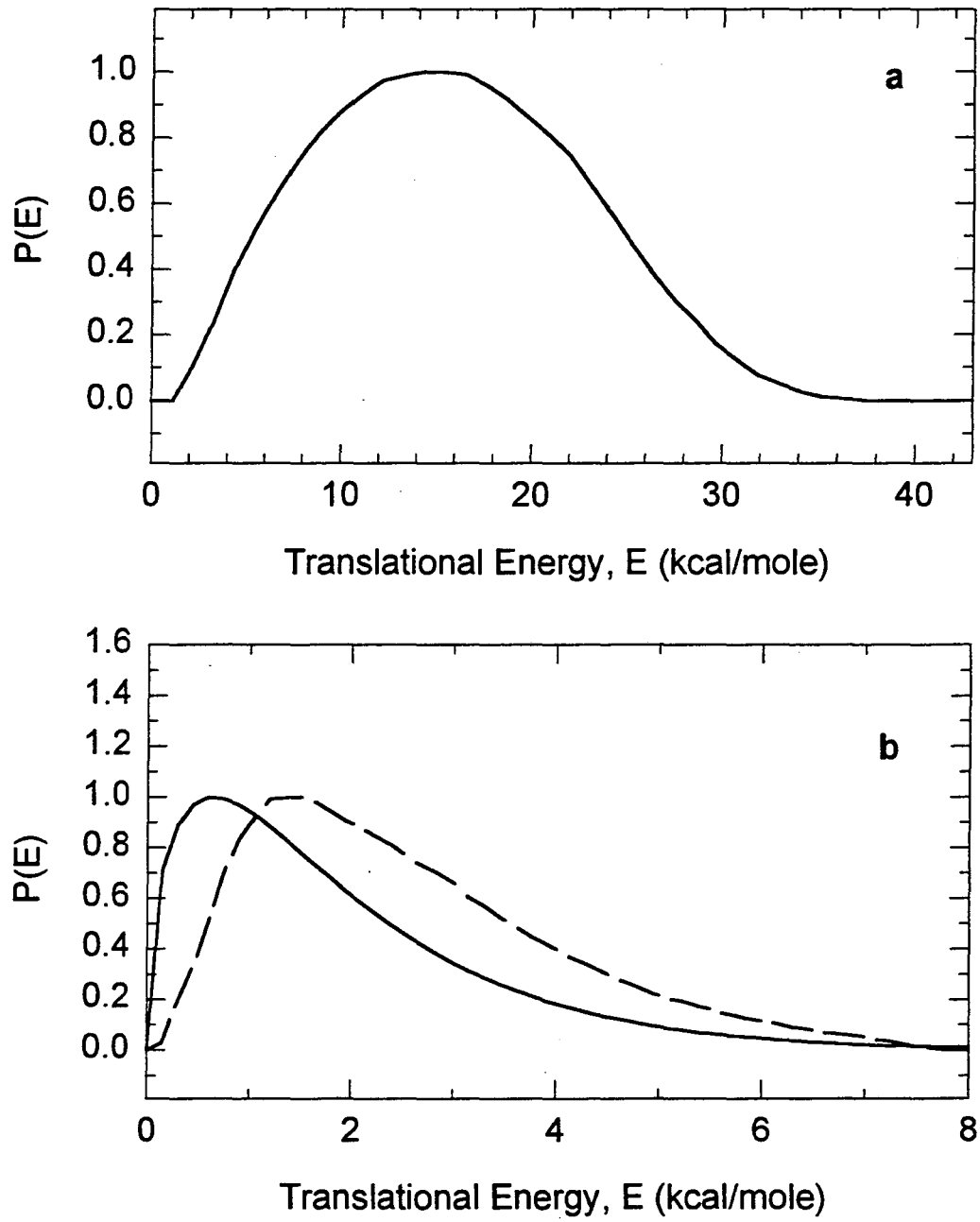
a
P(E)
1.0
0.8
0.6
0.4
0.2
0.0
0
10
20
30
40
Translational Energy, E (kcal/mole)
b
P(E)
1.6
1.4
1.2
1.0
0.8
0.6
0.4
0.2
0.0
0
2
4
6
8
Translational Energy, E (kcal/mole)

Figure 3-5

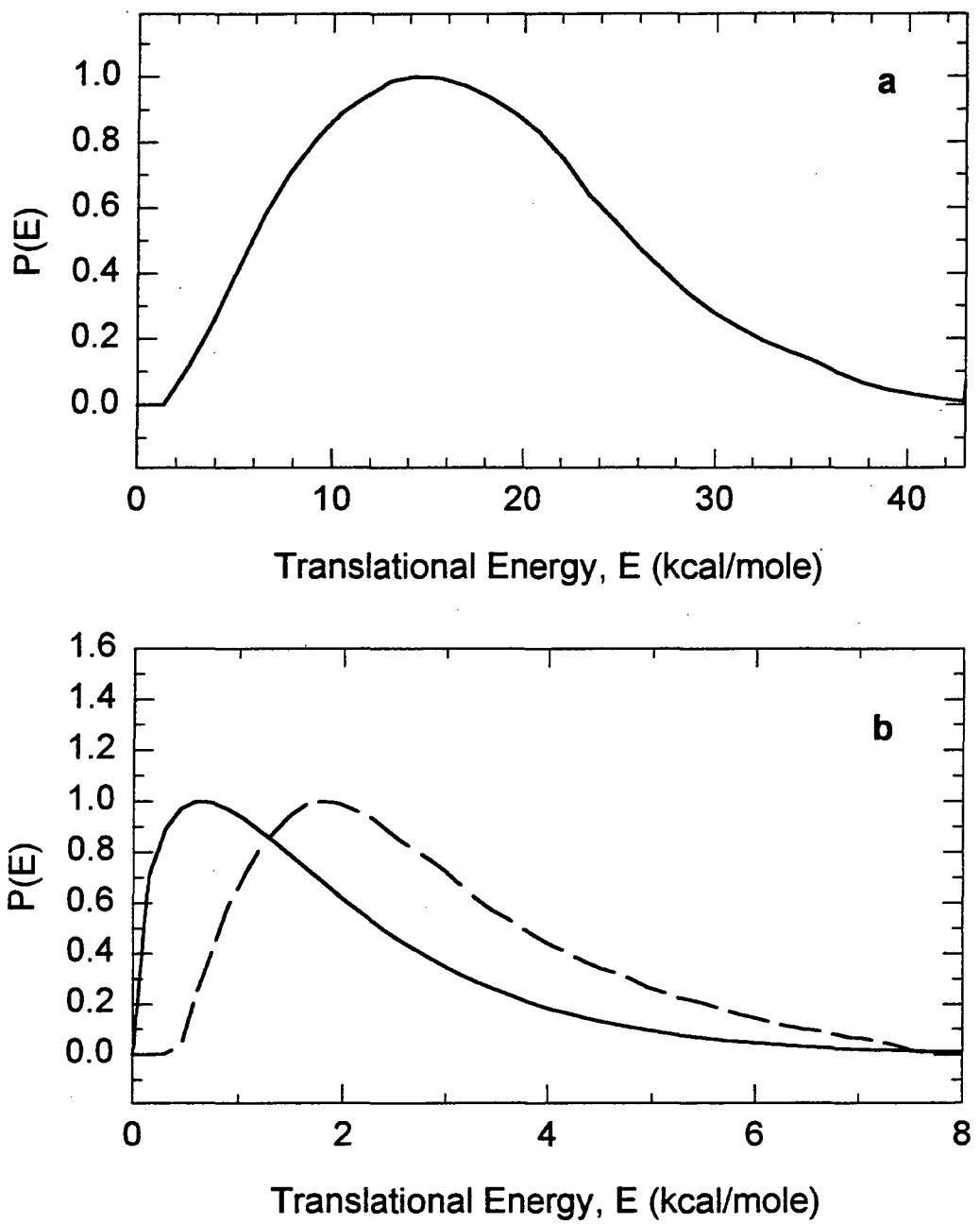
a
P(E)
1.0
0.8
0.6
0.4
0.2
0.0
0
10
20
30
40
Translational Energy, E (kcal/mole)
b
P(E)
1.6
1.4
1.2
1.0
0.8
0.6
0.4
0.2
0.0
0
2
4
6
8
Translational Energy, E (kcal/mole)

Figure 3-6

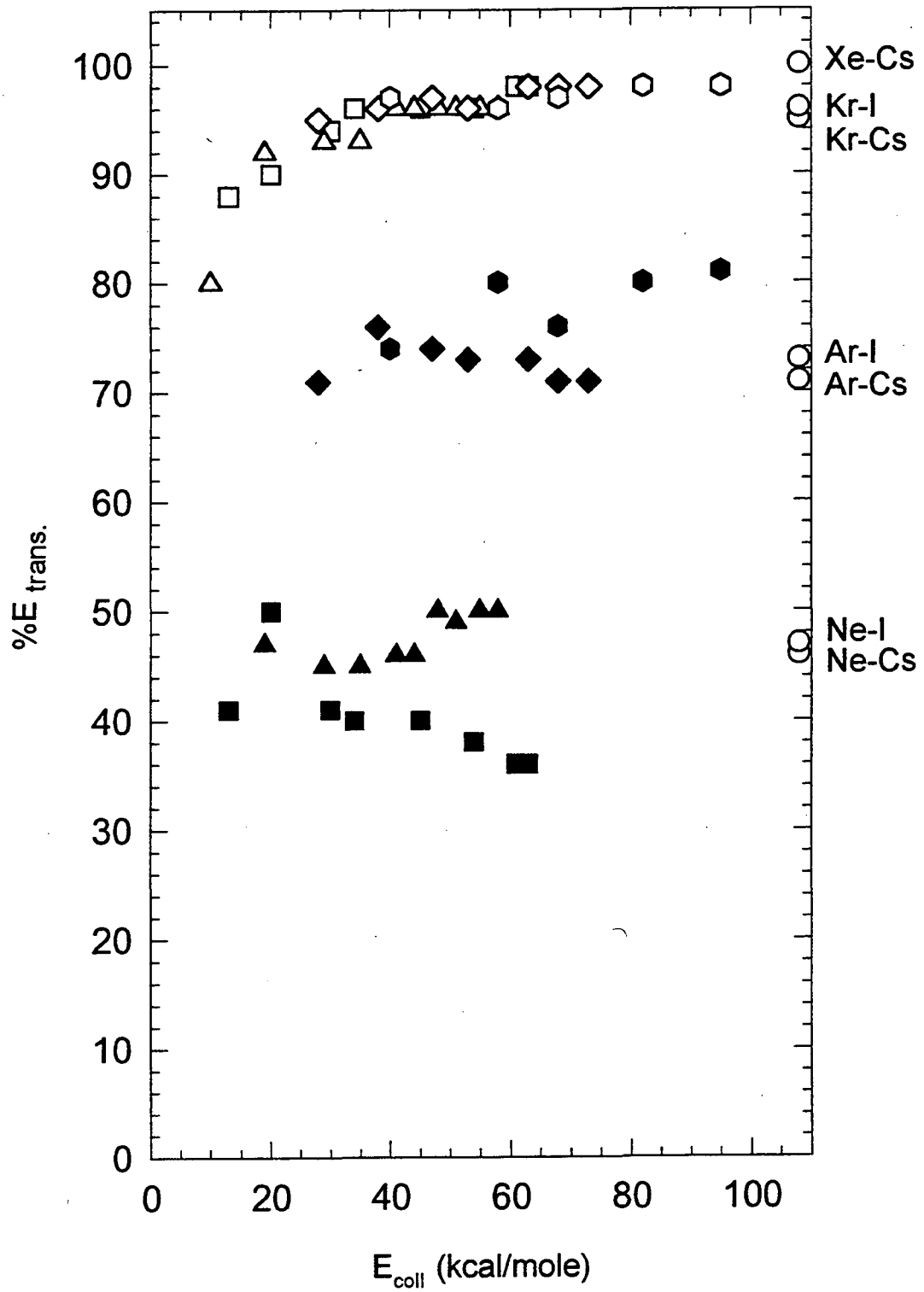
100
90
80
70
60
50
40
30
20
10
0
%E trans.
0
20
40
60
80
100
E coll (kcal/mole)
Xe-Cs
Kr-I
Kr-Cs
Ar-I
Ar-Cs
Ne-I
Ne-Cs

Figure 3–7

Chapter 4

Atomic Beam-Surface Scattering Study of HF (DF) Produced in the Reaction: H(D) + LiF(001)

Introduction

Reactions at the gas-surface interface have been successfully probed using molecular beam techniques by many research groups. Modulated beams have been used to study the kinetics of gas-surface reactions by measuring the rates of formation of various product species as they evolve from the surface.[1-3] The dynamics of the gas-surface reaction can also be studied using molecular beam techniques. Pure adsorption and desorption events, which model important steps in the overall reaction process, have been more extensively studied than reaction product dynamics.[4] The final step in a gas-surface reaction, where either a bond is formed and/or the new product molecule desorbs from the surface, can be studied by looking at the product translational and/or internal energy as it emerges from the surface.[5] For example, the work on D_2O formation in the oxidation of deuterium on Pt(111) by Ceyer et. al.[6] shows how the D_2O product angular and translational energy distributions lead to an understanding of the reaction mechanism. The internal states of product CO_2 from CO oxidation on Pt have also been measured, showing how different modes, each characterized by its own Boltzmann

temperature, behave as a function of surface temperature.[7]

In this work, the velocity distributions of individually mass-selected products are measured as they desorb from the surface for different angles between the source, a supersonic atomic beam of H or D atoms, and the plane of the surface, LiF(001), with the detector fixed. In addition to identification of reaction products, analysis of this type of data reveals the dynamical nature of the gas-surface reaction.

Crystalline LiF is usually considered to be a relatively inert material. However, the gas phase reaction H + LiF ---> HF + Li is nearly thermoneutral.[8] In the solid phase, the LiF lattice commonly contains anion vacancies that can sometimes be filled by H-atoms without too much distortion of the total lattice electron density.[9] In addition, calculations show that as an H-atom approaches certain types of anion vacancies, a bound state is formed, whereas for H_2 the interaction is repulsive.[10] The interesting dynamics of the H-atom LiF(001) surface interaction explored here show that LiF(001) is not inert to H-atoms, and indeed the reaction product HF (and the DF analogue) is directly measured by time-of-flight methods.

Experimental

A continuous supersonic beam of H (or D) atoms was directed towards a freshly cleaved LiF(001) surface in the gas-surface scattering apparatus described earlier.[11] The particles scattered from the surface are chopped by a cross-

correlation wheel, mass selected, and counted by a channeltron after travelling through a flight distance of 23.9cm.[12] Time-of-flight spectra of individual mass-selected species are thus measured, which allows for determination of the translational energy imparted to individual products of a gas-surface chemical reaction. In this experiment, the isotopes of Ne at m/e= 20 and 22 were used to calibrate the mass spectrometer. Also, by using high resolution, m/e= 19, 20, and 21 could be clearly distinguished.

The H and D atoms are produced in a supersonic expansion by thermal pyrolysis of neat H_2 or D_2, using a high temperature nozzle made of pure rhenium metal (Sandvik Rhenium). The nozzle is made of two concentric rhenium tubes that are connected by a rhenium cap, which has been welded to one end under inert atmosphere. A 0.007" nozzle hole was drilled in the center of the cap by EDM (EDM Exotics). The inner tube is welded to 1/4" stainless steel tubing, which forms the gas line. Two water-cooled copper clamps, one attached to the inner rhenium tube and one to the outer tube, carry the current and secure the nozzle to a translational stage. The translational stage allows for thermal expansion of the rhenium tubes as they are heated without straining the welds at the cap. The current is thus forced to pass through the welded cap where it can heat the metal to about 2500 K (using up to 250 W). The nozzle temperature has been measured using optical pyrometry and by measuring the beam time-of-flight for a neat Ne beam. The temperatures from the two measurements agree well (Fig. 1). The nozzle was operated at 2140 K to produce H and D atoms but minimize the

possibility of evaporating rhenium metal, which becomes a problem above 2500 K. The use of rhenium instead of tungsten, which has been used previously,[13] was motivated by a desire to find a material that does not become brittle and therefore susceptible to cracking after thermal cycling to high temperatures. The flux of H-atoms is determined to be 5 x 10^{18} atoms cm^{-2} s^{-1} based on a 3% dissociation rate of H_2 under the beam conditions used.

The LiF samples were cleaved from a single-crystal boule in air along the natural (001) cleavage plane. Freshly cleaved samples were heated in vacuum (1 x 10^{-7} Torr) for 24 hrs. at about 750 K to remove water and anneal the crystal. Experiments were typically run between 650-700 K to minimize adsorption of impurities. A narrow velocity distribution in the scattering pattern from H_2 is a good check of the cleanliness of the surface, and so such time-of-flight measurements were performed before looking for reaction products. The beam was brought to high temperature over the course of 2 hrs. and allowed to stabilize, with the crystal out of the beam path. Once the beam was stable, a typical time-of-flight spectrum of product HF or DF took about an hour or two to collect, depending on the angle between the beam and the surface plane. The angle θ_i, between the beam and the surface, and ϕ_i, the angle of the beam with respect to the [100] surface direction, can both be varied independently. No ϕ_i dependence was observed, though, in the case of HF or DF product evolution, so the spectra in the figures here are all at ϕ_i= 0°. The angle θ_i is defined to be 0° when the angle between the beam and the surface plane is 0° (it is the complement of the angle

between the beam and the surface normal); the detector is fixed at 90° from the beam.

Results

HF(m/e= 20) and DF(m/e= 21) product time-of-flight spectra were measured in separate experiments for different angles, θ_i, between the source and the plane of the LiF(001) surface. The product DF has the advantage that m/e= 21 has very low background in the mass spectrometer. In addition to monitoring the appropriate product mass, spectra were also taken at m/e= 19, corresponding to fluorine, and also m/e= 1 or 2 resulting from reflected H and H_2 or D and D_2, respectively. The product m/e= 20 or 21 signal was only seen when the nozzle was hot enough to produce atomic H or D, and considerable effort was made to keep the experimental conditions the same between HF and DF experiments so that they could be compared. At a nozzle temperature of 2140 K, the maximum H or D atom beam energy is calculated to be ~7.5 kcal/mole.[14]

Typical time-of-flight spectra at m/e= 20 for H + LiF(001) and at m/e= 21 for D + LiF(001) are shown for θ_i= 30° along with the time-of-flight for the reflected beam in each case in Fig. 2. The m/e= 20 and 21 time-of-flight spectra show a sharp fast peak and a slower peak. The time-of-flight for the reflected beam in each case has been scaled and shifted to have the same leading edge as the m/e= 20 or 21 data to clearly show that the peak from the beam is narrower. The origin of the fast peak will be addressed in the discussion of the results, but at this

point suffice it to say that the slow peak is the only real product signal.

At all angles θ_i, the HF or DF product time-of-flight is the same as that of m/e= 19, corresponding to F. The matching time-of-flights indicate that F results from cracking of HF or DF in the ionizer rather than by other mechanisms, such as desorption of F or LiF from the surface. Such a desorption mechanism should give rise to a Maxwell-Boltzmann distribution at the surface temperature, which would extend out to longer times in the time-of-flight spectrum. No evidence for this type of mechanism was observed.

Fig. 3 and Fig. 4 show the time-of-flight spectra obtained at m/e= 20 and m/e= 21, respectively, for different values of θ_i. Also included in the figures are simulated time-of-flight spectra for the slow peak, corresponding to the translational energy distribution in Fig. 5. Each frame has been scaled to show the details of the individual spectra; the change in product yield with θ_i is shown separately in Fig. 6. The simulated spectra are obtained by the forward convolution method[15] and include the various apparatus functions that affect a time-of-flight spectrum. In this case, since the fast peak in the product time-of-flight spectra could not simply be removed by subtracting the corresponding reflected beam time-of-flight (due to the different peak widths, see discussion), simulations of the slow peak were done by generating a consistent translational energy distribution at all angles θ_i. For both products, HF and DF, one translational energy distribution that fits the slow time-of-flight peak was found (Fig. 5) with $\langle E \rangle_T$= 4.3 kcal/mole and E_{max}= 13 kcal/mole. In the region of the peak maximum, the uncertainty is 0.2 kcal/mole,

but at E_{max} (tail of the distribution) the uncertainty is as high as 1.3 kcal/mole. The cross-correlation wheel is limited to 5 μsec time resolution, and the energy goes as $E \propto (1/t)^2$, giving rise to greater uncertainties at higher energies.

A θ_i distribution is calculated by integrating under the curve for the simulated time-of-flight peak in each spectrum. The HF and DF θ_i distributions look similar (Fig. 6), peaking near θ_i= 45-50°. Although these distributions are not full flux angular distributions, given the geometry of the machine, they do indicate that the scattering lobe for the product HF or DF lies near the specular angle.

Discussion

Atomic Reactant Species

The fact that HF or DF product is not seen until the beam source nozzle is hot enough to dissociate a significant fraction of H_2 or D_2 strongly suggests that the atomic species is indeed the reactant in the systems discussed here. Calculations done by Matsumura support this conclusion.[16] The calculations show that for H_2 approaching anion vacancies in the LiF lattice at either an edge, corner, or surface vacancy, the interaction is highly repulsive. For atomic H, however, there is an attractive interaction, especially when an electron is trapped in the vacancy. H_2 approaching a site on the LiF(001) surface with no vacancy would also not be expected to molecularly adsorb and take part in a reaction. In addition, dissociative chemisorption of H_2 is not possible because the dissociative adsorption energy of 1 eV is smaller than the 2.3 eV necessary to break the H-H bond. Therefore, the

atomic species produced in the beam must be the reactant.

Origin of the Fast Time-of-Flight Peak

In the time-of-flight spectra of Fig. 3 and Fig. 4, there are clearly two peaks. The fast peak is largest at θ_i= 45° (not shown), where it completely hides the features of the second, slow peak. As θ_i is moved towards a grazing angle of 10° or near the surface normal at 80°, the fast peak drops to a minimum and the second, slow peak becomes the dominant feature. The fast peak, when converted to a translational energy distribution, extends out to energies as high as 40 kcal/mole for the case of HF. HF coming off the surface with 40 kcal/mole of translational energy is not physically reasonable, and so other sources of the fast time-of-flight peak must be considered.

In the source, H or D atoms are produced, which can be excited in the electron bombardment ionizer to Rydberg states. In fact, even H_2 can be a source of excited states of atomic hydrogen in the electron bombardment ionizer.[17] Such Rydberg H or D atoms are energetic neutrals, travelling with the velocity of the beam. As neutrals, they cannot be filtered by the quadrupole, but they can be detected by the channeltron; thus, they show up in spectra taken at m/e= 20 or 21. In fact, if the fast time-of-flight peak is due solely to Rydberg atoms, it should appear at any mass setting on the quadrupole, and so by tuning to masses not normally expected to produce signal, this hypothesis can be tested. Upon tuning to other m/e settings of the quadrupole, however, the fast peak did not always appear.

In fact, it only appeared at masses where there was significant background in the mass spectrometer or where the reaction product HF or DF appeared. Thus, Rydberg H or D atoms alone cannot fully explain the presence of the fast time-of-flight peak.

The fact that the fast time-of-flight peak is observed at masses where background appears offers a clue. H^+, metastable H_2,[18] and Rydberg H-atoms (all produced by electron impact) can ionize background gases through collisions just after the ionization region in the detector (and before the quadrupole mass filter). There is a constant source of background because a continuous beam and a cross-correlation chopper wheel are used in the experiment. Two processes can occur to give rise to signal at background masses. First of all, H^+ formed in the ionizer can undergo charge exchange collisions that ionize background gas molecules.[19] Secondly, through processes such as Penning ionization and associative ionization, the background molecules can be ionized by Rydberg H (D) atoms or metastable H_2 (D_2) and therefore mass-selected by the quadrupole.[20] They appear in the time-of-flight spectrum at the characteristic time of the excited H, D, H_2, or D_2, which is very fast. In comparing the reflected beam time-of-flight with the fast peak due to collisional ionization (Fig. 2) the collisional ionization peak is broader, but it is reasonable that the collisional process would give rise to broadening since the background molecules are moving at random velocities and the collisions occur with a wide range of impact parameters. All of the above mechanisms may be operating simultaneously, but the density of H_2 (D_2) is much greater than H (D),

and so charge exchange from the molecular species is probably contributing more to the fast time-of-flight peak than atomic species involved in Penning and associative ionization processes.

In comparing the collisional ionization effect from different spectra, it is interesting to note the intensity dependence of the fast time-of-flight peak on the mass-selected species and the angle θ_i, which determines how much of the incident beam is directly reflected into the detector. In comparing spectra for different mass-selected species, the highest intensity is seen for m/e= 28, which is usually the highest background mass peak in any vacuum system and normally attributed to CO. For θ_i= 45°, the ratio of the fast peak for the m/e= 28 spectra to that of the m/e= 21 (product DF) spectra is 5:1. The intensity of the fast peak seen in spectra taken at m/e= 18 is only 4% of the m/e= 28 peak, which is consistent with a low background due to residual H_2O in the vacuum. In the m/e= 21 spectra, there is a strong dependence of the collisional ionization peak intensity on the angle θ_i. The intensity of the collisional ionization peak drops by a factor of 4 when changing from θ_i= 30° to θ_i= 20°, but the intensity of the slow peak due to the products remains the same. The angular dependence shows that the fast time-of-flight peak has a strong dependence on the incident beam, as expected for the collisional ionization mechanism.

The arguments above rule out the possibility of the fast peak arising from reaction products formed at the surface, which is the main interest in this experiment. Attention is thus focused on the slower peak, which is why a fit for

only the second peaks and the corresponding translational energy distribution is displayed in Figs. 3-5.

Dynamics of HF and DF Products

The HF and DF reaction products, measured directly as they evolve from the surface, appear as the slower peaks in the time-of-flight spectra of Fig. 3 and Fig. 4, respectively. The translational energy distribution in Fig. 5 is derived by fitting the slow peak for both products at each angle θ_i. The difficulty in this method is finding the true leading edge of the slow peak, which corresponds to the high energy limit of the translational energy distribution. However, at θ_i= 10°, the leading edge is distinguishable since the signal between the first and second peaks drops to the baseline. The same translational energy distribution is used to fit the data from both reactions at all angles θ_i.

The translational energy distribution for HF and DF is not a Maxwell-Boltzmann distribution at the surface temperature. Fig. 7 compares the product translational energy distribution from Fig. 5 with a Maxwell-Boltzmann distribution at the surface temperature, T_{surf}= 690 K. The product distribution peaks at higher energy than a Maxwell-Boltzmann distribution, about 2.5 kcal/mole, with a substantial fraction of the molecules having up to 13 kcal/mole of translational energy. The translational energy distribution peaking far from the Maxwell-Boltzmann distribution peak indicates that there is a barrier in the exit channel.

Although it is possible to fit the HF and DF products separately so that they

each have their own translational energy distribution, such a distinction between the products is not strongly supported by the data. The difference in the energy distributions is too small to be justified given the signal/noise ratio and the added complication of the collisional ionization peak near the leading edge of the product time-of-flight peak. However, it is interesting to note that when two distributions are used, best fit to all the θ_i for a particular product, the DF appears to have less energy left over in translation than the HF upon separating from the LiF(001) surface (although the two distributions have the same E_{max}). This suggests that DF has more energy in rotational degrees of freedom, which is not surprising considering the rotational constants B_{HF}= 20.939 cm^{-1} and B_{DF}= 11.007cm^{-1}.[21] Only one translational energy distribution is used to fit both the HF and DF data here, though, which is reasonable since the features of the potential energy surface influencing the dynamics should be the same.

If the total available energy for the reaction to make HF or DF were known, then the translational energy distribution would give more detailed information about the internal states of the product molecules. This in turn would reveal some details of the reaction mechanism. However, the energy required to form and remove the HF or DF molecule is not known. If, for the sake of forming a qualitative picture, one assumes the maximum energy in the translational energy distribution is also the total available energy to the product HF or DF, and that the products are all in v= 0, then the rotational states lying under the distribution of Fig. 5 can be as high as J= 14 for HF and J= 20 for DF.[22] Since the vibrational

spacing for HF is 11.83 kcal/mole, it is unlikely that any vibrational excitation occurs. For DF, the vibrational spacing is lower, 8.57 kcal/mole, so it might be energetically possible to have some vibrational excitation. The shape of the translational energy distribution does not support this conclusion, though. Qualitatively, the rotational excitation indicates that in the exit trajectory off the surface, the potential exerts some torque on the molecule. However, there are certainly other factors leading to the broadening of the time-of-flight spectrum, so the J values are not a strict assignment. For example, a variety of surface sites leading to reaction will broaden the product distribution.

The fact that HF and DF have the same maximum energy gives a clue about the microscopic picture of the molecule's departure from the surface. Two extreme cases can be considered. First, if the "kick" off the surface is directed to the light end of the diatomic product, the translational energy distributions for HF and DF, particularly the E_{max}, will be different depending on whether H or D receives the "kick" (Fig. 8). In fact, DF should have about four times the kinetic energy of HF in this scenario (a factor of 2 from v_D^2 and a factor of 2 from M_D). In the second case, however, if the heavy fluorine end gets the "kick" then the translational energy distributions will be about the same for HF and DF, which is what is observed in the experiment. Thus in this picture, if a strong torque is exerted to one end of the product by the potential, it must be applied toward the fluorine rather than the H or D end of the diatomic product. However, in the case of HF and DF the center-of-mass is very close to the fluorine end of the molecule, so if

the repulsion is applied toward the center-of-mass, a similar E_{max} would also be observed. It is safe to say, though, that a strong torque is not applied to the light end of the product HF or DF.

The θ_i distributions for HF and DF in Fig. 6 are peaked with their maxima near the specular angle. Fig. 9 shows the experimental θ_i distribution for HF and a cosine distribution. The cosine distribution would be observed if: 1) the desorbing product had no "memory" of the incident beam and 2) the desorbing product molecule was completely in equilibrium with the surface, at the surface temperature of 690 K. Clearly, the two distributions are different. The experimental distribution is highly peaked towards 45-50° (angle between the detector and the surface normal, which is equal to θ_i). A simple fit to a $\cos^n\theta$ function is not appropriate, however, since $E_\perp$ (the component of the beam energy normal to the surface) changes with θ_i (i.e. as the surface is rotated the incident and final angles are changed simultaneously). It can be concluded, however, that the angular distribution has some dependence on the incident atomic beam angle, and hence $E_\perp$. Thus, the product molecule does have some "memory" of the incident beam. This indicates that the HF and DF are formed through an Eley-Rideal mechanism, which is fairly unusual. Most gas-surface reactions are of the Langmuir-Hinshelwood type.[23-25]

Surface Reaction Mechanism

The possibility of surface roughening as a result of the reactions with H and D atoms was investigated. The H_2 or D_2 time-of-flight patterns from the reflected beam should be sensitive to surface roughness. A less well-ordered surface will give a broader time-of-flight pattern. However, comparison of HF or DF time-of-flight spectra before and after 3 hours of reaction at the same spot on the surface showed no evidence for surface roughening.

The nature of the surface site in this reaction is unknown. The LiF(001) surface has steps and terraces as well as anion vacancies. The vacancies may have an electron trapped in them. The different sites are expected to have different reactivities. Matsumura's calculations[26] clearly show that for anion vacancies, depending on the type (with or without a trapped electron) and location (i.e. corner, edge, or surface), the H-atom will feel a different potential. For example, the energy for adsorption of an H-atom on a surface vacancy with a trapped electron is as high as -6.266 eV, and the H sits in the lattice as H^- where it mimics the missing F^-. On the other hand, an H-atom interacting with the same vacancy without a trapped electron has an adsorption energy of only -0.062 eV, and the potential curve is largely repulsive. Similar differences in the corner and edge sites are reported. Since the HF and DF in this experiment leave the surface with up to 13 kcal/mole of translational energy, it seems unlikely that the trapped electron vacancy is the site of reaction. If the H can sit in the lattice as H^-, then formation of HF that leaves with excess kinetic energy should be unfavorable. Also, the F

that the H reacts with would have to be either an interstitial F or one diffusing along the surface, because in a "perfect" lattice the H would only see Li neighbors. More likely, the HF or DF is formed at sites where the H or D atom cannot easily replace F in the lattice, and then the newly formed molecule feels a repulsive potential as it leaves the surface. The question remains, though, whether H reacts at an anion vacancy site (without a trapped electron) or creates one by pulling F out of the lattice.

Conclusions

A supersonic beam of H or D atoms incident on a LiF(001) surface can be used to study the dynamics of the HF or DF product formed. By directly measuring the time-of-flight of the product species as it evolves from the surface, features of the potential energy surface involved are elucidated. The translational energy distribution describing both products peaks higher in energy than a Maxwell-Boltzmann distribution, indicating that there is a barrier in the exit channel for HF and DF to form and evolve from the surface. There is also evidence of rotational excitation, and a microscopic picture of the molecule-surface interaction is discussed . However, because the energetics of the reaction are unknown in this case, details about the internal states of the products cannot be resolved. A state-specific study of the reaction products could help to further understand the details of the surface reaction mechanism.

With an ultra-high vacuum system, the reaction could be explored over a

wide range of surface temperatures. Here, surface temperatures were limited to 650-700 K to insure cleanliness of the crystal surface. In addition, when the H or D atom hits the surface it has ~7.5 kcal/mole of translational energy from the beam, chiefly determined by the nozzle temperature. A study of the role of energy transfer in the reaction by varying the H or D collision energy would be interesting, but accelerating H or D atoms is not a trivial problem. As new sources of H and D atoms are developed, perhaps such an investigation will be possible.

References and Notes

1. C. Su, Z. G. Dai, W. L. Luo, D. H. Sun, M. F. Vernon, and B. E. Bent, Surf. Sci. **312**, 181 (1994); C. Su, H. Q. Hou, G. H. Lee, Z. G. Dai, W.Luo, M. F. Vernon, and B. E. Bent, J. Vac. Sci. Technol. B **11**, 1222 (1993); C. Su, M. Xi, Z. G Dai, M. F. Vernon, and B. E. Bent, Surf. Sci. **282**, 357 (1993).
2. M. J. Vasile and F. A. Stevie, J. Appl. Phys. **53**, 3799 (1982).
3. M. Balooch and D. R. Olander, J. Chem. Phys. **63**, 4772 (1975).
4. S. T. Ceyer, D. G. Gladstone, M. McGonigal, and M. T. Schulberg, in Investigations of Surfaces and Interfaces-PartA, edited by B. W. Rossiter and R. C. Baetzold (Wiley, New York, 1993), pp. 383-452.
5. C. A. Becker, J. P. Cowin, L. Wharton, and D. J. Auerbach, J. Chem. Phys. **67**, 3394 (1977).
6. S. T. Ceyer, W. L. Guthrie, T. H. Lin, and G. A. Somorjai, J. Chem. Phys. **78**, 6982 (1983).
7. D. A. Mantell, K. Kunimori, S. B. Ryali, G. L. Haller, and J. B. Fenn, Surf. Sci. **172**, 281 (1986).
8. D_0^0(HF)≤ 6.40 eV, D_0^0(LiF)≤ 6.6 eV, from Herzberg; G. Herzberg, Molecular Spectra and Molecular Structure, I. Spectra of Diatomic Molecules (D. Van Nostrand Co., Inc., New York, 1950).
9. K. Matsumura, J. Phys. Soc. Jpn. **52**, 2164 (1983).

10. see ref. 9.

11. Chapter 2.

12. R. David, K. Kern, P. Zeppenfeld, and G. Comsa, Rev. Sci. Instrum. **57**, 2771 (1986).

13. B. Van Zyl and M. W. Gealy, Rev. Sci. Instrum. **57**, 359 (1986); H. Koschmieder and V. Raible, Rev. Sci. Instrum. **46,** 536 (1975); M. A. D. Fluendy, R. M. Martin, E. E. Muschlitz, Jr., and D. R. Herschbach, J. Chem. Phys. **46**, 2172 (1967).

14. The reason the two atomic beams have the same translational energy at the same temperature is that the value of the ratio of the atomic mass to the average mass of the beam is the same. Using E_{beam}= 7/2 kTm/<m>, the maximum energy is calculated, although total rotational cooling (leading to 7/2 instead of 5/2) is not expected. Assuming 3% dissociation versus 1% dissociation only changes E_{beam} by 0.1 kcal/mole. The nozzle temperature is really the determining factor for E_{beam}.

15. A. M. Wodtke, Ph. D. Thesis, University of California, Berkeley, 1986; X. Zhao, Ph. D. Thesis, University of California, Berkeley, 1988; J. D. Myers, Ph. D. Thesis, University of California, Berkeley, 1993.

16. see ref. 9.

17. L. D. Weaver and R. H. Hughes, J. Chem. Phys. **52**, 2299 (1970).

18. V. Cermak, J. Chem. Phys. **44**, 1318 (1966).

19. D. W. Koopman, J. Chem. Phys. **49**, 5203 (1968).

20. H. Hotop, F. W. Lampe, and A. Niehaus, J. Chem. Phys. **51**, 593 (1969).

21. see ref. 8.

22. $E_{HF,J=14}$=12.6 kcal/mole, $E_{DF,J=20}$= 13.2 kcal/mole; values calculated from the rotational constants, B_{HF}= 20.939 cm^{-1} and B_{DF}= 11.007 cm^{-1} in ref. 8.

23. M. L. Yu and L. A. DeLouise, Surf. Sci. Rep. **19**, 285 (1994).

24. E. W. Kuipers, A. Vardi, A. Danon, and A. Amirav, Phys. Rev. Lett. **66**, 116 (1991).

25. C. T. Rettner, Phys. Rev. Lett. **69**, 383 (1992).

26. see ref. 9.

Figure Captions

Fig. 4-1 Nozzle temperature as a function of power. Temperature calculated from neat Ne beam time-of-flight (circles) and measured by optical pyrometry (squares).

Fig. 4-2 Time-of-flight spectra at θ_i= 30° comparing the width of the reflected beam with the width of the fast time-of-flight peak due to collisional effects (see text): (a) H-atom beam (solid line) compared to m/e=20 signal (circles), and (b) D-atom beam (solid line) compared to m/e=21 signal (circles).

Fig. 4-3 m/e=20 time-of-flight spectra (circles) showing the second peak fit at all angles, θ_i, by a simulated time-of-flight spectrum (solid line) generated from one translational energy distribution, shown in Fig. 5. The collisional ionization component shown (.....) is not a fit.

Fig. 4-4 m/e=21 time-of-flight spectra (circles) showing the second peak fit at all angles, θ_i, by a simulated time-of-flight spectrum (solid line) generated from one translational energy distribution, shown in Fig. 5. The collisional ionization component shown (.....) is not a fit.

Fig. 4-5 Translational energy distribution used to fit HF and DF data in Figs. 3 and 4; $\langle E \rangle_T = 4.3$ kcal/mole.

Fig. 4-6 θ_i distributions for HF (filled circles) and DF (open circles) calculated by integrating the simulated time-of-flight spectra for each angle θ_i.

Fig. 4-7 HF translational energy distribution (solid line) compared to a Maxwell-Boltzmann distribution for the surface temperature, $T_{surf} = 690$ K (dashed line). The distributions are normalized.

Fig. 4-8 Microscopic picture of the fluorine end of the diatomic product feeling the "kick" off the surface, justified by HF and DF having the same E_{max}.

Fig. 4-9 Polar plot showing the measured θ_i distribution for HF (triangles) and a cosine distribution expected if HF were in equilibrium with the surface (squares). For the measured distribution, the normal component of the incident enegy ($E_\perp$) changes with θ_i. For Detection Angle 1 $E_\perp = 2.6$ kcal/mole, while for Detection Angle 2 $E_\perp = 6.6$ kcal/mole.

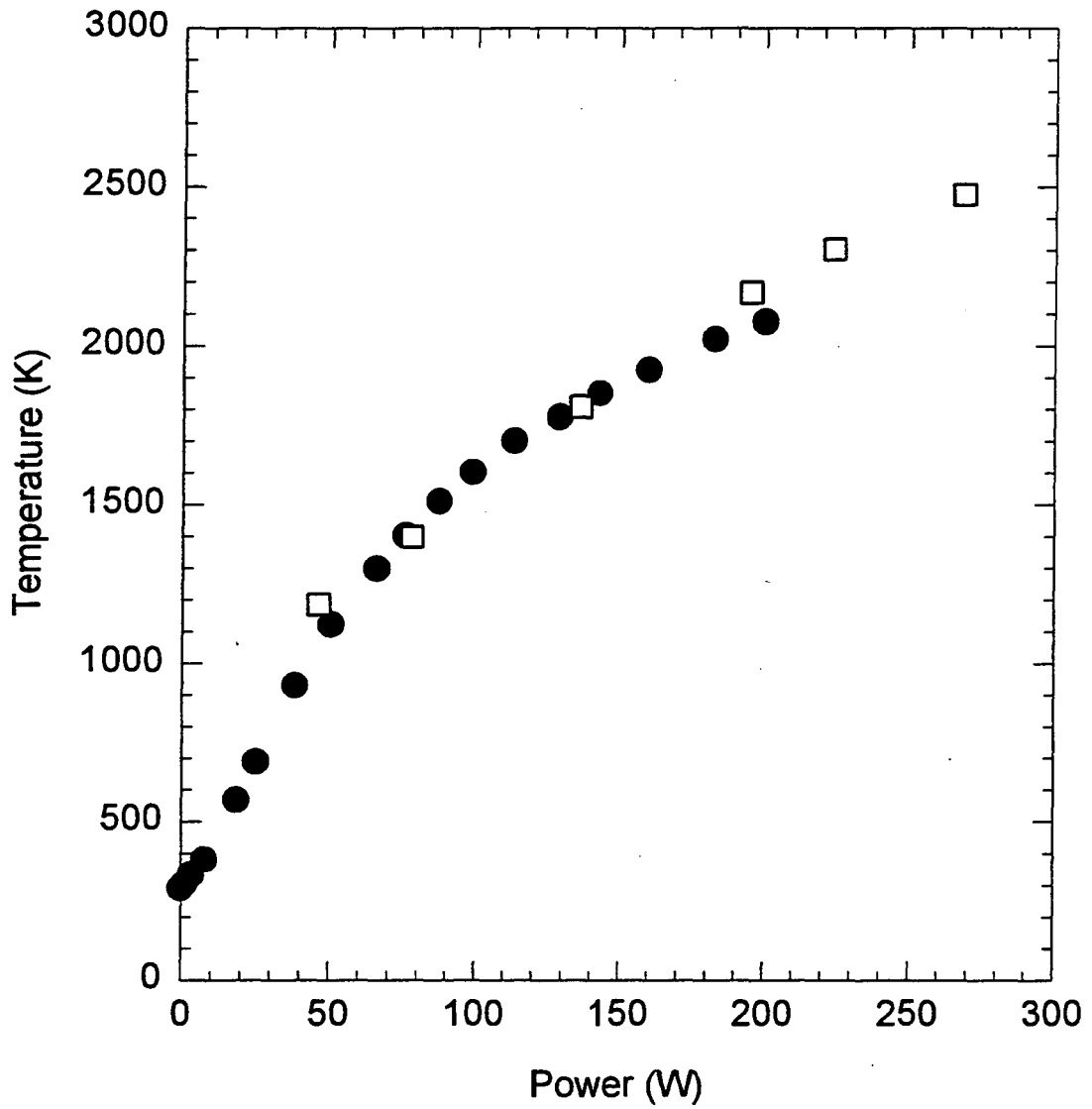
3000
2500
2000
1500
1000
500
0
Temperature (K)
0
50
100
150
200
250
300
Power (W)

Figure 4-1

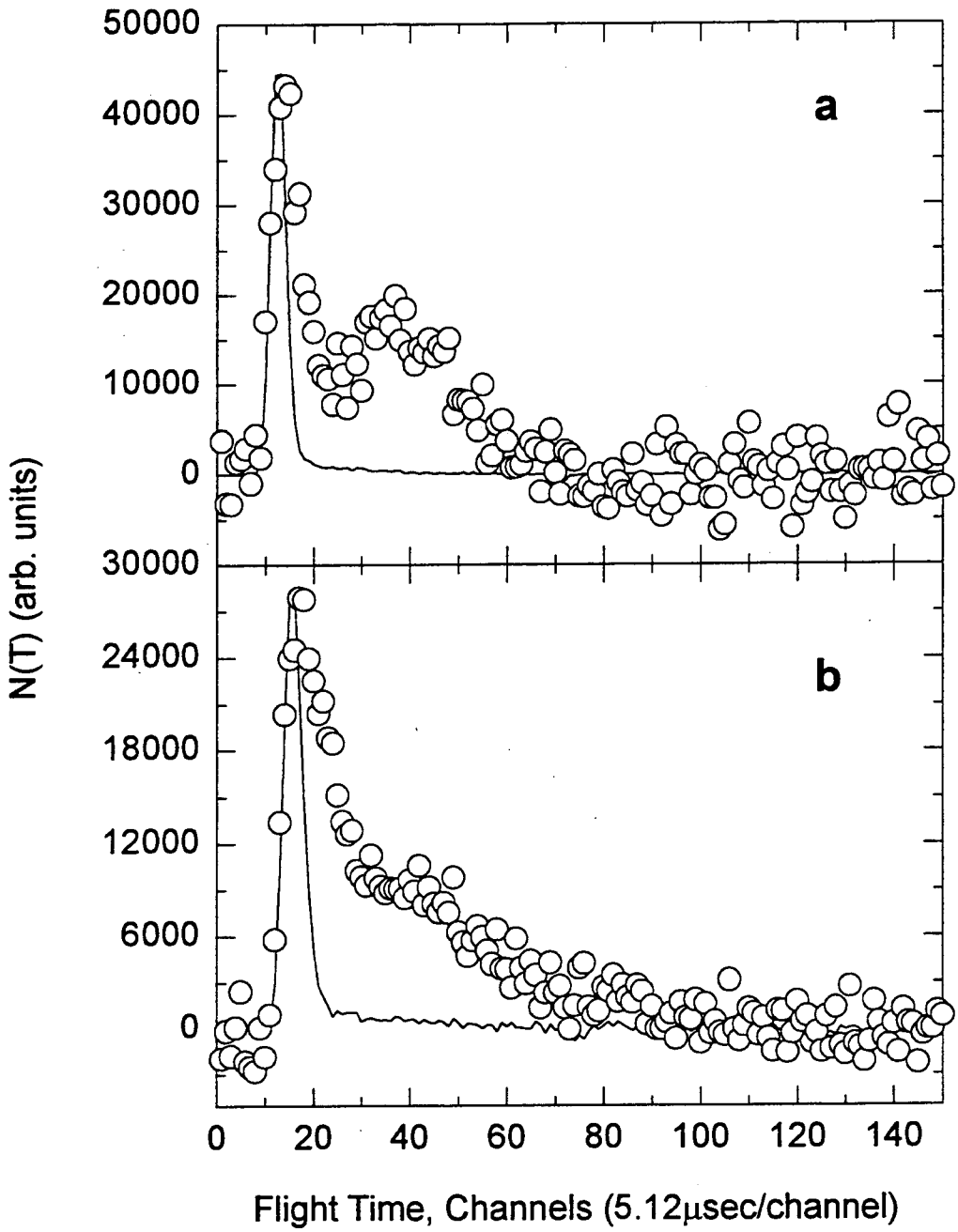
50000
40000
30000
20000
10000
0
a
30000
24000
18000
12000
6000
0
b
N(T) (arb. units)
0
20
40
60
80
100
120
140
Flight Time, Channels (5.12μsec/channel)

Figure 4-2

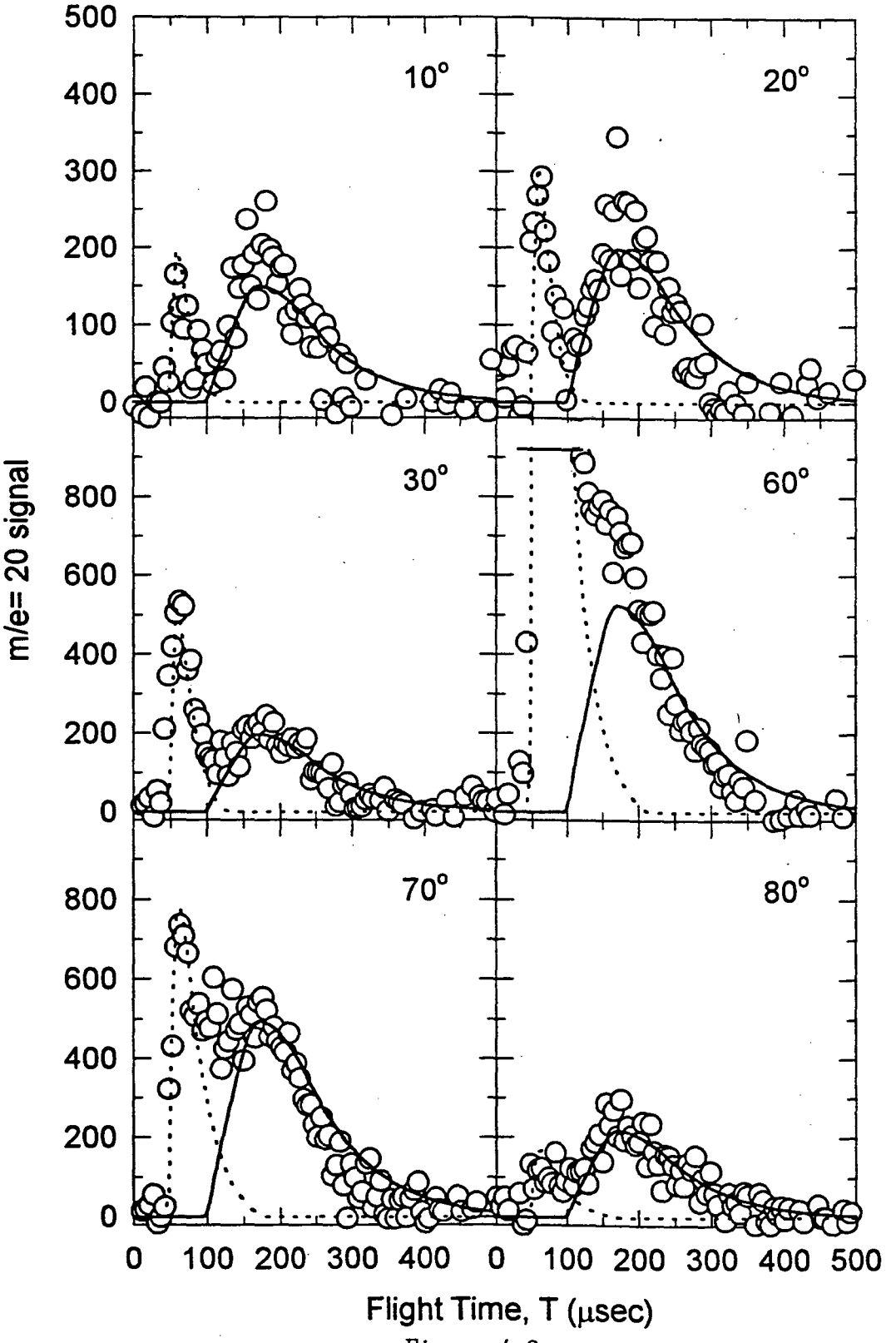
10°
20°
30°
60°
70°
80°
m/e= 20 signal
Flight Time, T (μsec)
0
100
200
300
400
500
600
800

Figure 4-3

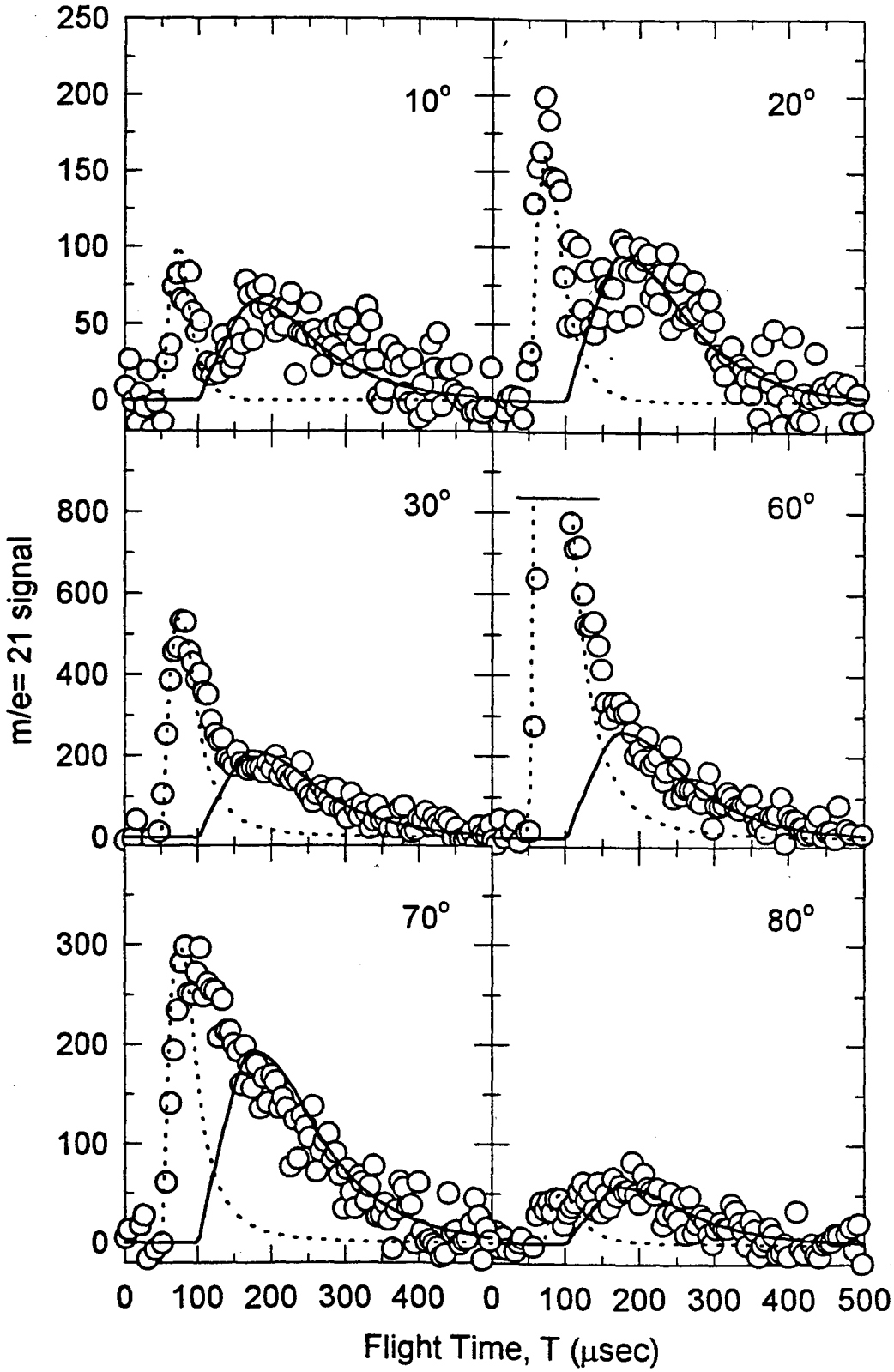
10°
20°
30°
60°
70°
80°
m/e= 21 signal
Flight Time, T (μsec)
0
50
100
150
200
250
200
400
600
800
300
0
100
200
300
400
500

Figure 4-4

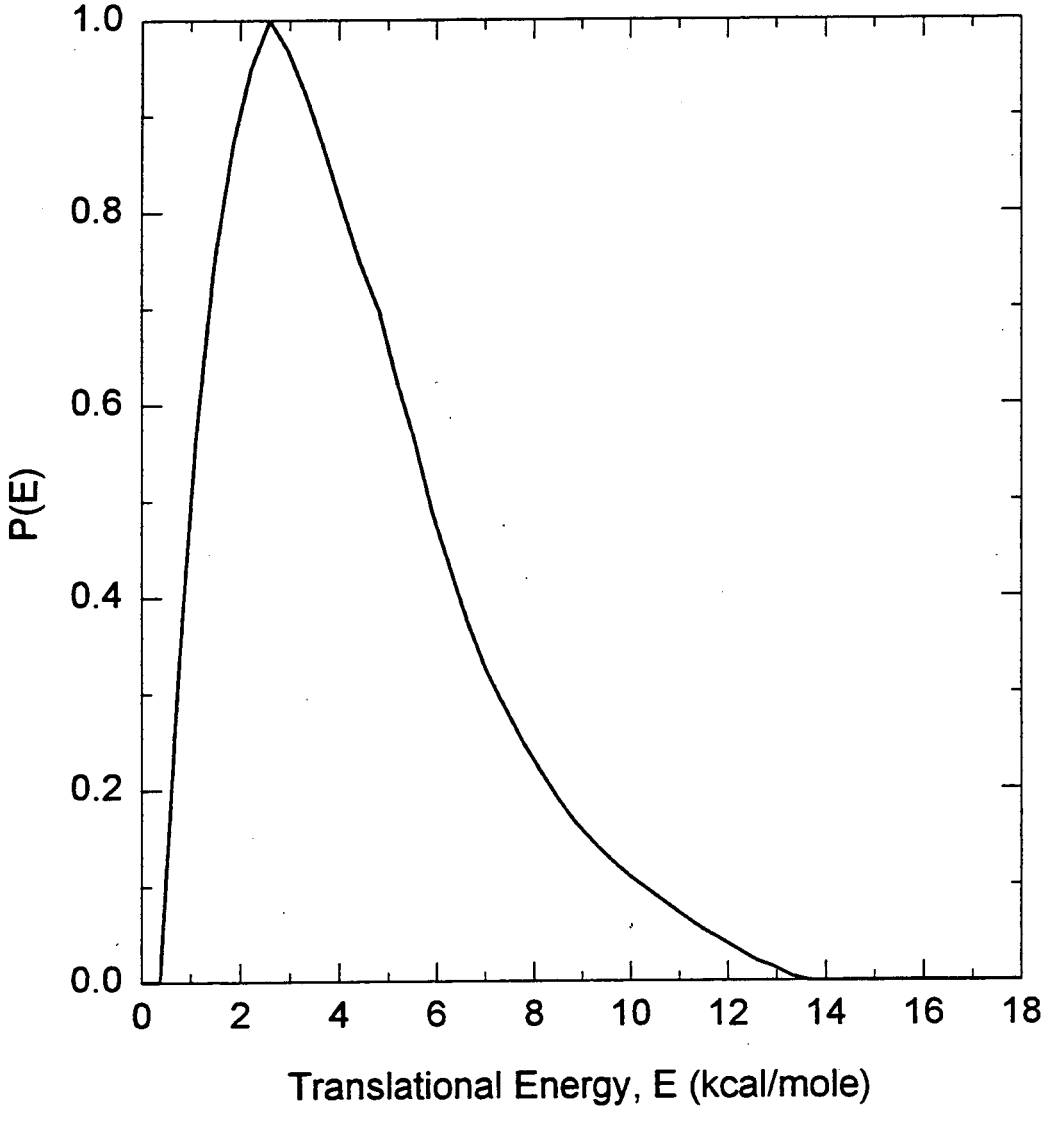
1.0
0.8
0.6
0.4
0.2
0.0
P(E)
0
2
4
6
8
10
12
14
16
18
Translational Energy, E (kcal/mole)

Figure 4-5

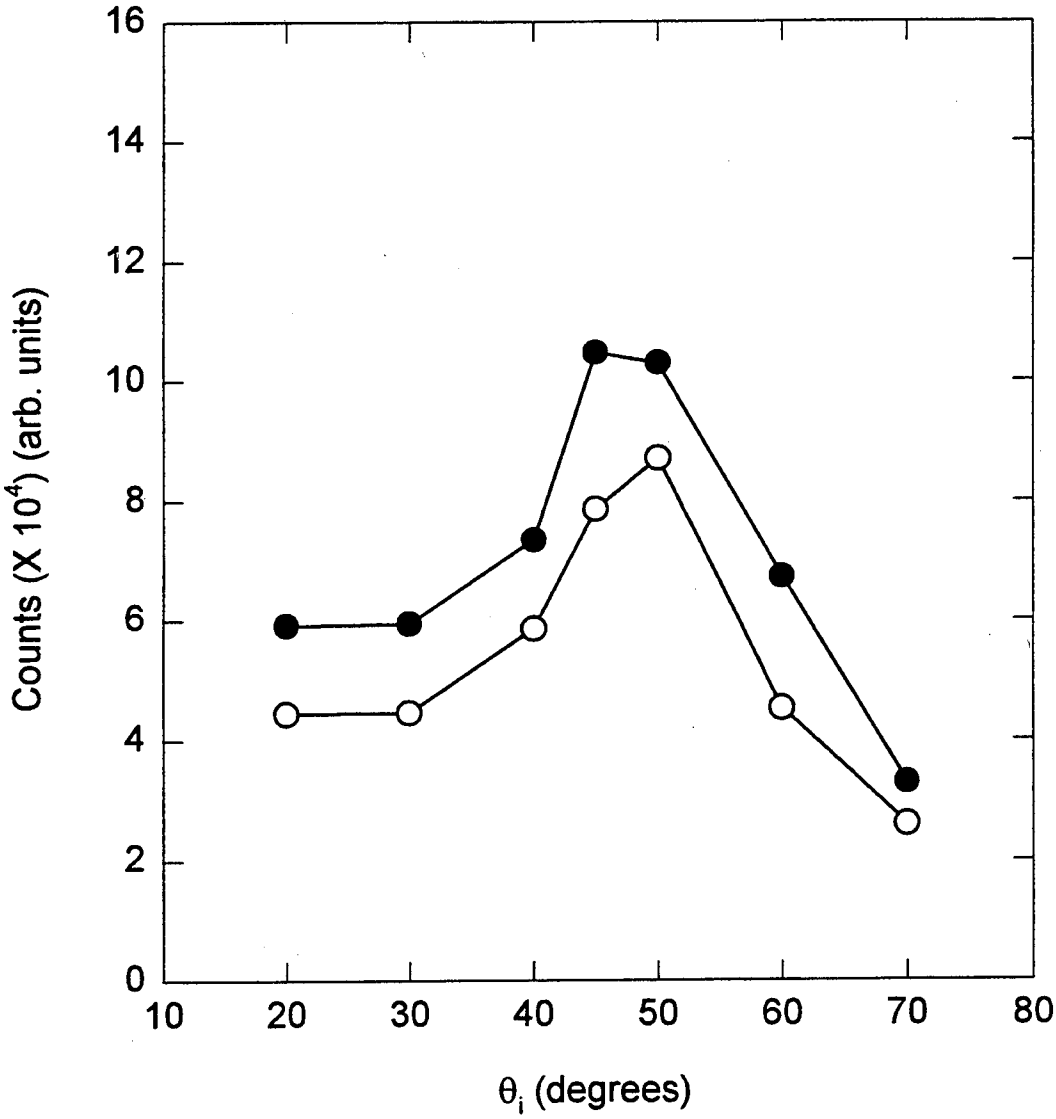
16
14
12
10
8
6
4
2
0
10
20
30
40
50
60
70
80
Counts (X 10^4) (arb. units)
θi (degrees)

Figure 4-6

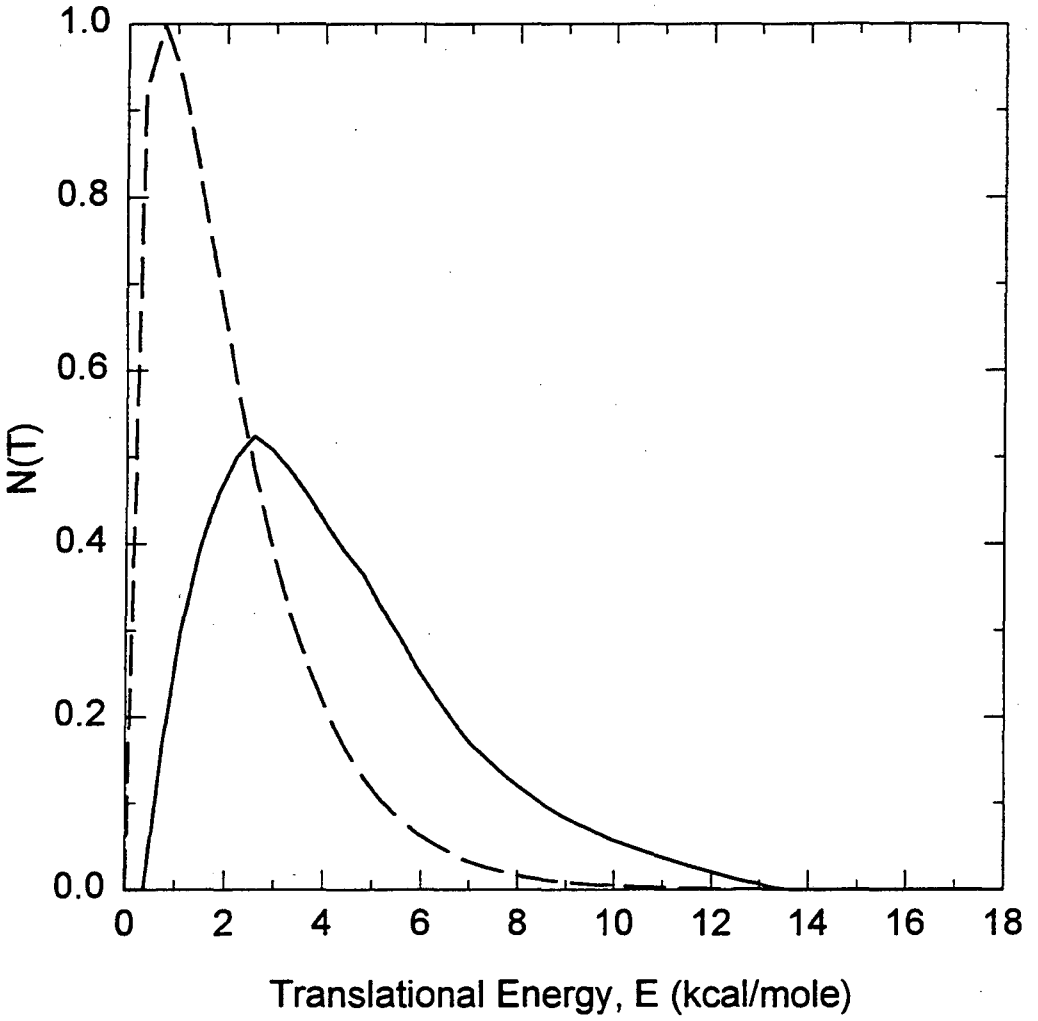
1.0
0.8
0.6
0.4
0.2
0.0
N(T)
0
2
4
6
8
10
12
14
16
18
Translational Energy, E (kcal/mole)

Figure 4-7

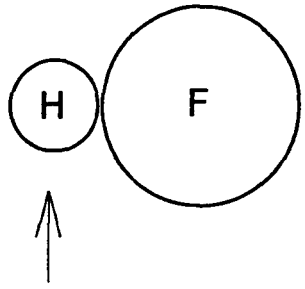

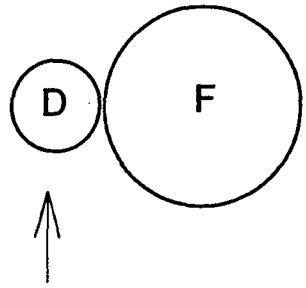

$$1/2\ M_H V_H^2 = 1/2\ M_{HF} V_{HF}^2$$

$$V_{HF}^2 = V_H^2 (M_H/M_{HF})$$

$$V_{DF}^2 = V_D^2 (M_D/M_{DF})$$

Expect 4X the Kinetic Energy

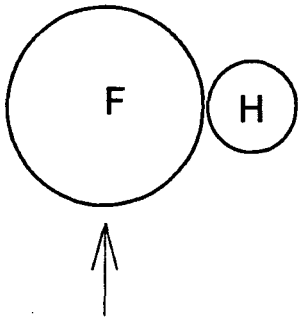

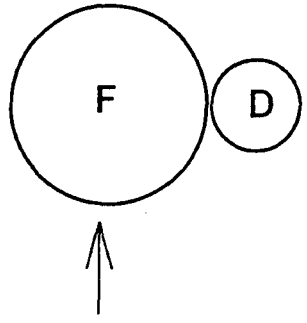

$$1/2\ M_F V_F^2 = 1/2\ M_{HF} V_{HF}^2$$

$$V_{HF}^2 = V_F^2 (M_F/M_{HF})$$

$$V_{DF}^2 = V_F^2 (M_F/M_{DF})$$

Expect the Same Kinetic Energy

Figure 4-8

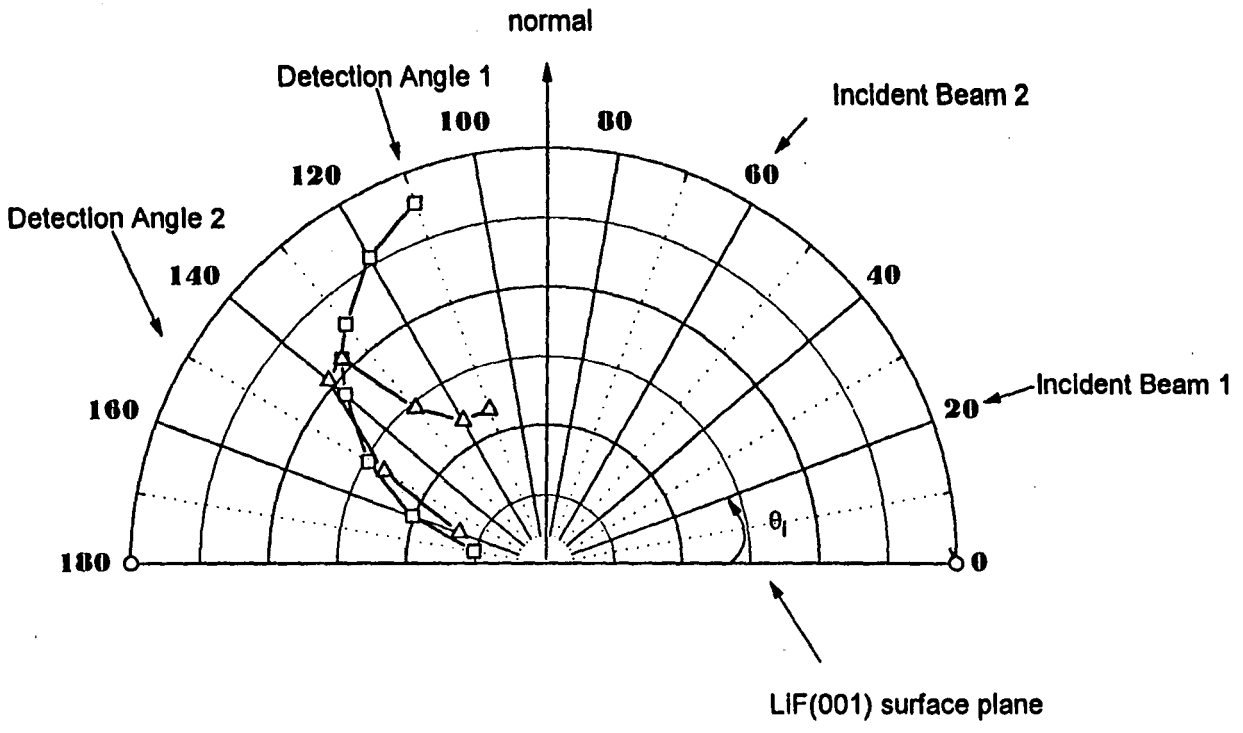
normal
Detection Angle 1
Incident Beam 2
Detection Angle 2
Incident Beam 1
100
80
120
60
140
40
160
20
180
0
θI
LiF(001) surface plane

Figure 4-9

Chapter 5

Dynamics of the Acetylene-d_2, Ethylene-d_4, and Tetradeuteromethane Products from the Reaction of D-Atoms with a Graphite Surface

Introduction

Thermodynamic and kinetic aspects of the reaction of hydrogen atoms with graphite have been studied extensively. Early experiments were performed in a bulb by heating the graphite or by passing molecular hydrogen gas over a hot graphite filament or rod to adsorb atomic hydrogen, and then measuring the desorbing gases. The uptake and desorption of H_2 was studied[1] as well as formation and desorption of hydrocarbon species such as CH_4 and C_2H_2.[2] Later, the kinetics of the reaction of hydrogen atoms with a graphite surface was studied by dissociating molecular hydrogen in a radiofrequency discharge source. In the surface temperature range of 450-1200 K, the products found were molecular hydrogen and methane.[3] Using the technique of modulated molecular beams, Balooch et. al. studied the reaction of H-atoms with graphite where the H-atoms were produced in a pyrolytic effusive source.[4] They found that for surface temperatures up to 800 K, methane was the only product, but acetylene was seen at temperatures above 1000 K. They proposed a model in which the methane was

formed by sequential addition of adsorbed H-atoms and the acetylene was formed by surface recombination of CH groups. They did not see any other hydrocarbon products, in particular ethylene, which differs from this work.

While the kinetics of the reacion of H-atoms with graphite have been well studied, the dynamics have not been directly explored. The dynamics in such hydrogen-carbon systems are now of interest, particularly in the related area of diamond growth. In this work, a supersonic beam of D-atoms incident on the basal plane of a graphite surface is used to generate reaction products whose individual velocities are directly measured upon evolution from the surface. By varying the angle, θ_i, between the beam and the surface plane, while the beam-to-detection angle remains fixed at 90°, a distribution of products giving insight into the reaction mechanism is obtained. The dynamics of the deuterated acetylene, ethylene, and methane products are examined. Two reaction mechanisms occur: methane is formed both through the Eley-Rideal and Langmuir-Hinshelwood mechanisms while the acetylene and ethylene are formed through the Langmuir-Hinshelwood mechanism.

Experimental

A continuous supersonic beam of D-atoms was directed towards the basal plane of highly oriented pyrolitic graphite (HOPG) maintained at T_{surf}= 570 K or T_{surf}= 705 K in a gas-surface scattering apparatus, described previously.[5] The products of the surface reaction are chopped by a cross-correlation wheel, mass

selected, and counted by a channeltron after travelling through a flight distance of 23.9cm.[6] The time-of-flight spectra of individual mass-selected reaction products were measured for m/e= 32, 30, 28, 26, 20, 18, 16, and 14. In addition, the reflected beam was monitored.

The surface was mounted on a 3-axis rotatable manipulator equipped with a resistive heater. The HOPG graphite sample was obtained from Union Carbide (grade ZYH monochromator) and heated for at least 24 hours in vacuum (1×10^{-7} torr) to T_{surf}= 720-770 K before running an experiment. Surface temperature was limited to a narrow range because of concerns about absorption of background gases and limits of the crystal heater. In the range studied, no surface temperature dependence on the dynamics was clearly seen. Time-of-flight spectra were measured as a function of θ_i, the angle between the source and the surface plane, with the source-to-detector angle fixed at 90°. In such a configuration, any memory of the incident beam in the product dynamics is readily ascertained, but it is not possible to measure a full flux angular distribution to determine energy scaling. In addition, by using a D-atom source, differentiation between deuterium from the beam and hydrogen from the bulk crystal[4] is possible.

A D-atom source with a flux of ~5×10^{18} atoms cm^{-2} s^{-1}, previously described,[7] was used to prepare D-atoms by thermal pyrolysis of D_2. D_2 does not react with graphite,[4] so the atomic species is the true reactant species. In a previous experiment on the H and D atom reactions with LiF(001) to make HF and DF, respectively, an artifact in the time-of-flight spectra due to collisional

ionization was identified and discussed extensively.[7] The same effect is observed in some of the time-of-flight spectra for the D-atom reactions with graphite, and similarly discounted. The collisional ionization arises from the fact that D^+, metastable D_2, and Rydberg D-atoms are all produced in the electron bombardment ionizer and can collisionally ionize other molecules in the region between the ionizer and the quadrupole filter of the detector.[8-11] Because the collisional process leads to broadening, which is dependent on θ_i and the particular m/e setting of the quadrupole, there is no systematic way to subtract this artifact from the data. Thus, it is simply excluded from the fitting when analyzing the reaction product data.

Results

Product time-of-fight spectra were taken for m/e= 32, 30, 28, 26, 20, 18, 16, and 14. Table I lists the assignments of the fragments detected. Signal was not observed above m/e= 32, indicating that C_2 is the longest chain hydrocarbon, and no evidence for the evolution of radical species such as CD, CD_2, or CD_3 was found.[4] Radical species would be expected to evolve from the surface more slowly than the stable molecular products observed. Additionally, because no time-of-flight peak was observed at m/e= 36, ethane-d_6 is not a product. The three hydrocarbon products observed were deuterated acetylene, ethylene, and methane. The products will hereafter be referred to by these names with the deuteration understood. The fragmentation patterns for these products and ethane are listed in Table II.[12]

By considering the fragmentation patterns, two schemes for fitting the data were devised and tested, one assuming the C_2 species is ethylene and the other assuming it is ethane. The scheme involving ethane did not fit the data well,[13] and in addition, since m/e= 36 signal was not observed (which is unique to the ethane product), this possibility can be ruled out. Thus, only one scheme, where the C_2 species is ethylene, is discussed here.

The first step of the fitting scheme comes from the fact that C_2D_4 and C_2D_2 do not fragment in the electron bombardment ionizer to m/e= 20. Thus, m/e= 20 data can be fit at all θ_i to derive a single translational energy distribution describing CD_4 evolution. In addition, the fit to the m/e= 18 time-of-flight peak should be generated from the same translational energy distribution since m/e= 18 only appears in the fragmentation pattern of CD_4. Fig. 1 shows the time-of-flight data for m/e= 20 and 18 taken at θ_i= 30°, along with a fit derived from the translational energy distribution in Fig. 2. The fit is a simulated time-of-flight spectrum obtained by the forward convolution method, which includes the various apparatus functions affecting the data.[14-16] Fig. 3 shows how the translational energy distribution of Fig. 2 fits the data at θ_i= 20°, 45°, and 60° for two different surface temperatures, T_{surf}= 570 K and T_{surf}= 705 K. In the θ_i= 45° and 60° data, the fast peak is discounted as an artifact from collisional ionization.[7] There does not seem to be an appreciable difference in the time-of-flight spectra with surface temperature within the narrow range studied here.

Next, the m/e= 32 data, attributed solely to C_2D_4, is fit at all angles θ_i to

generate a single translational energy distribution. This is the distribution describing the dynamics of ethylene evolving from the surface. The fit for m/e= 32 at four angles θ_i is shown in Fig. 4, and the corresponding translational energy distribution is in Fig. 5. The m/e= 26 data has two contributions, one from C_2D_4, and the other from C_2D_2. Once the C_2D_4 distribution has been determined from the m/e= 32 data, the translational energy distribution of C_2D_2 is adjusted to generate the best total fit to the m/e= 26 data at all angles θ_i, while also finding the relative contributions of the two channels. The fit for θ_i= 20°, 45°, and 60° is shown for two surface temperatures in Fig. 6. Once again, the time-of-flight data do not show a dependence on T_{surf} in the range studied. The acetylene translational energy distribution used to fit the m/e= 26 data is shown in Fig. 7.

The time-of-flight spectra at m/e= 16 and 14 should be fit with a combination of the translational energy distributions already derived for methane, ethylene, and acetylene. In the case of m/e= 16, the data can be fit using a combination of the distributions for ethylene and methane; acetylene only gives a small amount of m/e= 16 upon fragmentation in the ionizer. The m/e= 16 data is shown in Fig. 8 with a fit generated from a combination of the translational energy distributions for methane, Fig. 3, and ethylene, Fig. 5. Data for m/e= 14 is fit using a combination of all three translational energy distributions found above, Fig. 9. The contribution from methane is negligible, which is at first surprising when only considering the fragmentation pattern of the different products. It turns out that methane is the minor product of the gas-surface reaction under the conditions

used, though, as will be discussed later. Therefore, it is reasonable that the methane contribution is negligible compared to acetylene and ethylene in the m/e= 14 time-of-flight spectrum. Finally, data at m/e= 30 must be a result of ethylene fragmenting in the electron bombardment ionizer. In Fig. 10, time-of-flight data taken for m/e= 30 is shown θ_i= 20° with a fit generated from the ethylene translational energy distribution in Fig. 5.

In Fig. 11, the three translational energy distributions used to fit the data are plotted with a Maxwell-Boltzmann distribution for T_{surf}= 705 K. The distributions for the products clearly peak at higher energies than the Maxwell-Boltzmann distribution, indicating that there is a barrier to desorption of the product molecules. For the product translational energy distributions, $\langle E \rangle_T$= 3.1 kcal/mole for ethylene, $\langle E \rangle_T$= 4.1 kcal/mole for acetylene, and $\langle E \rangle_T$= 3.9 kcal/mole for methane. The $\langle E \rangle_T$ for acetylene and methane is nearly the same, and the shapes of the distributions are similar, but the low-energy side of the acetylene distribution is shifted to higher energy as is the peak, by about 0.5 kcal/mole. It turns out that the methane distribution is reflecting the translational energy release from two different surface reaction mechanisms, which will be addressed in a discussion of the θ_i product distributions. Since the mechanism of acetylene and methane formation is different, as evidenced by the θ_i distributions (see below), the similarity of the two translational energy distributions is thought to be just coincidental. Ethylene has E_{max}~9 kcal/mole, which is lower than the common E_{max}~11 kcal/mole for acetylene and methane.[17]

Qualitatively, the yield of the products under the conditions used indicates that the major product is ethylene and the minor product is methane. However, the relative yield of products is expected to be dependent on the D-atom flux and so no attempt to quantify a branching ratio is made here. The flux of D-atoms used in this experiment is about 100 times higher than in the modulated molecular beam work of Balooch et. al. (where ethylene product was not observed),[4] suggesting that ethylene formation is dependent on the availability of D-atoms.

The θ_i distributions for each product were measured, and the results are plotted in Figs. 12-14 in polar form along with a cos(θ) distribution, which is scaled to the product intensity for θ_i= 45°. For the θ_i distribution, it is important to remember that the beam-to-detector angle remains fixed at 90°, and thus the normal component of the D-atom incident energy changes with θ_i. The cos(θ) distribution shown here would be observed if the product: 1) was in thermal equilibrium with the surface at the surface temperature and 2) had no "memory" of the incident beam. In Figs. 12-14 the beam is incident on the surface between θ_i= 0-90°, and the products are detected from θ= 90-180° as shown. The angle θ_i is thus equal to the angle between the detector and the surface normal for each measurement. The acetylene θ_i distribution (Fig. 12) is most similar to a cos(θ) distribution. The ethylene θ_i distribution is somewhat similar to a cos(θ) distribution, except the product intensity is more strongly peaked toward the surface normal (Fig. 13). Methane, however, differs from the acetylene and ethylene; part of its distribution is strongly peaked toward 45° and part looks like a $\cos^n(\theta)$ distribution (Fig. 14).

The θ_i distributions show that some of the methane product has a "memory" of the incident beam, while all of the acetylene and ethylene products do not. The important dynamical implications of this result will be discussed in the following section.

Discussion

Product Translational Energy

The translational energy and θ_i distributions of the deuterated methane, acetylene, and ethylene products reveal some dynamical and mechanistic aspects of the gas-surface reaction. The importance of considering both the energy released into translation and the angular distribution of products has been demonstrated.[18] Measuring an angular distribution gives insight into the reaction mechanism and desorption dynamics, but can be misleading without an accompanying translational energy distribution. This is particularly true when a cos(θ) angular distribution is observed, which is normally associated with thermal desorption but can also arise simply from the way a molecule's energy is accommodated at the surface before desorption (i.e. partitioned between the directions parallel and perpendicular to the surface).

The translational energy distributions in Fig. 11 have been normalized to have the same area. All three peak at higher energies than a Maxwell-Boltzmann distribution for T_{surf}= 705 K (shown) and of course for T_{surf}= 570 K (not shown). This is indicative of a barrier in the exit channel of each potential energy surface

governing the interaction of individual products with the graphite surface.[19] If the exit channels had no barrier, Maxwell-Boltzmann distributions would be expected. Deviations from Maxwell-Boltzmann behavior characteristic of $T_{surface}$ have been observed in many studies of desorption.[20-22] In fact, Comsa has pointed out that there is really no general reason to expect to see Maxwell-Boltzmann distributions for the desorption of molecules from a surface.[23] The distributions can be loosely characterized by a "temperature"($T_{<E>} = <E>_T/2k_B$, where k_B is the Boltzmann constant) to quantify the deviation from $T_{surface}$; $T_{<E>} = T_{surface}$ in the case of a Maxwell-Boltzmann distribution.[24] For ethylene, acetylene, and methane, $T_{<E>}$= 780, 1032, and 982 K, respectively.

The three product distributions are also wider than a Maxwell-Boltzmann distribtution. As the newly formed product surmounts the barrier and leaves the surface, potential energy is not only channelled into translation but also into internal modes of the product, which is reflected in the width of the derived translational energy distribution. Products with less translational energy are more internally excited. The width can also reflect reaction at different types of surface sites, which will effectively change the total available energy to the departing molecule. For the two products that desorb without a memory of the incident beam, the width is larger for ethylene, which has more degrees of freedom than acetylene. The methane is formed through two mechanisms, a direct reaction and a surface recombination, and the combination of the two mechanisms or reaction from different types of surface sites may broaden the distribution.

The ethylene distribution has the lowest $T_{<E>}$ (780 K) and also has a lower E_{max} of ~9 kcal/mole. Such behavior is consistent with a lower barrier height with respect to the final product state in the exit channel for the ethylene product as compared to the acetylene or methane. The fact that ethylene was found to be the major product under the conditions used also suggests a lower barrier in the forward direction, from the reactants to the transition state. The ratio of products ethylene: acetylene: methane is ~9:3:1. The barrier in the exit channel can result from the geometric and configurational requirements of the transition state for a particular product to form and evolve. In the case of ethylene, the carbon has the same sp^2 hybridization of the graphitic carbon on the surface. Perhaps this explains why ethylene evolution would have a lower barrier.

Product θ_i Distributions

The θ_i distributions in Figs. 12-14 illustrate how the product flux changes when the surface is rotated. In the rotating surface, fixed source-detector arrangement, the normal component of the incident D-atom energy varies with θ_i. Thus, the distribution observed cannot be properly fit to a $\cos^n(\theta)$ distribution unless there is no effect from the incident beam. However, in the case of acetylene the distribution clearly shows a loss of "memory" of the incident beam. It is interesting to note, in fact, that the angle with the most product intensity here is from the measurement where the D-atom has the least incident energy in the normal direction. A mechanistic picture whereby two CD groups move around on

the surface, find each other, and join together to evolve as acetylene is consistent with no "memory" of the beam, which is the Langmuir-Hinshelwood type mechanism.[25] The plotted cos(θ) distribution, shown for comparison, is what would be seen if a true thermal desorption were occurring with the product in equilibrium with the surface. However, since the translational energy distribution clearly peaks at higher energy than a Maxwell-Boltzmann distribution, thermal desorption is not an appropriate description of the desorption dynamics. The observed θ_i distribution must arise from the dynamics of the last formation step and exit off the surface, reflecting the shape of the exit barrier in the potential energy surface. While the CD groups are accomodated to the surface, the newly formed acetylene is not, for there is no surface temperature dependence observed. The acetylene product formation and desorption can be a concerted process, resulting in a very short residence time for the acetylene on the surface. Thus the cos(θ) distribution reflects the way the acetylene's energy is divided in the directions parallel and perpendicular to the surface as it moves through the exit channel of the potential energy surface.

The θ_i distribution for ethylene, Fig. 13, also shows a loss of "memory" of the beam. The distribution is more highly peaked toward the normal than a cos(θ) distribution, as shown. In fact, it can be fit to a $\cos^{2.6}(\theta)$ distribution, again based on loss of "memory" of the incident beam. The translational energy distribution already indicates that the ethylene evolution is not a simple thermal desorption. A microscopic picture of two accomodated CD_2 groups diffusing along the surface

until they find each other and form the product is consistent with the angular distribution, which is again the Langmuir-Hinshelwood mechanism. However, the strong peaking indicates that the exit channel barrier has a different shape than that in the acetylene case. This barrier is more significant along the normal direction. The ethylene product, whose dynamics show no surface temperature dependence, is not accomodated to the surface. In addition, its energy must be partitioned more in the direction perpendicular to the surface than parallel to the surface in order to result in the $\cos^{2.6}(\theta)$ distribution. Peaked angular distributions have been previously interpreted as resulting from excess energy in the desorbing molecule in a study of CO_2 formed by reaction of CO and oxygen (O_2^{2-} and O) on a Pt(111) surface.[26] There may be a particular configuration of the transition state that leads to more energy in the coordinate normal to the surface.

Fig. 14 shows the θ_i distribution for the methane product. Methane differs from acetylene and ethylene: it appears that two mechanisms, Eley-Rideal and Langmuir-Hinshelwood, are operating simultaneously. One part of the distribution is highly peaked toward 45°, indicating that there is a "memory" of the incident beam. This part of the angular picture is consistent with D-atom addition from the beam to radical species adsorbed on the surface: first to $CD_{(ads)}$, then to $CD_{2(ads)}$, and finally to $CD_{3(ads)}$, constituting an Eley-Rideal mechanism. Sequential additions from adsorbed D-atoms or D-atoms that have suffered a few collisions with the surface before reaction (and therefor lost information about their incident coordinates) contribute to the other part of the angular distribution, which has a

$\cos^{3.4}(\theta)$ distribution (note that this fit is only based on three points, so it is rough). The $\cos^{3.4}(\theta)$ contribution is from reactions of the Langmuir-Hinshelwood type mechanism. Thus, both the Eley-Rideal and Langmuir-Hinshelwood mechanisms are occuring simultaneously. Unfortunately, it is not possible to deconvolute the translational energy distribution (Fig. 2) to reflect the individual contributions from the two mechanisms. Reports of the Eley-Rideal mechanism are quite rare, and so the observation of such a mechanism in this case is of particular interest.[27-29] From kinetic studies,[4] the addition to CD_2 is expected to be the rate-determining step while the addition to CD_3 is very fast. Thus, if there is a competition between D-atom addition to CD_3 and two CD_3 groups finding each other on the surface to form ethane, the D-atom addition would be favored. Perhaps this is why no evidence for ethane formation has been observed.

Microscopic Picture

In the present study, the observed products were methane, acetylene, and ethylene. While methane and acetylene were reported previously in a modulated molecular beam study,[4] ethylene was not. Possible explanations for this discrepancy are that the flux of D-atoms is two orders of magnitude higher here, and the D-atoms are produced in a supersonic expansion with $E_{incident} \sim 7.5$ kcal/mole. Previously, acetylene formation was only seen at high surface temperatures (above 1000 K), and methane was the only hydrocarbon product at lower temperatures (up to 800 K). This suggests that the surface temperature had

to be high enough to insure mobility of the $CD_{(ads)}$ species on the surface so that they could find each other with a reasonable frequency. The incident beam energy of ~7.5 kcal/mole is well above k_BT_{surf} at 1000 K (k_BT_{surf}= 1.99 kcal/mole), so there may be ample energy available for mobility of newly formed species, depending on how much energy is consumed in the initial reaction. Thus, the incident energy from the D-atom can be partially accommodated by CD and CD_2 mobility at the surface, which is necessary for recombination reactions to form acetylene and ethylene.

In further considering the mobility of the radical species at the surface, it becomes clear why ethane formation is not favored. The graphitic carbon atom starts as an sp^2 carbon, covalently bound to three other carbon atoms. As D-atom addition occurs, one C-C bond is broken and a D-atom is attached. However, a CD species is still anchored to the surface by two other C-C bonds if the sp^2 hybridization is maintained. Likewise, a CD_2 species is anchored by one C-C bond. A CD_3 species loses its anchor, though, if sp^2 hybridization is maintained, and thus may not remain on the surface long enough to recombine with another CD_3 group. The final D-atom addition quickly forms CD_4, and thus CD_3 may be a very short-lived species under conditions of high D-atom flux. This would explain the absence of ethane product. In addition, radical species evolution would probably be unfavorable.

Comparison with other Molecular Beam Etching Studies

The dynamics of only a few etching reactions have been studied using molecular beam-surface scattering. Some are mentioned here for the sake of comparison in order to gain a better understanding of the dynamics observed in the D-atom/graphite system. Of particular interest is why some systems show barrierless thermal desorption behavior and others do not.

The dynamics of Cl_2 etching of GaAs have been studied. In one experiment, the etching of the GaAs(110) surface to form $GaCl_3$ was reported,[30] with $GaCl_3$ evolution well described by a Maxwell-Boltzmann distribution with a temperature below $T_{surface}$ and a cosine angular distribution. These results were attributed to an absence of an activation barrier for desorption. In another experiment,[31] time-of-flight spectra of the GaCl from Cl_2 reacting with GaAs(100) were measured. A cosine distribution for GaCl was observed, and the authors mention that an even better fit was found for $\cos^{1.5}(\theta)$, i.e. more peaked towards the surface normal than $\cos(\theta)$. The time-of-flight spectrum was wider than a Maxwell-Boltzmann distribution (the width was dependent on $T_{surface}$ with slower products appearing at lower surface temperatures) except at a high surface temperature of 550 °C. Attempts to fit the time-of-flight distribution for GaCl by including a factor accounting for a surface residence time were unsuccessful. It was postulated, however, that GaCl comes from different types of defect sites, giving rise to different residence times and thus broadens the time-of-flight distribution.

The velocities of $SiCl_n$ (n= 2, 3 and 4) reaction products from the reaction of Cl_2 with Si(111) were measured.[19] The product time-of-flight distributions were well fit with Maxwell-Boltzmann distributions with temperatures 9.0% higher than $T_{surface}$. In addition, the angular distribution was a bit peaked toward the normal, fit by $\cos^{1.26}(\theta)$. The $SiCl_2$ results were explained in terms of a low potential barrier in the exit channel resulting in translational heating of the newly formed products upon desorption.

The results presented here show broader product distributions than expected for a Maxwell-Boltzmann distribution as in the GaCl work, which could arise for similar reasons, i.e. reaction and desorption from different types of surface sites. In addition, the ethylene θ_i distribution is more highly peaked towards the normal than a $\cos(\theta)$ distribution as observed for the $SiCl_2$ and also the GaCl. The acetylene distribution follows $\cos(\theta)$ well, but the translational energy distribution shows that thermal desorption is not taking place. As in the case of $SiCl_2$ formation and desorption, there is a barrier in the exit channel for each product, indicated by the translational energy distribution peaking at higher energy than a Maxwell-Boltzmann distribution for the surface temperature.

Conclusion

The dynamics of three hydrocarbon reaction products in the reaction of D-atoms with a graphite surface have been explored. Time-of-flight measurements of individual products coupled with variation of the beam-surface angle allow for

determination of the translational energy imparted to each product and the role of the incident beam in each product's formation on the surface. Unlike some other etching reactions reported in the literature, the products do not evolve by a simple thermal desorption process. In fact, there is a barrier in the exit channel for each product, and thus the translational energy distribution is shifted to higher energies than a Maxwell-Boltzmann distribution for the surface temperature. Additionally, the distributions do not have the functional form of a Maxwell-Boltzmann distribution. By examining the influence of the incident D-atom beam, it was determined that the methane was formed both by sequential addition of D-atoms from the beam to radical species on the surface (Eley-Rideal mechanism) and also through a Langmuir-Hinshelwood type mechanism, while acetylene and ethylene were formed by recombination of accommodated CD and CD_2 species on the surface, respectively (Langmuir-Hinshelwood). The accommodation of the incident energy allows for surface mobility and the radical species lose "memory" of the incident D-atom velocity. The major product was ethylene under the conditions of D-atom flux and incident energy used. A study of the branching ratio of products by varying the D-atom flux would be interesting and would allow for a greater understanding of the competition between the pathways leading to the three observed products.

References and Notes

1. J. P. Redmond and P. L. Walker, Jr., J. Phys. Chem. **54**, 1093 (1960).
2. J. T. Clarke and B. R. Fox, J. Chem. Phys. **46**, 827 (1967).
3. B. J. Wood and H. Wise, J. Phys. Chem. **73**, 1348 (1969).
4. M. Balooch and D. R. Olander, J. Chem. Phys. **63**, 4772 (1975).
5. see Chapter 2.
6. R. David, K. Kern, P. Zeppenfeld, and G. Comsa, Rev. Sci. Instrum. **57**, 2771 (1986).
7. see Chapter 4.
8. L. D. Weaver and R. H. Hughes, J. Chem. Phys. **52**, 2299 (1970).
9. V. Cermak, J. Chem. Phys. **44**, 1318 (1966).
10. D. W. Koopman, J. Chem. Phys. **49**, 5203 (1968).
11. H. Hotop, F. W. Lampe, and A. Niehaus, J. Chem. Phys. **51**, 593 (1969).
12. E. Stenhagen, S. Abrahamsson, and F. W. McLafferty, Atlas of Mass Spectral Data (John Wiley and Sons, New York, 1969).
13. A fitting scheme assuming that m/e=32 was due to ethane did not fit the data well. In particular, one consistent translational energy distribution could not be found to fit the m/e=26 data.
14. A. M. Wodtke, Ph. D. Thesis, University of California, Berkeley, 1986.
15. X. Zhao, Ph. D. Thesis, University of California, Berkeley, 1988.

16. CMLAB2 fitting program written by J. D. Myers.

17. The uncertainty at the tail end of the translational energy distribution from the 5μsec resolution of the chopper (double sequence cross-correlation wheel) is ~1 kcal/mole.

18. S. T. Ceyer, W. L. Gutherie, T. H. Lin, and G. A. Somorjai, J. Chem. Phys. **78**, 6982 (1983).

19. H. Yoshikawa and K. Shobatake, Chem. Phys. Lett., **223**, 341 (1994).

20. C. T. Rettner, E. K. Schweizer, and C. B. Mullins, J. Chem. Phys. **90**, 3800 (1989).

21. C. R. Arumainayagam, R. J. Madix, M. C. McMaster, V. M. Suzawa, and J. C. Tully, Surf. Sci. **226**, 180 (1990).

22. L. A. DeLouise, J. Chem. Phys. **94**, 1528 (1991).

23. G. Comsa and R. David, Surf. Sci. Rep. **5**, 145 (1985).

24. While $T_{<E>}=<E>_T/2k_B$ is only strictly valid for a Maxwell-Boltzmann distribution, it is often used loosely to quantify deviations in the data from a Maxwell-Boltzmann distribution. See Ref. 23.

25. J. I. Steinfeld, J. S. Francisco, and W. L. Hase, Chemical Kinetics and Dynamics (Prentice Hall International, Inc., London, 1989) p.196.

26. T. Matsushima, Surf. Sci., **123**, L663 (1982).

27. M. L. Yu and L. A. DeLouise, Surf. Sci. Rep. **19**, 285 (1994).

28. E. W. Kuipers, A. Vardi, A. Danon, and A. Amirav, Phys. Rev. Lett. **66**, 116 (1991).

29. C. T. Rettner, Phys. Rev. Lett. **69**, 383 (1992).

30. L. A. DeLouise, J. Chem. Phys. **94**, 1528 (1991).

31. P. Bond, P. N. Brier, J. Fletcher, P. A. Gorry, and M. E. Pemble, Chem. Phys. Lett., **208**, 269 (1993).

Table I. Assignment of Detected Ions from Reaction

m/e	parent ion assignment
32	$C_2D_4^+$
30	$C_2D_4^+$
28	$C_2D_4^+$ $C_2D_2^+$
26	$C_2D_2^+$ $C_2D_4^+$
20	CD_4^+
18	CD_4^+
16	CD_4^+ $C_2D_4^+$ $C_2D_2^+$
14	$C_2D_2^+$ CD_4^+ $C_2D_4^+$

Table II. Fragmentation Patterns[a]

m/e	Ethane-d_6 C_2D_6	Ethylene-d_4 C_2D_4	Acetylene-d_2 C_2D_2	Tetradeuterro-methane CD_4
36	185			
34	146			
32	**1000**	**1000**		
30	273	618		
28	209	640	406	
27			807	
26		106	**1000**	
24		32	286	
20				**1000**
18				830
16	54	110	13	125
14	24	64	136	72
12			194	
2				30

[a]Data from Ref. 12.

Figure Captions

Fig. 5-1 Time-of-flight data (OOOO) taken at θ_i=30° for (a) m/e=20 and (b) m/e=18. The fit (—) is a simulated time-of-flight generated from the translational energy distribution in Fig. 2 for both (a) and (b).

Fig. 5-2 Translational energy distribution for tetradeuteromethane obtained by fitting m/e=20 data at all angles θ_i (some fits are shown in Fig. 3).

Fig. 5-3 Data (OOOO) taken for m/e=20 at different angles θ_i. The left side (a, c, and e) were measured with T_{surf}=570 K. The right side (b, d, f) were measured with T_{surf}=705 K. The collisional ionization component is shown (.....) in (c)-(f) (not a fit) and is off the scale of the graph. The simulated time-of-flight (—) is generated from the translational energy distribution in Fig. 2. The same translational energy distribution is used to fit all the data (a)-(f), for both surface temperatures.

Fig. 5-4 Data (OOOO) taken at m/e=32 for different angles θ_i and T_{surf}=570 K. The fit (—) is a simulated time-of-flight spectrum generated from the translational energy distribution in Fig. 5.

Fig. 5-5 Translational energy distribution for ethylene-d_4 obtained by fitting

m/e=32 data at all angles θ_i (some fits are shown in Fig. 4).

Fig. 5-6 Data (OOOO) taken at m/e=26 for different angles θ_i and two surface temperatures: T_{surf}=570 K (a, c, and e) and T_{surf}=705 K (b, d, and f). The collisional ionization component (off the scale of the graph) is shown in (c)-(f) (.....) (not a fit). The simulated time-of-flight spectra used to fit the product time-of-flight peaks are generated from the translational energy distributions of Fig. 5 (ethylene-d_4, —) and Fig. 7 (acetylene-d_2, -----). The total fit is also shown(_____).

Fig. 5-7 Translational energy distribution for acetylene-d_2 obtained by fitting m/e=26 data at all angles θ_i (some fits are shown in Fig. 6).

Fig. 5-8 Data (OOOO) taken at m/e=16 for different angles θ_i. The fit is generated from the translational energy distributions for ethylene-d_4 (—) (Fig. 5) and acetylene-d_2 (-----) (Fig. 7). T_{surf}=570 K for (a), (c), and (d) and T_{surf}=705 K for (b). In (d) the collisional ionization component (off the scale of the graph) is shown (.....) (not a fit).

Fig. 5-9 Data (OOOO) taken at m/e=14 and θ_i=25° for T_{surf}=705 K. The ethylene-d_4 component (-----), the acetylene-d_2 component (—), and the

tetradeuteromethane component (— — — —), which is negligible, are shown. The translational energy distributions of Figs. 2, 5, and 7 were used for tetradeuteromethane, ethylene-d_4, and acetylene-d_2, respectively, in fitting.

Fig. 5-10 Data (OOOO) taken for m/e=30, θ_i=20°, and T_{surf}=570 K. The fit (—) is a simulated time-of-flight spectrum generated from the translational energy distribution in Fig. 5.

Fig. 5-11 The translational energy distributions of Figs. 2 (tetradeuteromethane, ...), 5 (ethylene-d_4, — — — —), and 7 (acetylene-d_2 — . — .) are plotted with a Maxwell-Boltzmann distribution for T_{surf}=705 K (———).

Fig. 5-12 The measured θ_i distribution for acetylene-d_2 (■) is plotted in polar form with a cos(θ) distribution (●) for comparison. T_{surf}=705 K.

Fig. 5-13 The measured θ_i distribution for ethylene-d_4 (■) is plotted in polar form with a cos(θ) distribution (●) for comparison. T_{surf}=705 K. The data is best fit with a $\cos^{2.6}(\theta)$ distribution, also shown (———).

Fig. 5-14 The measured θ_i distribution for tetradeuteromethane (■) is plotted in polar form with a cos(θ) distribution (●) for comparison. T_{surf}=705 K. Part of the tetradeuteromethane product shows a "memory" of the beam by peaking near θ_i=45°.

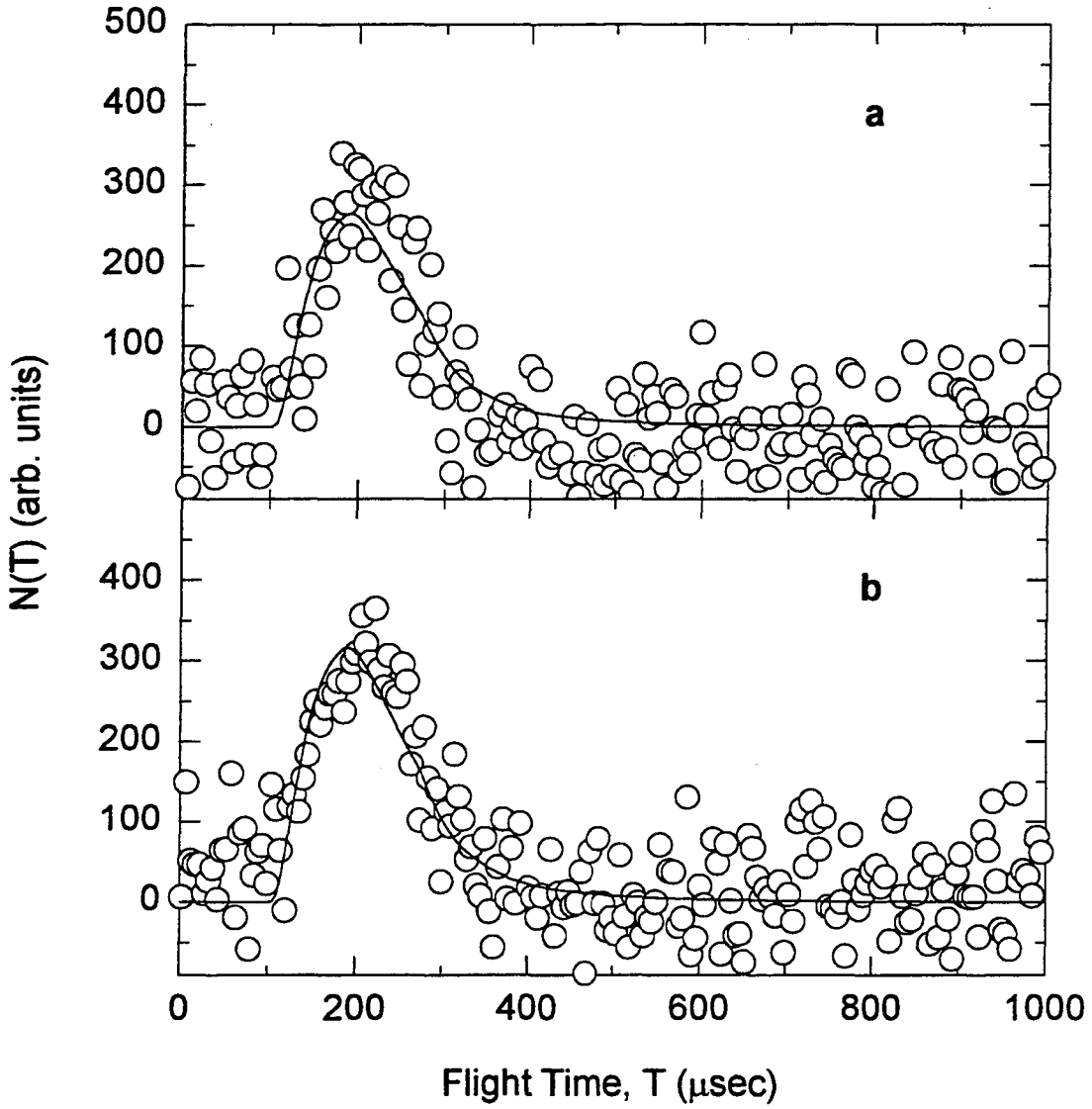
500
400
300
200
100
0
a
400
300
200
100
0
b
N(T) (arb. units)
0
200
400
600
800
1000
Flight Time, T (μsec)

Figure 5-1

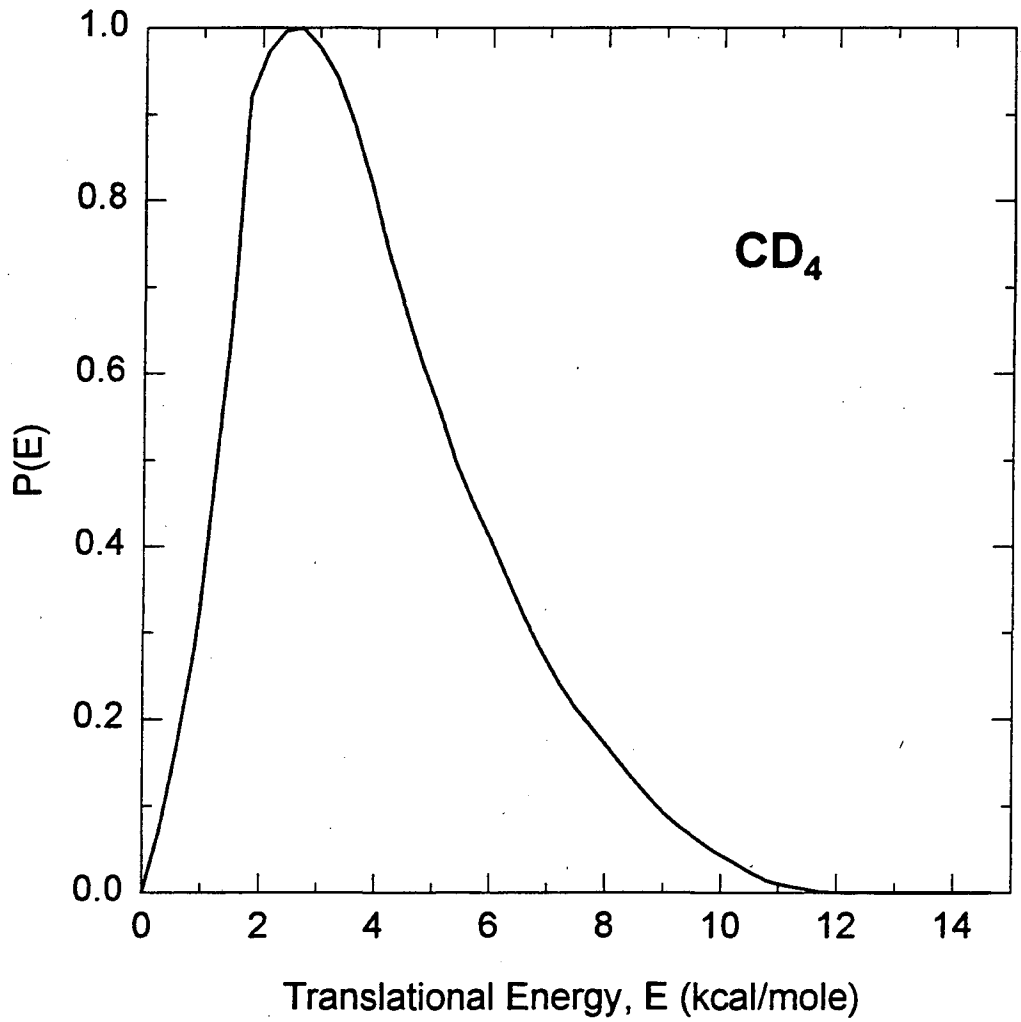
1.0
0.8
0.6
0.4
0.2
0.0
P(E)
CD4
0
2
4
6
8
10
12
14
Translational Energy, E (kcal/mole)

Figure 5-2

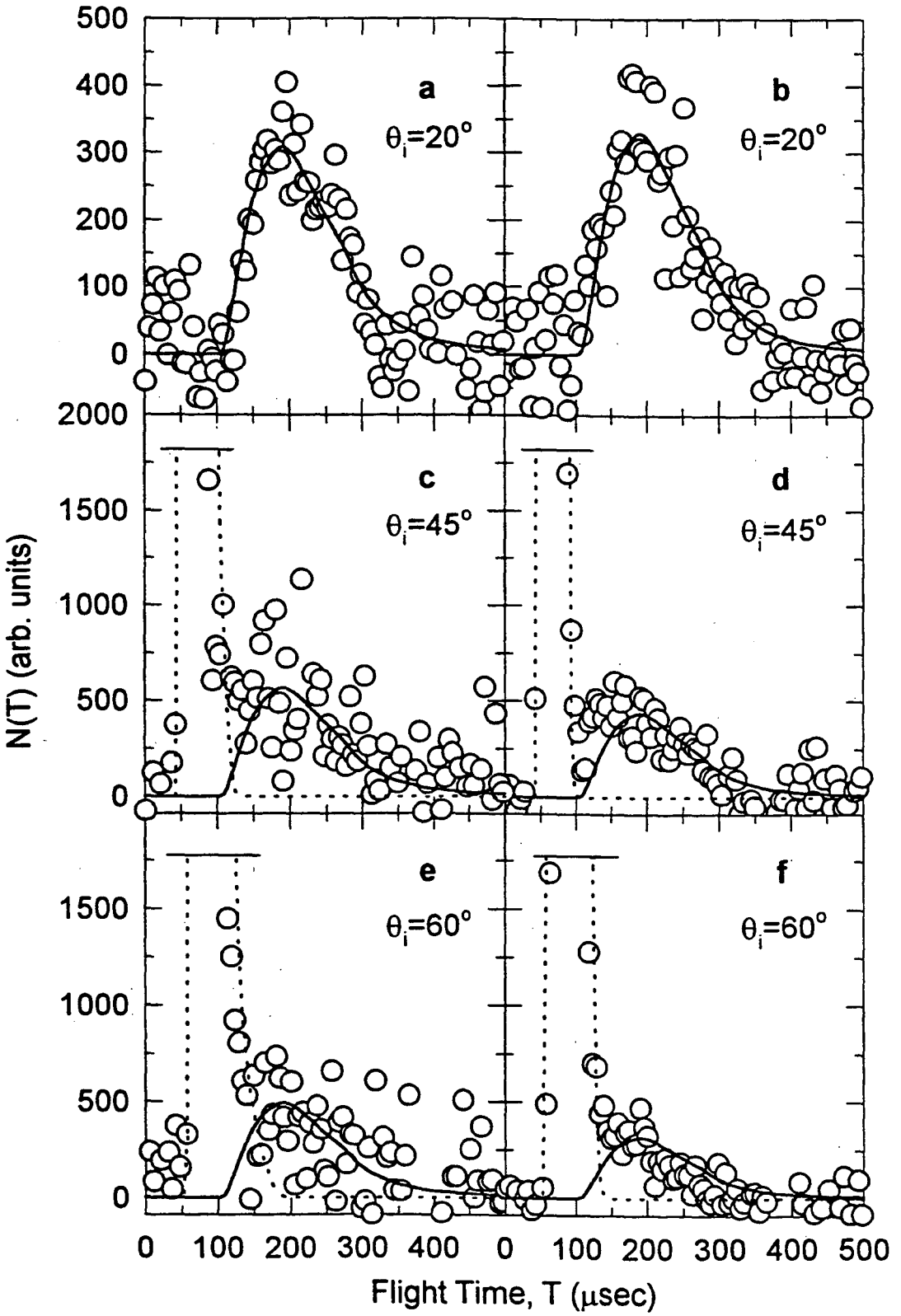
a
θi=20°
b
θi=20°
c
θi=45°
d
θi=45°
e
θi=60°
f
θi=60°
N(T) (arb. units)
Flight Time, T (μsec)
0
100
200
300
400
500
1000
1500
2000

Figure 5-3

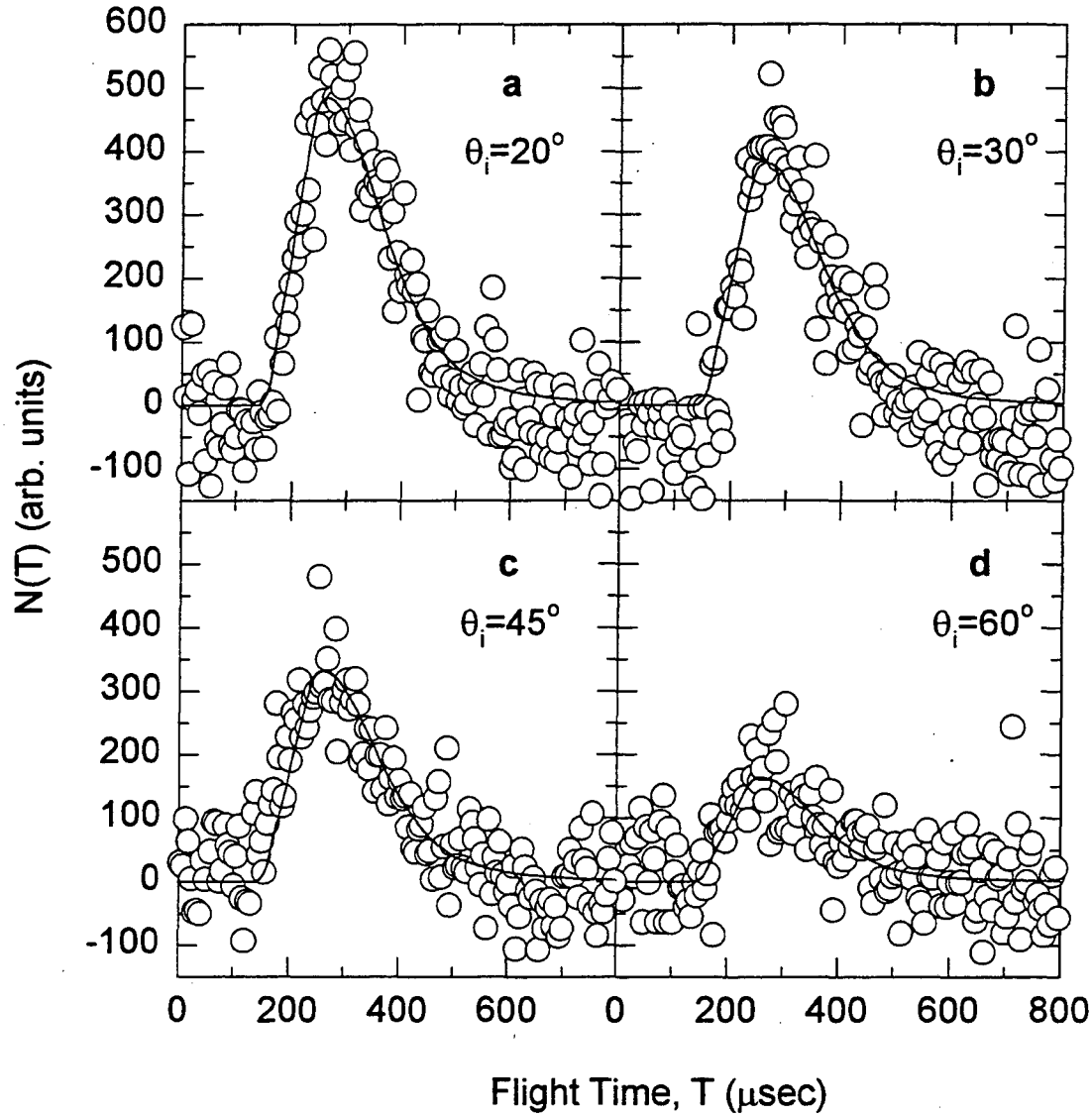
a
θi=20°
b
θi=30°
c
θi=45°
d
θi=60°
N(T) (arb. units)
Flight Time, T (μsec)
600
500
400
300
200
100
0
-100
0
200
400
600
800

Figure 5-4

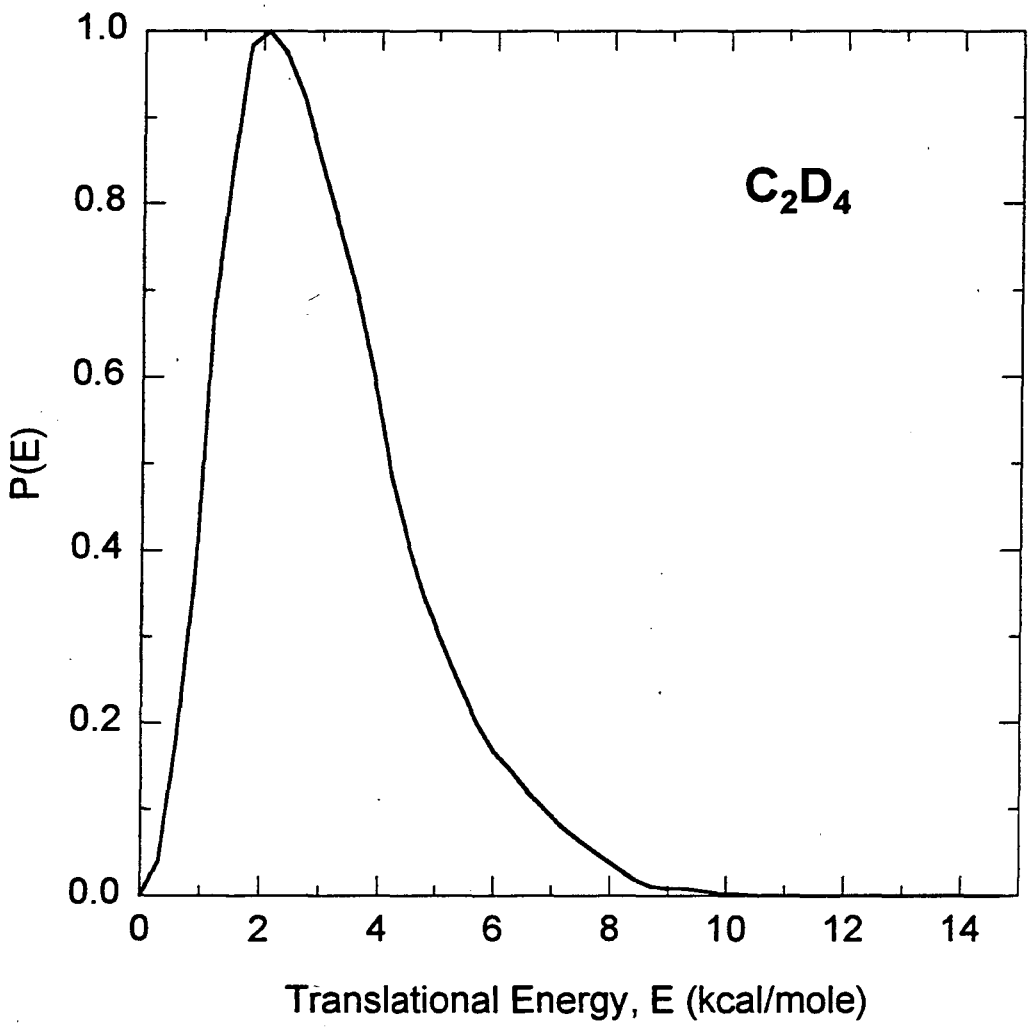
1.0
0.8
0.6
0.4
0.2
0.0
P(E)
C_2D_4
0
2
4
6
8
10
12
14
Translational Energy, E (kcal/mole)

Figure 5-5

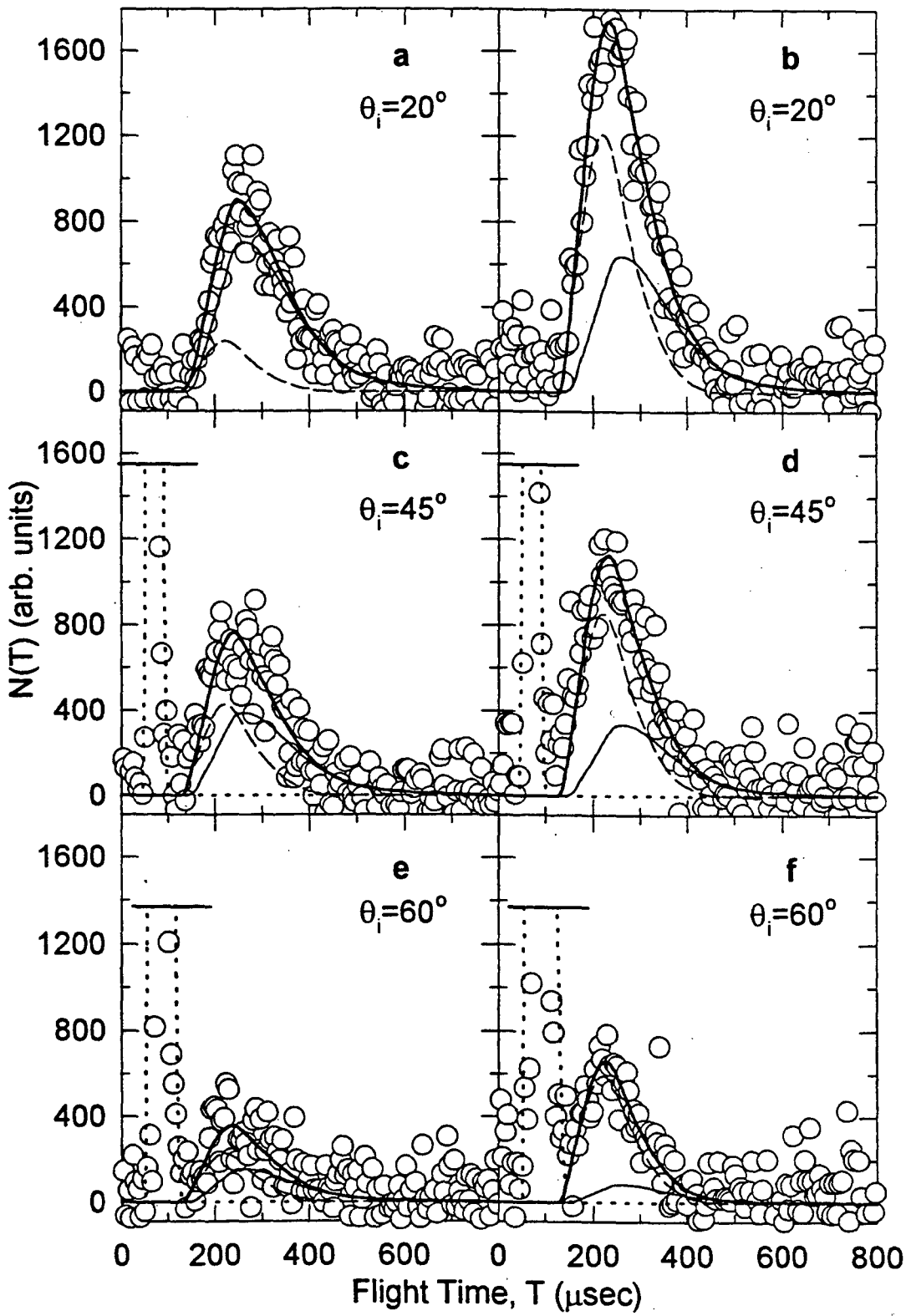
a
θi=20°
b
θi=20°
c
θi=45°
d
θi=45°
e
θi=60°
f
θi=60°
N(T) (arb. units)
Flight Time, T (μsec)
0
200
400
600
800
1200
1600

Figure 5-6

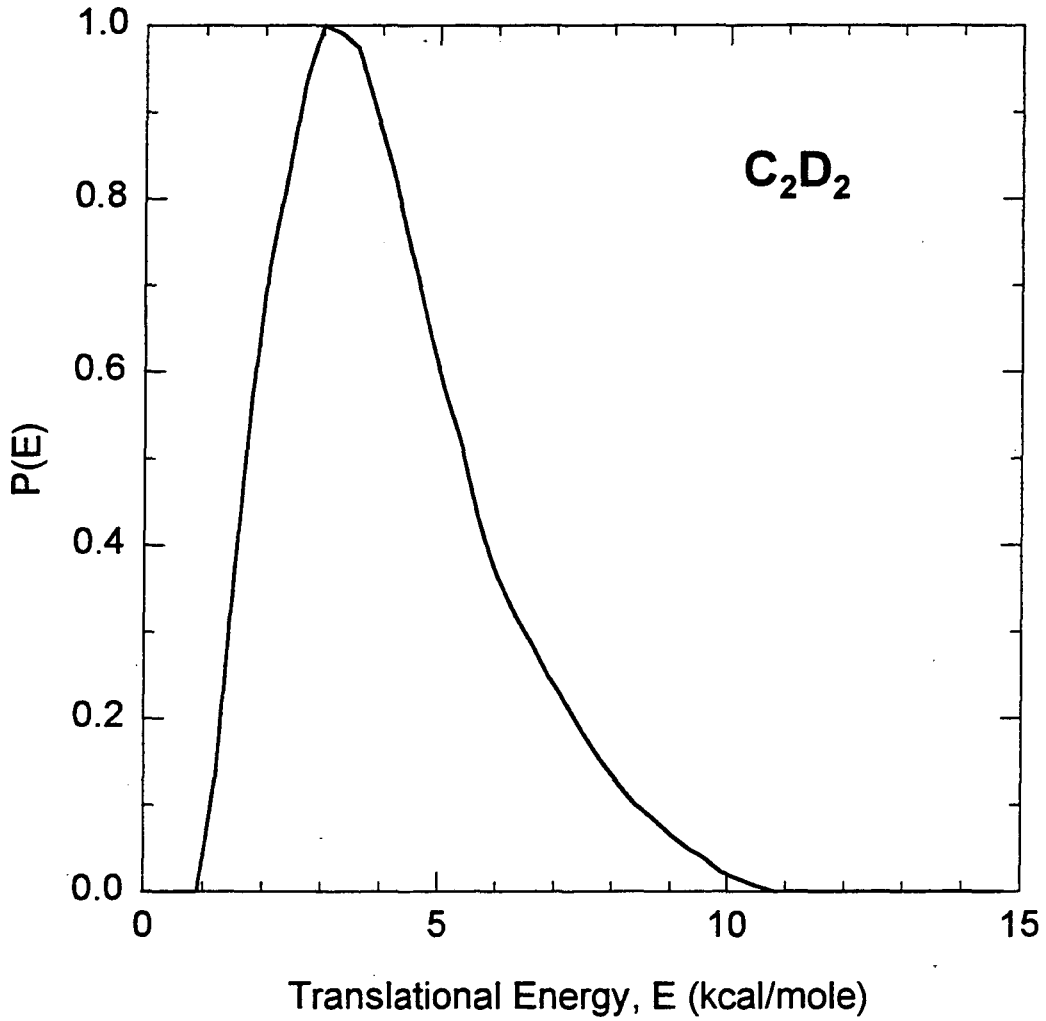
1.0
0.8
0.6
0.4
0.2
0.0
P(E)
C_2D_2
0
5
10
15
Translational Energy, E (kcal/mole)

Figure 5-7

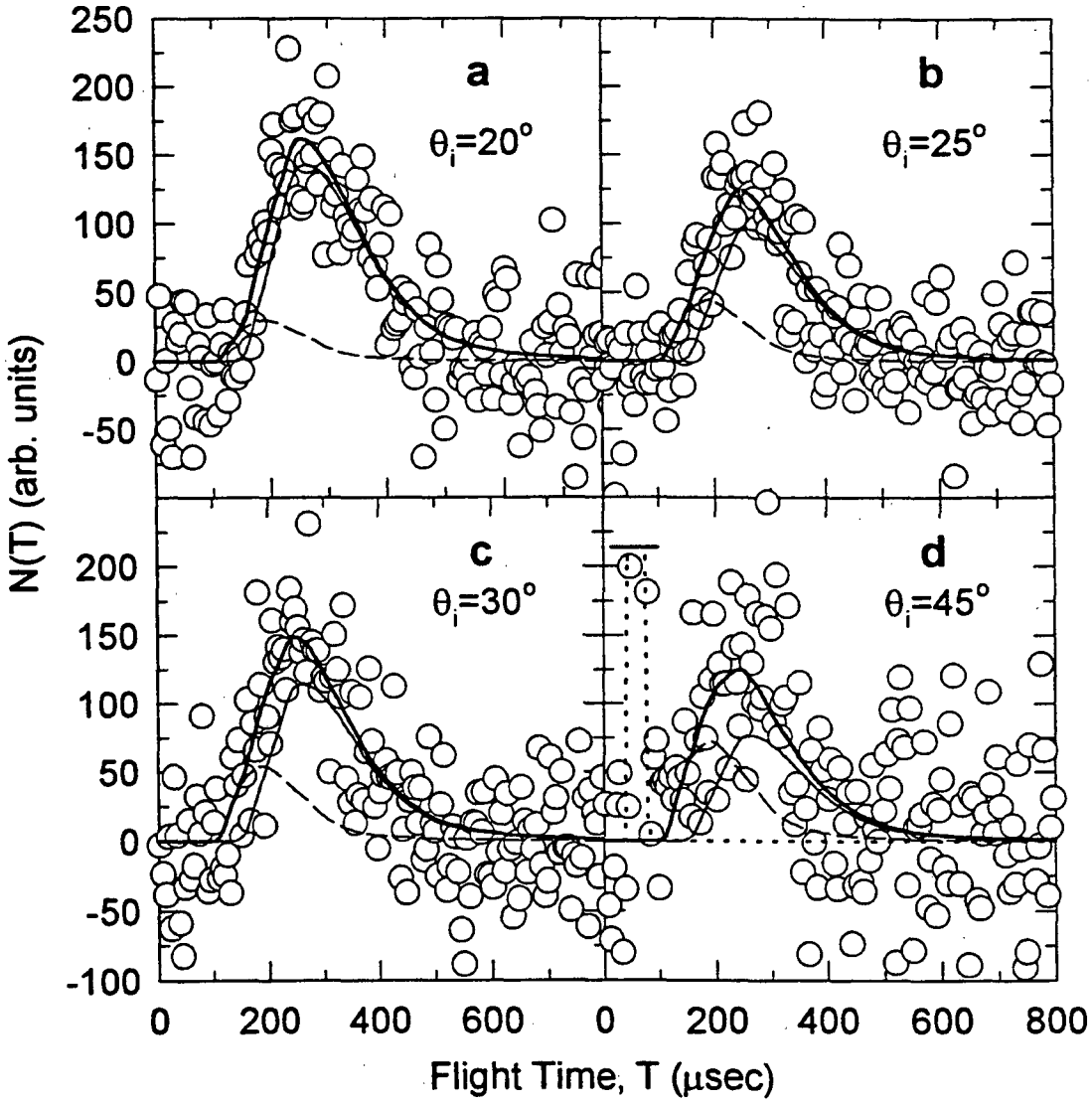
a
θi=20°
b
θi=25°
c
θi=30°
d
θi=45°
N(T) (arb. units)
Flight Time, T (μsec)
250
200
150
100
50
0
-50
-100
0
200
400
600
800

Figure 5-8

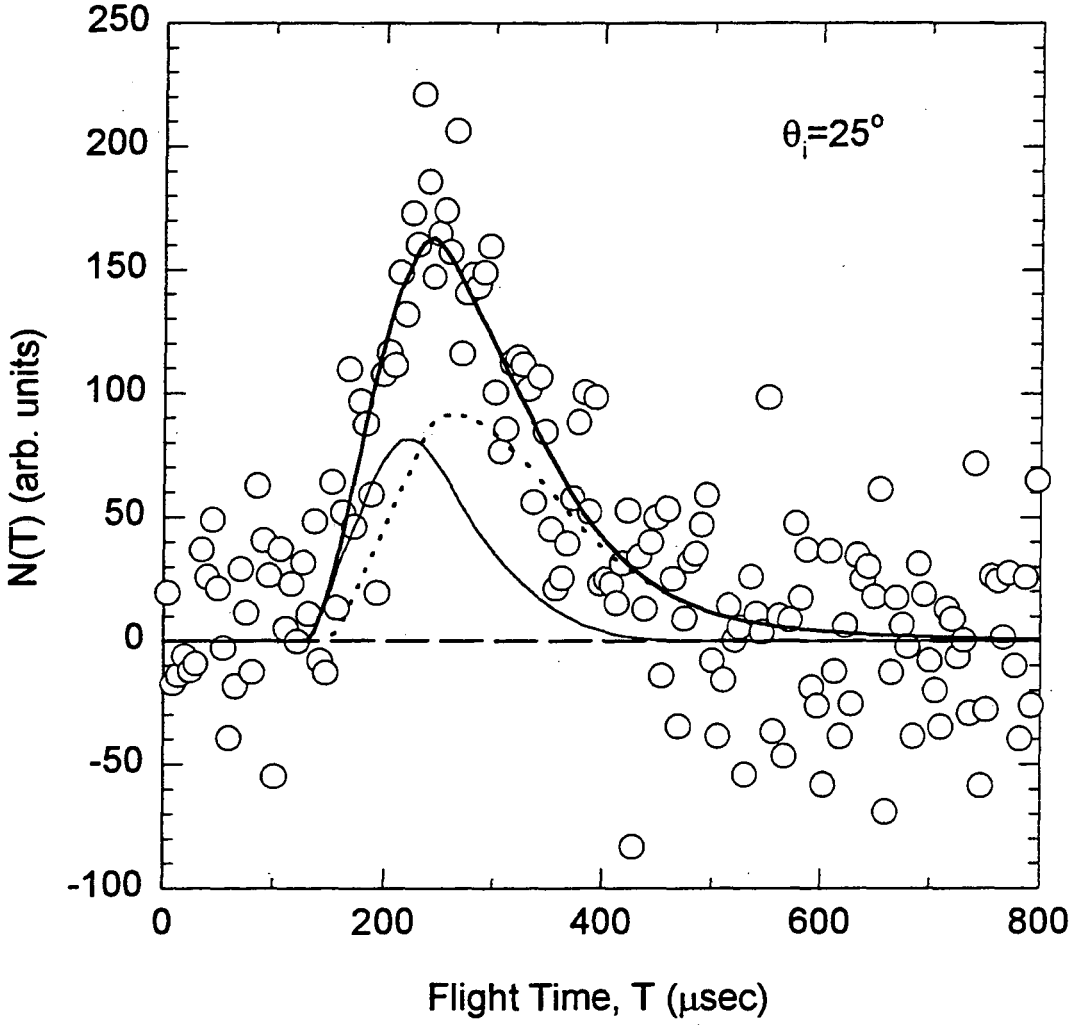
250
200
150
100
50
0
-50
-100
N(T) (arb. units)
0
200
400
600
800
Flight Time, T (μsec)
θi=25°

Figure 5-9

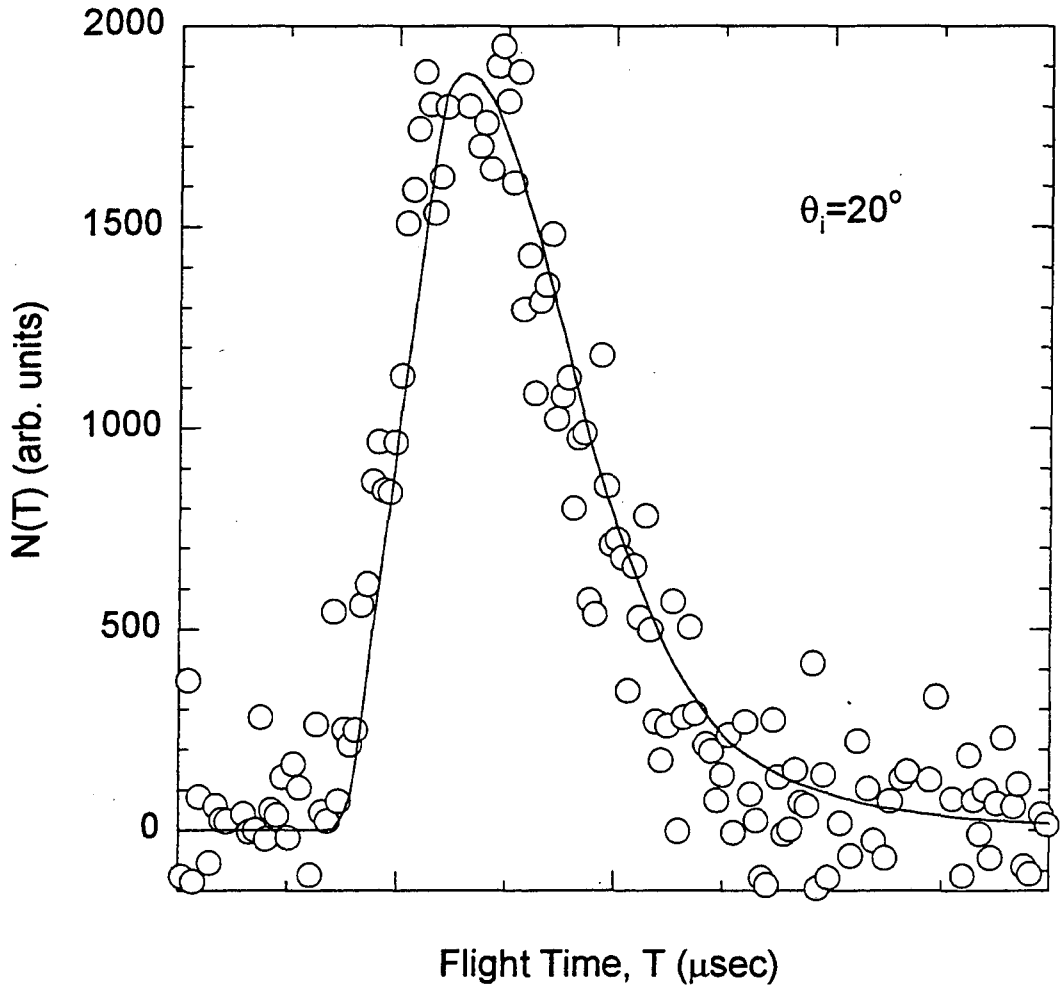

Figure 5-10

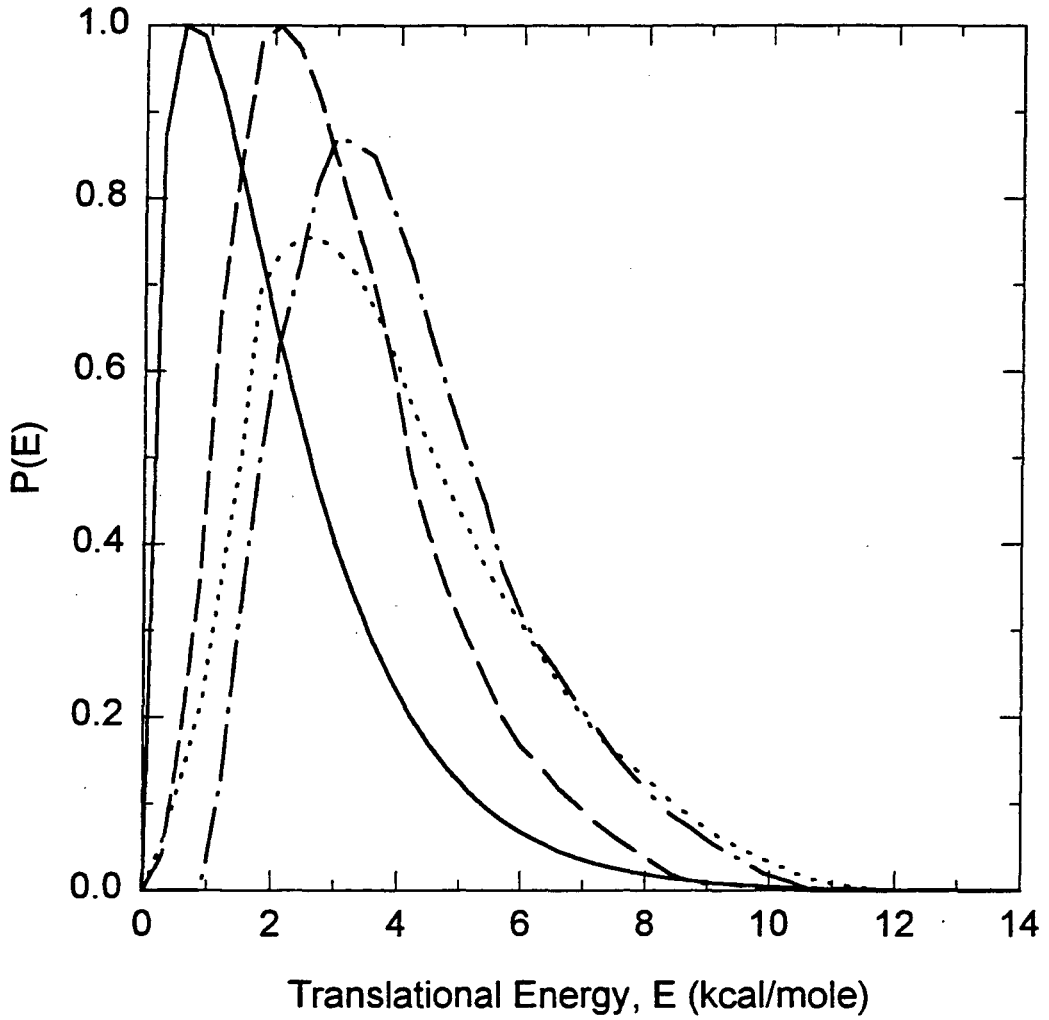
1.0
0.8
0.6
0.4
0.2
0.0
P(E)
0
2
4
6
8
10
12
14
Translational Energy, E (kcal/mole)

Figure 5-11

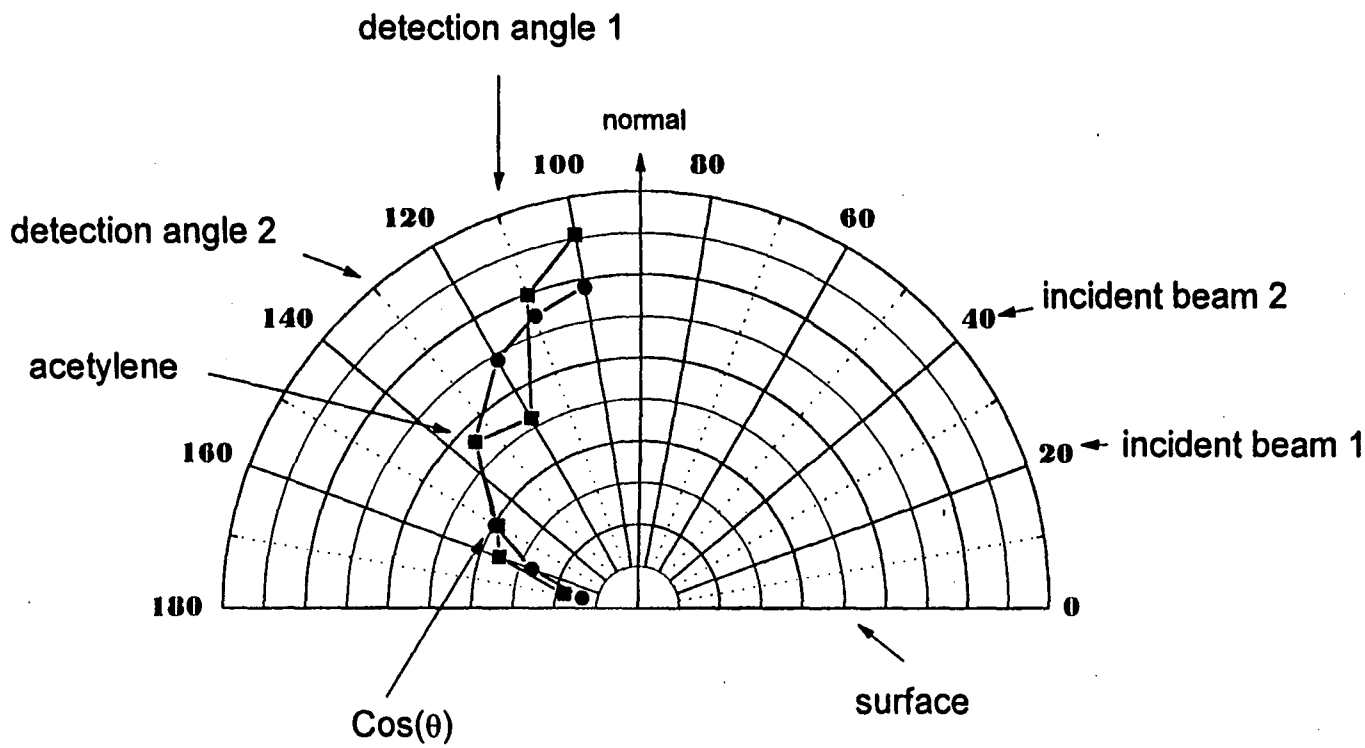
detection angle 1
normal
100
80
120
60
detection angle 2
140
40
incident beam 2
acetylene
160
20
incident beam 1
180
0
Cos(θ)
surface

Figure 5-12

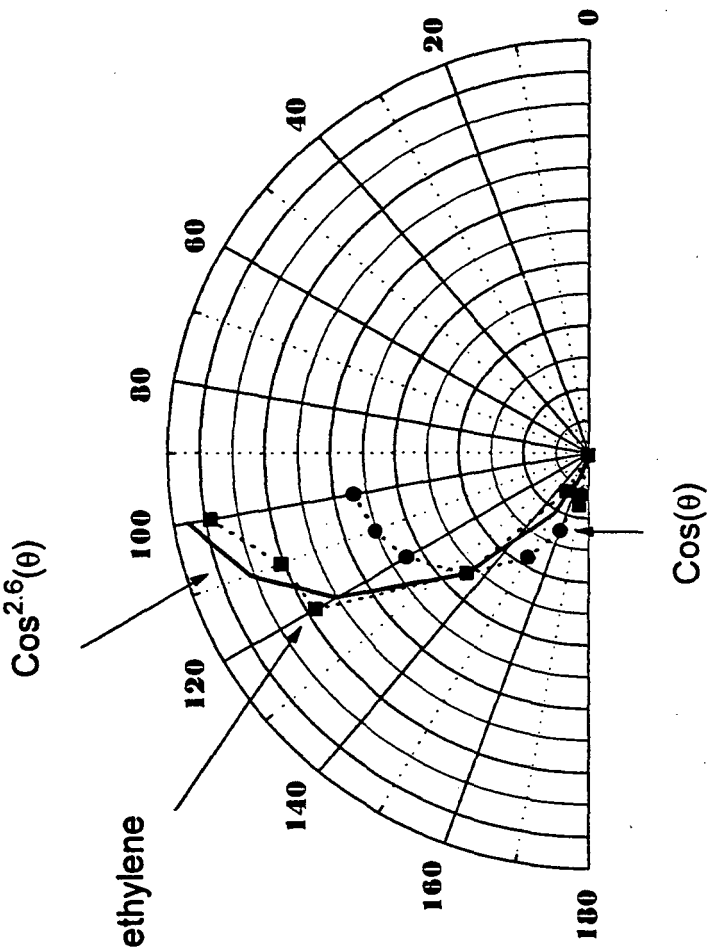

Figure 5-13

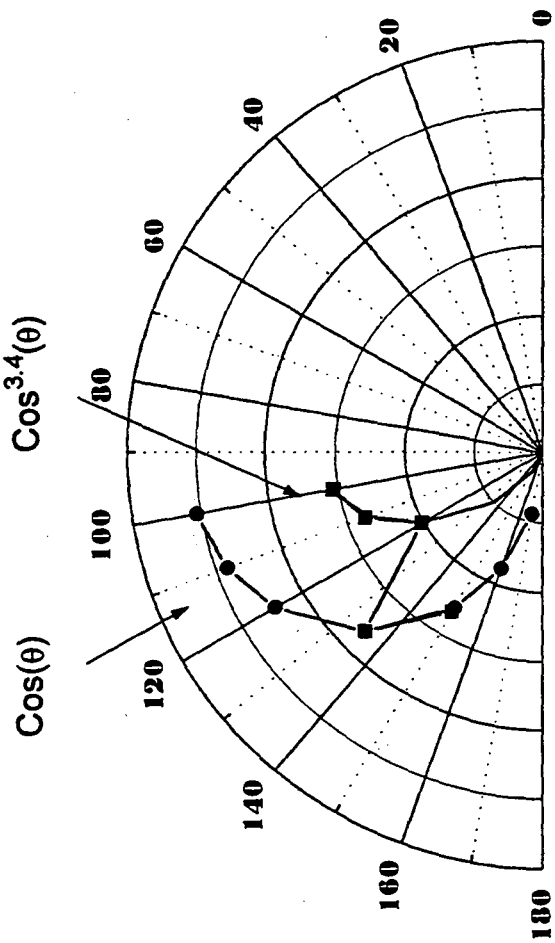

Figure 5–14

LAWRENCE BERKELEY LABORATORY
UNIVERSITY OF CALIFORNIA
TECHNICAL INFORMATION DEPARTMENT
BERKELEY, CALIFORNIA 94720